BONNER METEOROLOGISCHE ABHANDLUNGEN
Heft 74 (2016) (ISSN 0006-7156)
Herausgeber: Andreas Hense

Kaleem Muhammad

A SENSITIVITY STUDY OF DECADAL CLIMATE PREDICTION TO AEROSOL VARIABILITY USING ECHAM6-HAM (GCM)

BONNER METEOROLOGISCHE ABHANDLUNGEN
Heft 74 (2016) (ISSN 0006-7156)
Herausgeber: Andreas Hense

Kaleem Muhammad

A SENSITIVITY STUDY OF DECADAL CLIMATE PREDICTION TO AEROSOL VARIABILITY USING ECHAM6-HAM (GCM)

A sensitivity study of decadal climate prediction to aerosol variability using ECHAM6-HAM (GCM)

DISSERTATION
ZUR
ERLANGUNG DES DOKTORGRADES (DR. RER. NAT.)
DER
MATHEMATISCH-NATURWISSENSCHAFTLICHEN FAKULTÄT
DER
RHEINISCHEN FRIEDRICH-WILHELMS-UNIVERSITÄT BONN

vorgelegt von
MS Atmospheric Sciences, Oceanography and Climate
Muhammad Kaleem
aus
Multan, Pakistan

Bonn, June, 2016

Diese Arbeit ist die ungekürzte Fassung einer der Mathematisch-Naturwissenschaftlichen Fakultät der Rheinischen Friedrich-Wilhelms-Universität Bonn im Jahr 2016 vorgelegten Dissertation von Kaleem Muhammad aus Multan, Pakistan.

This paper is the unabridged version of a dissertation thesis submitted by Kaleem Muhammad born in Multan, Pakistan to the Faculty of Mathematical and Natural Sciences of the Rheinische Friedrich-Wilhelms-Universität Bonn in 2016.

Anschrift des Verfassers: Address of the author:

Kaleem Muhammad
Meteorologisches Institut der
Universität Bonn
Auf dem Hügel 20
D-53121 Bonn

1. Gutachter: Prof. Dr. Andreas Bott, Rheinische Friedrich-Wilhelms-Universität Bonn
2. Gutachter: Prof. Dr. Andreas Hense, Rheinische Friedrich-Wilhelms-Universität Bonn

Tag der Promotion: 24. October 2016

Contents

List of Figures and Tables

List of Figures

List of Tables

Abstract

The influence of aerosols on climate is an important but still highly uncertain aspect in climate research. Using the atmospheric general circulation model ECHAM6-HAM the objective of this study is to quantify the aerosol effect over the decadal time scale in comparison to variability induced by varying sea surface temperature (SST) concentration taken from the atmospheric model inter-comparison project (AMIP) data base and the inevitable internal climate noise. This specific modeling setup allows for a quantitative estimation and separation of the stationary aerosol induced variability (AIV), transient SST induced variability (SIV) and the internal variability due to the large scale atmospheric instabilities and non-linearities using the methods of one-way and two-way analysis of variance (ANOVA). The ensemble data of aerosol optical depth (AOD) is analyzed with the help of one-way ANOVA. Furthermore, the two-way ANOVA is implemented on the data of the atmosphere radiative energy balance (AREB), temperature and large scale circulation like velocity potential (VP) and stream function (SF). The correlation coefficients method is used to determine a connection for the AIV and SIV with the 2m temperature.

The four ensemble model runs in this study are: no-aerosol, aerosol, HAM-full and HAM-dir. The model ECHAM6 without the HAM model estimated the no-aerosol and aerosol ensemble, where no-aerosol has no transient aerosol influence and aerosol utilized the aerosol climatological data. The HAM-full and HAM-dir ensemble both are simulated by utilizing the aerosol comparisons between observations and models (AEROCOM), they differ in the integration techniques used in HAM model. The HAM-full ensemble integrated the direct and indirect scheme, whereas the HAM-dir integrated only the direct effect of aerosols. A comparison is made between ECHAM6 and ECHAM6-HAM ensemble data of AOD. The dust burden of African aerosol particles and the industrial plume of the west China is well captured by the ECHAM6. Using the interactive aerosol scheme in HAM-dir ensemble, an additional anthropogenic aerosol plume towards the north of India is simulated in ECHAM6-HAM. The difference between these model realizations is due to the different aerosol micro-physics processes used in the HAM-model.

The satellite products like surface radiation budget (SRB), global precipitation climatology project (GPCP) are used for the validation of the model data. The model emission data is compared against the ERA-Interim. The model realizations for the global mean of planetary albedo (PA) is in good agreement with the SRB except for the HAM-model ensemble. However, the errors and uncertainties in global mean PA are propagating further into the global mean of TOA radiative energy balance (TREB) and surface radiative energy balance (SREB). Despite of this, the global mean of AREB for all model realizations is estimated with a reasonable accuracy. The imbalances in the global mean of PA, TREB and SREB is further investigated with the global mean of fresh water using GPCP and ERA-Interim data. However, the imbalances in radiative energy balance did not show any link with the latent heat flux but they are associated with the sensible heat flux. The zonal mean of radiative energy balance results explained how the errors or uncertainties are transferred from global to zonal mean scale.

The statistical technique ANOVA is used for the estimation of the local AIV, SIV and climatic noise variability. Reasonable SST signals are captured by all model runs for the AREB,

temperature and large scale circulation model data and the results of those signals are justified when analyzed by the correlation coefficients method. Therefore, it is concluded on the basis of these results that the real time forecast is only possible for the SIV and not for the AIV. It is recommended that the decadal climate forecast of SIV over the Pacific is possible by ECHAM6-HAM but with the same experiment setup as it has been done in this study.

1 Introduction

Recent reports published by the Intergovernmental Panel on Climate Change (IPCC) emphasize that atmospheric aerosol particles (AP) have a strong impact on the global climate by affecting the radiative energy balance (Houghton *et al.* 1996; IPCC 2013; Solomon *et al.* 2007). Compared to the pre-industrial time, during the last century the AP concentration increased dramatically. However, even nowadays quantitative estimates regarding the impact of aerosol particles on the global climate remain widely uncertain (Houghton *et al.* 1996). AP may either cool or warm the climate system by directly absorbing and scattering the solar and terrestrial radiation which is called the direct aerosol effect (Charlson *et al.* 1992). Moreover, AP may indirectly affect the climate since the formation of clouds is strongly controlled by the availability of AP serving as cloud condensation nuclei (CCN), thus modifying the optical properties of the clouds (Twomey 1977). The impact of this so-called indirect aerosol effect on the global climate is even less known than the direct aerosol effect.

One of the main reasons for our limited understanding of the impact of AP on the climate is given by the lack of our understanding regarding the major physico-chemical processes yielding the spatio-temporal heterogeneities of the AP distribution, such as AP formation processes (e.g. emission by soil dust, volcanoes, evaporation of sea spray, erosion, gas to particle conversion), micro-physical aerosol processes (e.g. collision-coalescence of aerosol, the interaction of aerosol with clouds) and AP sedimentation. While the physical properties of AP may be modified by changes of temperature, precipitation, wind speed or changes of the soil moisture, their chemical and biological properties are strongly linked to the concentration of atmospheric oxidants and the change in the vegetation cover (Chang, Park 2004). Hence, it is to be expected that atmospheric AP concentrations are characterized by strong spatio-temporal variations yielding the present large data uncertainties on different spatial (e.g. local, regional, global) and temporal (e.g. daily, seasonal, decadal) scales. However, in the last decades a distinct scientific progress has been made regarding our understanding of atmospheric AP so that in the IPCC fifth assessment report (AR5) the AP impact on the climate could distinctly better be described as compared to the fourth assessment report (AR4) (IPCC 2013; Solomon *et al.* 2007).

The aerosol size distribution is represented by the superposition of log-normal modes. These modes are divided into nucleation, aitken, accumulation and coarse modes. Nucleation mode has particles with radii less than 0.005 μm, aikten mode with radii 0.005 to 0.05 μm, accumulation mode with radii 0.05 to 0.5 μm and the coarse mode with radii greater than 0.5 μm (Whitby 1978). Among these size ranges, aerosol exist either as a separate particle or as in mixed composition. The mixed composition belongs to internal mixture or external mixture. The internal mixture contains the uniform mixture of the individual solute. And the external mixture is made of solely one solute. In the atmosphere, internal aerosol mixture plays a more dominant role as compared to external aerosol mixture. For example, biomass burning and soot can mix with the other aerosol species (McFiggans *et al.* 2006). The cloud albedo indirect effect is estimated negative for the internally mixed sea-salt, mineral dust, black carbon (BC), organic carbon (OC) and sulfates (Chuang *et al.* 2002; Lohmann *et al.* 2000). The size distribution, composition and mixing state of aerosol are determined by their moment of emission or formation and combination of subsequent micro-physical and chemical transformation processes (Brasseur *et al.* 2006). In accumulation mode, the dry aerosol have diameter 0.1 to 1 μm and the hydrate aerosol have diameter 0.1 to 2 μm. Extinction due to hydrate aerosol is larger than the dry aerosol (IPCC 2001; Schwartz 1996).

Aerosol nucleation in the atmosphere is a complex and important process. Several kinds of nucleation processes are involved, but it is harder to find which one is dominating in the atmosphere. The size of local-aerosol grow continuously from 1 to 20 nmh^{-1} and the nucleation rate varies between the 0.01 to 10 particles $cm^{-3}\mathrm{s}^{-1}$. Atmospheric aerosol nucleation strongly depends on the chemistry (e.g. sulfuric acid and some low volatility gases), organic species and iodide compounds over the coastal areas. This nucleation process can be affected by solar radiation and mixing processes within the boundary layer. Scientists categorized four main kinds of atmospheric nucleation processes (i) Homogenous nucleation (e.g. binary mixture of water and sulfuric acid from the industrial plume) (ii) Homogenous ternary nucleation (e.g. mixture of water, sulfuric acid and ammonia from the continental boundary layer areas) (iii) Ion induced nucleation (e.g. from binary, ternary and organic vapors in the upper troposphere and lower stratosphere) (iv) Homogenous nucleation due to Iodide (e.g. In the coastal areas) (Kulmala *et al.* 2004).

In climate models, aerosol particles are usually treated in five lumped groups, i.e. sea salt particles, mineral dust, sulfate, BC and OC. Certainly, over oceanic remote areas sea salt aerosol are dominant yielding 55 to 75 % of the total aerosol mass. Over continental regions, mineral dust is the most important aerosol component having total aerosol mass up to 30 % of the continental atmosphere. For sulfate, the mass fraction is around 10 to 30 %, except for the urban regions of Oceania, rural African regions and the south America. OC contributes to the total aerosol mass by around 20 %, having its highest concentrations in north and south America. The smallest contribution of about 5 % to the total aerosol mass is due to BC, however, in the last decades this value increased up to 13 % in the urban African regions, Europe, Asia and the south America (Jimenez *et al.* 2009; Zhang *et al.* 2012).

Depending on their formation mechanisms one speaks either of anthropogenic or natural AP. Sea salt and mineral dust particles belong to natural aerosol whereas sulfate and carbonaceous aerosol are mainly of anthropogenic origin. Owing to their strong hygroscopicity, sea salt particles are relatively large (Textor *et al.* 2006). Since they absorb almost no solar or infrared radiation, their impact on the global climate is mainly given by a cooling effect, resulting from the back-scattering of the incoming solar radiation into space. Global estimates of the annual sea salt emission are around 1000 to 35000 Tgyr^{-1} (Granier *et al.* 2004; Raes *et al.* 2000). Mineral dust particles scatter the solar radiation and absorb infrared radiation. The global annual dust emission rates are in the order of 1100 to 3000 Tgyr^{-1} (Penner *et al.* 2001; Raes *et al.* 2000; Zender *et al.* 2004). Similar to sea salt particles, sulfate aerosol do almost not absorb atmospheric radiation, but they scatter the incoming solar radiation back to space. Natural sources of sulfate are volcanic emissions while anthropogenic sources are the emission of sulfur dioxide with subsequent oxidation to sulfate. Total sulfur dioxide emission rates are estimated to range between 92 to 144 Tgyr^{-1} (Forster *et al.* 2007; Granat *et al.* 1976). OC particles scatter and absorb solar radiation. Their global annual budget is about 6 to 22 Tgyr^{-1} (Bond *et al.* 2004). BC particles strongly absorb solar radiation, yielding a clear warming impact for the global climate. The currently estimated global annual budget for BC is about 8 Tgyr^{-1}. The main sources for BC and OC are fossil fuel and bio-fuel burning (Bond *et al.* 2004; Huang *et al.* 2013). AP can be removed from the atmosphere by sedimentation, wet and dry deposition (IPCC 2013). Sea salt and mineral dust particles have much shorter atmospheric lifetimes than BC and OC. Since the impact of AP on the radiation budget is strongly controlled by the AP concentration, in climate models the numerical parametrization of aerosol source and sink processes is of crucial importance (Feng 2008; Kerkweg *et al.* 2006; Petroff, Zhang 2010).

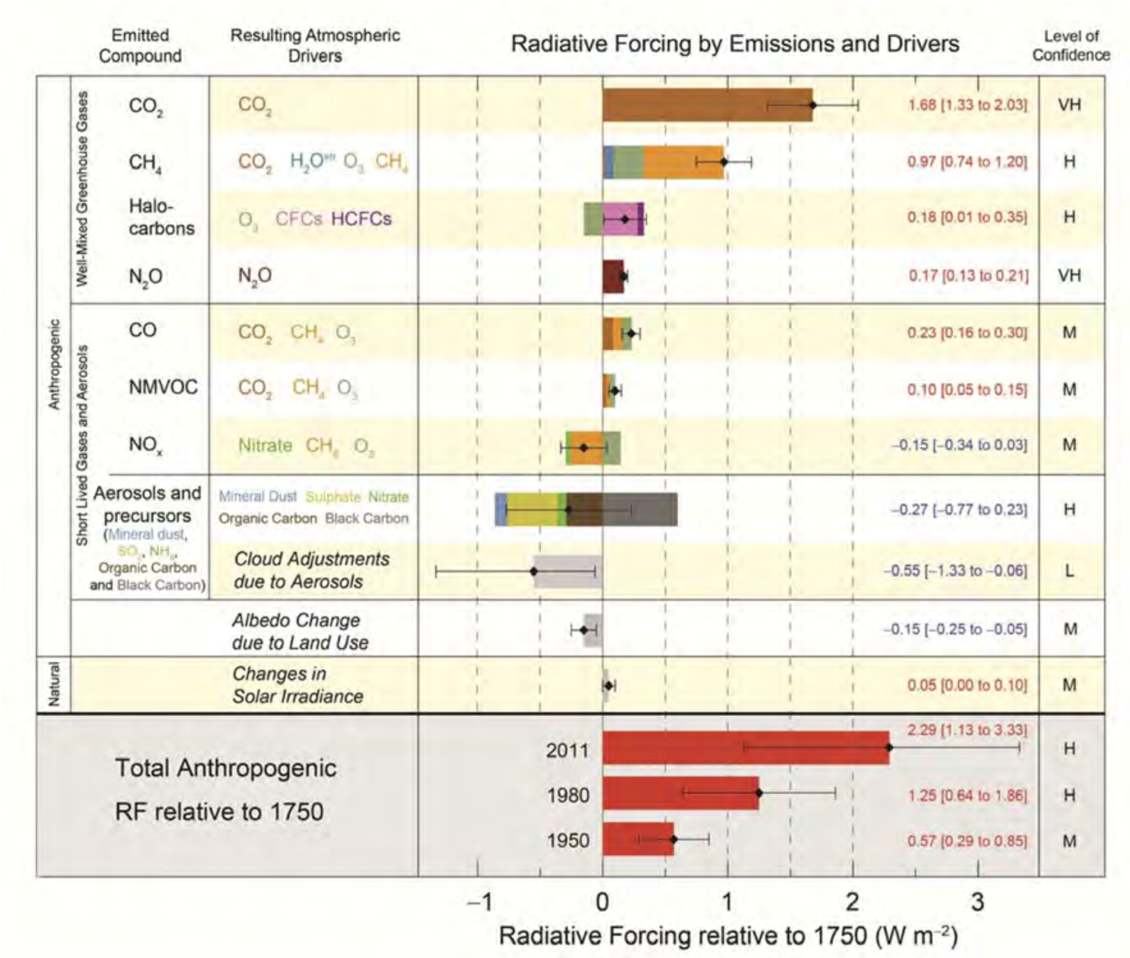

Figure 1.1: A comparison between the greenhouse gases and aerosol radiative forcing with aggregated uncertainties. The values are estimated for the global average radiative forcing in 2011 relative to 1750. The numerical values are shown on the right side of this plot with a confidence level in net forcing (VH–very high, H–high, M–medium , L–low). The black carbon aerosol bar contains the information about the albedo forcing due to black carbon on snow and ice. The bottom portion of the plot provides the information about the total anthropogenic radiative forcing for the three different years relative to the 1750. This Figure is the part of IPCC-fifth assessment report AR5 (2013).

Aerosol affect the balance of visible and infrared radiation in the land-atmosphere system. This is known as aerosol radiative forcing (RF). It can be defined in different ways: first, it is the changed in the net flux at the tropopause; second, it is the changed in energy balance of earth-atmosphere due to the greenhouse gases and aerosol and third, It is also defined as the change in energy per unit area of the globe as measured from the top of the atmosphere (Forster *et al.* 2007; WMO 1986). The RF is also categorized for the direct and indirect effect of aerosol. In Figure 1.1, a comparison between the aerosol RF and the greenhouse gases

(GHG) is estimated in 2011 relative to 1750. The climate forcing of anthropogenic AP can offset the warming caused by the GHG, such as carbon dioxide and methane. The RF due to anthropogenic AP is estimated to be in the order of -2.5 to 0.1 $W{\cdot}m^{-2}$, thus approximately offsetting the present greenhouse gas radiative forcing, which is estimated as 0.5 to 3.0 $W{\cdot}m^{-2}$. However, in contrast to the greenhouse gas RF the AP radiative forcing has a medium to low level of scientific understanding.

For shortwave radiation the so-called aerosol radiation interaction (ARI) is typically negative varying between -4 to -6 $W{\cdot}m^{-2}$ at the top of the atmosphere (TOA), but it becomes positive with absorbing aerosol (Chand *et al.* 2009). While at the earth's surface ARI is negative as well (Li *et al.* 2010), at the TOA it is positive only over the Arctic ice surfaces (Stone *et al.* 2008). In contrast to this, the longwave radiation interaction of AP is positive at the TOA. This phenomenon is mainly caused by sea-salt, desert dust and stratospheric AP (McCormick *et al.* 1995; Reddy *et al.* 2005). Within the troposphere, absorbing aerosol modify the static–stability (Babu *et al.* 2011; Wendisch *et al.* 2008). For individual aerosol species the direct RF is less certain than the total or combined aerosol effect. The direct RF is estimated to be -0.65 $W{\cdot}m^{-2}$ for sea salt particles, -0.08 $W{\cdot}m^{-2}$ for mineral dust, -0.4 $W{\cdot}m^{-2}$ for sulfate, -0.02 $W{\cdot}m^{-2}$ for OC and 0.43 $W{\cdot}m^{-2}$ for BC (Ma *et al.* 2008; Stier 2004). Owing to rather poor instrument calibration and data development techniques, the data concerning the optical properties and size distribution of AP show significant uncertainties (Baumgardner *et al.* 2012; Moosmüller *et al.* 2009). For the radiative properties of the AP these uncertainties are for the single scattering albedo ± 0.07 over ocean and ± 0.02 over land, for the aerosol optical depth 0.05 and for the asymmetry factor -0.61 to -0.08. Combined with the uncertainties of the aerosol size distributions and of the AP vertical profiles this yields an overall uncertainty in ARI of up to 0.5 – 1.0 $W{\cdot}m^{-2}$ (Loeb, Su 2010; McComiskey *et al.* 2008; Zarzycki, Bond 2010).

Presently there exist only few General Circulation Model (GCM) studies on the aerosol radiative effects. Takemura *et al.* 2005 pointed out a negative global mean direct and indirect radiative forcing of AP. Oldenborgh *et al.* 2012 analyzed multi-model ensemble runs for the decadal climate prediction. Their study mainly focused the stratospheric aerosol predictability comparing to the sea surface temperature (SST) variability over the north Atlantic and Pacific ocean. Stier 2004 developed a aerosol micro-physics model (HAM) and coupled it to the atmospheric component of the ECHAM6 (GCM). His major findings are related to the aerosol interaction with the clouds (i.e. semi-direct effect) and he investigated the behavior of different aerosol species using the HAM-model. Koch *et al.* 2009 utilized the Goddard Institute for Space Studies GCM and conducted the experiments with and without changing greenhouse gas (GHG) concentration and they also estimated the aerosol direct and indirect effect. In their model simulation with fixed GHG concentration, they observed that the surface air temperature was changed by $-0.2\,^{\circ}C$ to $-1.0\,^{\circ}C$ and for the direct and indirect aerosol effect the temperature was changed by $0.2\,^{\circ}C$. They assumed that an increase in GHG concentration had no influence on the indirect aerosol effect, but it reduced the aerosol to climate effect on the surface air temperature by 20 % and for the snow or ice cover by 50 %. Ayash *et al.* 2007 used the Canadian aerosol module and estimated the direct and indirect shortwave radiative effect of sea salt aerosol. They found that over the southern ocean the sea salt aerosol have a significant direct radiative effect. Adams, Seinfeld 2002 coupled a two-moment aerosol sectional model in a GCM. They found an increase of atmospheric aerosol number concentrations with height and a distinct land to sea contrasts in the aerosol mass and size distributions. Feichter *et al.* 2004 integrated the ECHAM4 with a thermodynamic sea ice model and they found that the combined effect of aerosol and GHG was weaker than the sum of the individual effects.

Most of these research papers focus on the numerical treatment of aerosol radiative effects, the focal point of this study is to evaluate the global aerosol direct and indirect effect, statistically. For this purpose the ECHAM6-HAM model extended with the land vegetation model JSBACH (Jena Scheme for Biosphere-Atmosphere Coupling in Hamburg) is integrated with prescribed SST data.

IPCC (AR5) report deals with different carbon and bio-geochemical processes, aerosol direct and indirect effects, changes in anthropogenic and natural radiative forcing as well as the evaluation of climate models and climate predictions, but on time scales of 50 to 100 years (IPCC 2013). In contrast to this, the main goal of the German climate project (Medium range climate prediction) MiKlip is to develop and provide a model system that produces reliable decadal climate forecasts, including extreme weather events. MiKlip was started in late 2011. It evolves the statistical properties of the global and regional climate from the output of numerical models, mainly from the Max Planck Institute of Earth System Model (MPI-ESM). These models can assimilate the observations and can be integrated either for a single or multiple ensemble on the time scale of ten years. The decadal predictions by these models are based on accurate initial conditions, a detailed modeling of different cryosphere and biosphere processes, an increase in the spatial model resolution, statistical post-processing and a validation of all model systems (MiKlip 2011). Within the MiKlip project, this study will participate for the quantification of the aerosol climatic effects over the ten years time scale.

There are certain limitations associated within the global aerosol models. For example, their sink and radiative properties, chemical reactivity, water uptake depends on the aerosol size distribution, composition and mixing state. However, aerosol size distribution is not a prognostic parameter and therefore has to be prescribed. The aerosol mixing state is not constant quantity for different emission levels. Violation of these justification no matter under any climatic and environmental condition affect the aerosol radiative effect. In fact, the indirect effect of these bulk aerosol models is highly sensitive to changes in the size distribution. Aerosol mixing state is not a prognostic variable, therefore the global radiative effect gives an additive radiative effect of externally mixed aerosol populations. Aerosol water uptake is mainly used to calculate the aerosol radiative properties in most of aerosol models. However, it significantly affects the aerosol mass, sink processes and global aerosol distribution (Stier 2004).

1.1 Decadal climate prediction

The term forecast was introduced by Fitzroy in 1863 when he started to investigate the loss of a ship in a storm in 1859. And the word prediction was used by Richardson 1922. He first discussed how to do weather forecast by solving the differential equations numerically. The term prediction refers to estimate the scenarios of the future climate and it depends on the externally forced climatic response (e.g. greenhouse gas and aerosol variability) to a particular emission scenario. In case, when the climate scenarios are predicted over the ten or twenty years then this represents the decadal climate prediction or the short term climate system. Technically, the decadal prediction is considered as an expensive technique, because it mainly involves the high resolution models for the improved simulation results of both regional and climate extremes, such as tropical cyclones and extreme precipitation (Gualdi *et al.* 2008; Kimoto *et al.* 2005). Similarly, when the climate scenarios are studied for more than 50 years then these scenarios are known as the long term climate system. The results of long term climate prediction of different physical objects (e.g. radiation energy balance and temperature) are presented in the IPCC reports (IPCC 2013).

Climate change scientists raised the concern among the policy makers regarding an increase in hurricane activity over the tropical Atlantic, prolonged drought in southwest America, extreme events (European heatwave in 2003), changes in the fisheries regimes and the rise of temperature since the 1990s. These physical quantities are quite well assessed on the decadal time scale. They also affect the economic growth and environmental scenarios, and they are consistent with the climatic simulation of the twentieth and twenty-first century of some models (Seager *et al.* 2007). Meaningful decadal prediction was started in 2007, when many scientists started to use the coupled models and focused on the forced response of the climate system to the external forcing, such as greenhouse gases and aerosol (Keenlyside *et al.* 2008; Meehl *et al.* 2009; Pohlmann *et al.* 2009; Smith *et al.* 2007).

The main objective of this study is to quantify the global tropospheric aerosol variability as the basis for the higher accuracy estimates of the aerosol effect. The approach to solve this problem is threefold. First, the model data will be validated against the different observational data. Second, the model data will be analyzed by using a statistical scheme (i.e. ANOVA). Third, a theoretical background will be established for the decadal aerosol climate variability.

1.1.1 Outline

This study is organized around seven main sections. The overall outline of the study is given below; Chapter-1 mainly contains the information about the aerosol micro-physics, aerosol processes, aerosol chemistry. Models description, data, experiment design is briefly discussed in Chapter-2. Model data is validated against the observations in Chapter-3. Statistical theories are reviewed in Chapter-4. Results are examined and interpreted in Chapter-5. Physical reasoning of the results are investigated in Chapter-6. This study is concluded in Chapter-7. The sketch of all these chapters are shown in Figure 1.2.

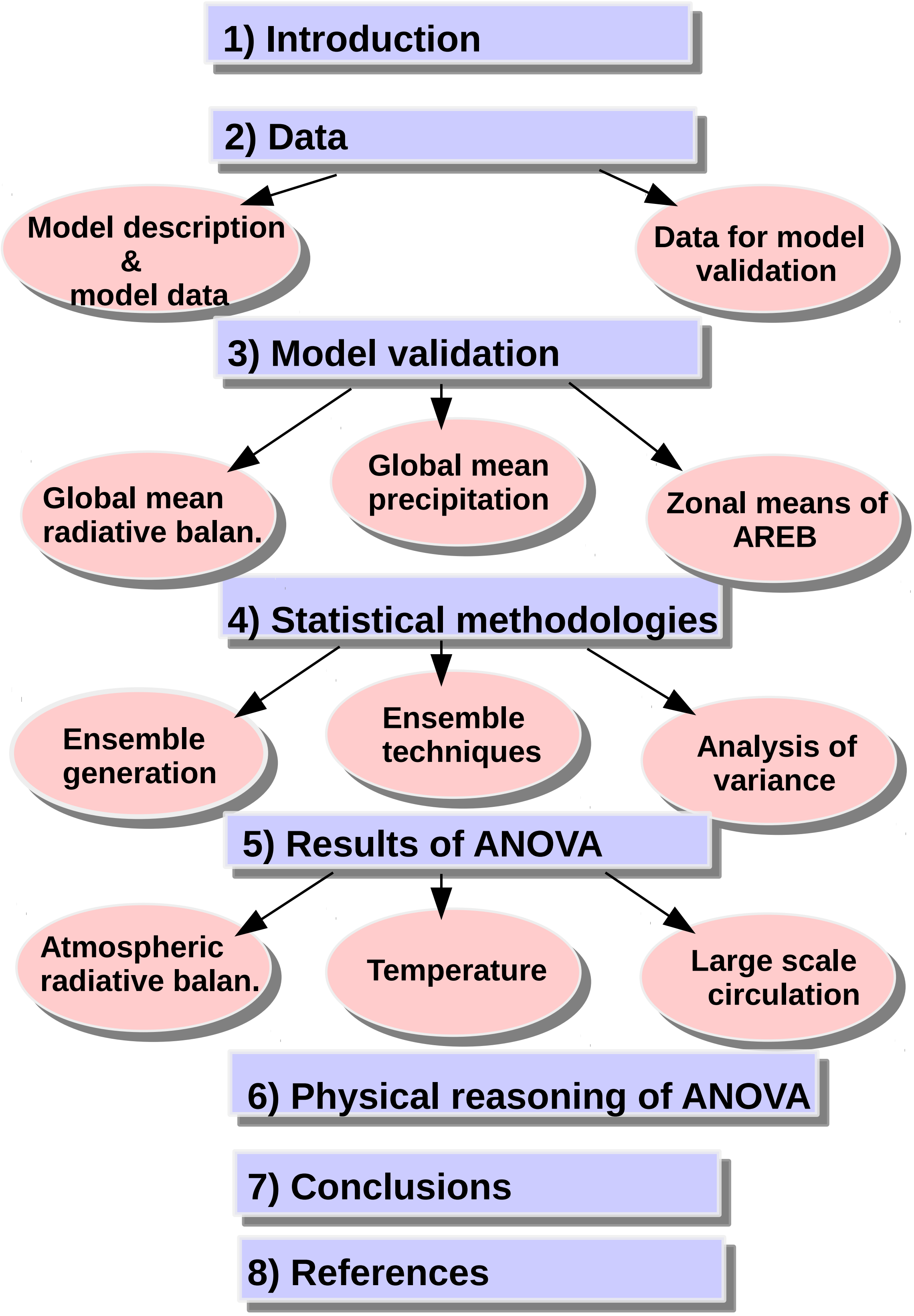

Figure 1.2: Dissertation flow–chart

2 Model description, data and experiment design

This chapter consists of four sections: (2.1) model description (2.2) data for model initialization (2.3) data for model validation and (2.4) experiment design. The ECHAM6 includes the land surface model JSBACH, aerosol model HAM and aerosol micro-physics model M7. The model is initialized with the Hadley center sea surface temperature (SST), greenhouse gases (GHG), solar irradiance and aerosol climatological data. The surface radiation budget (SRB) data is used for making a comparison against the model radiative energy balance data. The model water cycle is validated against the global precipitation climatology project (GPCP) data and the model evaporation data is analyzed against the ERA-Interim data. The experiment design is based on the four different ensemble which will be discussed later in this chapter. Each of these ensemble utilized a different aerosol scheme.

2.1 Model description

The MPI-ESM couples the ocean model with an atmospheric and land surface model. It has been mainly used for the coupled model intercomparison project phase–5 and it constituted the German contribution for the IPCC fifth assessment report (IPCC 2013).

The recent MPI-ESM setup contains an atmospheric general circulation model. The atmospheric component of the ECHAM6 was explained in Stevens *et al.* 2013. For this research, ECHAM6 is integrated with the land vegetation model JSBACH and the aerosol model HAM. The HAM model was briefly explained in Zhang *et al.* 2012.

2.1.1 ECHAM6

The model ECHAM6 is a general circulation model (GCM) and it belongs to the sixth generation of Echam. It has been developed by the Max Planck Institute for Meteorology in Hamburg, Germany. The original model code belongs to the European Center for Medium Range Weather Forecasts (ECMWF) (Roeckner *et al.* 1996). ECHAM6 is a large scale circulation model based on the diabatic processes which are derived by the radiative forcing. The model solves the primitive equations for the divergence, vorticity, temperature and surface pressure. The dynamical core of ECHAM6 is expanded in the spherical harmonics. The vertical coordinates of the model used the usual terrain following the sigma levels in the lower troposphere and the pressure levels in the middle and the upper atmosphere (Giorgetta *et al.* 2006; Manzini *et al.* 2006; Phillips 1957; Simmons, Burridge 1981).

The flux of the trace components like water vapour, cloud liquid water and cloud ice is transported by a semi-Lagrangian scheme onto the regular Gaussian grid (Eliasen *et al.* 1970; Lin, Rood 1996; Machenhauer, Rasmussen 1972; Orszag 1970). The turbulent kinetic energy in ECHAM6 separates the full flow into resolved mean-flow and unresolved turbulent eddies by Reynolds averaging. The turbulent kinetic energy causes the exchange of momentum between the atmosphere, ocean and land (Brinkop, Roeckner 1995). The cloud cover is obtained from a function of grid-mean relative humidity (Sundqvist *et al.* 1989). Tiedtke 1989 mass flux scheme is applied for the calculation of the convective cloud scheme and the convective transport. It was modified by Nordeng 1994.

The radiative transfer model used in ECHAM6 is an updated version of the rapid and the accurate radiative transfer model (RRTM). It contains the shortwave (SW) and longwave (LW) radiative schemes. The RRTM-SW is based on 14 spectral bands and RRTM-LW has 16 spectral bands (Giorgetta *et al.* 2012).

2.1.2 Land vegetation model (JSBACH)

The JSBACH is a land vegetation model, which is integrated in the ECHAM6. The land model helps the exchange of energy and water from surface to the atmosphere. It is a dynamical vegetation model with 12 plant types. The JSBACH computes the land-surface albedo and includes a consideration of the snow on soil, bare surfaces, the canopy effect and the forest masking. In addition to this, it also includes the carbon storage in the plants, photosynthetic activity of the plants, and the soil respiration. A hydrological discharge model is a part of JSBACH. It provides the river runoff to the oceans (Giorgetta *et al.* 2012; Stevens *et al.* 2013).

2.1.3 Aerosol model (HAM)

The ECHAM6 setup used for this research has an aerosol model HAM version 2.1. Table 2.1 is showing that the HAM model has seven aerosol modes based on less or no water solubility and it is denoted as an insoluble mode. The internal mixture of soluble and insoluble compounds is representing the soluble mode. It contains the five internally and externally mixed components: sulfate, black carbon, particulate organic matter, mineral dust and sea salt aerosol. The size distribution of aerosol has seven log-normal modes with a prescribed variance (Vignati *et al.* 2004). Several emission inventories of these aerosol are briefly described in Zhang *et al.* 2012. The insoluble BC aerosol are emitted by the aircraft, ships, vegetation fire, fossil-fuel and bio-fuel. The POA both in soluble and insoluble states are emitted through the biomass burning and fossil fuel emission. The Sulfate (SO_4) particles are emitted by the ships, public transport, industrial waste and by the volcanic eruption. It is further categorized into the soluble aitken, soluble accumulation and the soluble coarse modes. The SOA is emitted through the biogenic emission and it is divided into the soluble and the insoluble aitken modes. Some SOA emission is distributed into the soluble accumulation mode.

The chemistry module of HAM is based on the sulfur cycle model. The dimethyl sulfide (DMS), sulfur dioxide (SO_2) and sulfate (SO_4) are the prognostic quantities of the chemistry module. The HAM deposition module investigated the dry and wet deposition and sedimentation processes. The aerosol dry deposition velocity is a function of turbulence and particle radius. The aerosol wet deposition prescribed a scavenging parameter R, which depends on the size and the composition of aerosol. The scavenging parameter represents the cloudy part of the grid-box which is ingrained in the cloud liquid water. The calculation of sedimentation for the aerosol particle is based on the Stokes velocity (Stier 2004).

The general differences of aerosol micro-physics between HAM1 and HAM2.1 is listed in Table 2.2. It refers to the specific HAM1 configuration explained in Stier 2004. A modified configuration of HAM2.1 model is described in Zhang *et al.* 2012.

Table 2.1: HAM2.1 modal components

Aerosols size distribution	Soluble/mixed	Insoluble
Nucleation mode (r < 0.005 µm)	Aerosols mode-1 Sulfur Nuceleation soluble (NS)	
Aitken mode (0.005 µm < r <0.05 µm)	Aerosols mode-2 Sulfur (SU), Black carbon (BC), Primary organic aerosols (POA), Secondary organic aerosols with Isoprene oxidation (SOA-I1 and SOA-I2), SOA with Monoterpene oxidation (SOA-M1 and SOA-M2), SOA with anthropogenic precursors (SOA-AT). Aitken soluble (KS)	Aerosols mode-5 BC, POA, SOA-I1, SOA-I2, SOA-M1, SOA-M2, SOA-AT. Aitken insoluble (KI)
Accumulation mode (0.05 µm < r < 0.5 µm)	Aerosols mode-3 SU, Dust (DU), POA, BC, Sea salt (SS), SOA-I1, SOA-I2, SOA-M1, SOA-M2, SOA-AT. Accumulation soluble (AS)	Aerosols mode-6 Dust Accumulation insoluble (AI)
Coarse mode (r > 0.5 µm)	Aerosols mode-4 SU, DU, POA, BC, SS, SOA-I1, SOA-I2, SOA-M1, SOA-M2, SOA-AT. Coarse soluble (CS)	Aerosols mode-7 Dust Coarse insoluble (CI)

Table 2.2: An overview of the aerosol microphysics in HAM1 and HAM2.1 setup (Zhang et al. 2012)

Aerosol microphysics	HAM1 setup	HAM2.1 setup
Aerosol nucleation	The Vehkamäki et al. (2002) is used as a default scheme.	The new scheme of aerosol nucleation is included by Kazil et al. (2010). Vehkamäki et al. (2002) can still be used as an optional scheme.
Sulfuric acid gas	The sulfuric acid gas can not distinguish between cloudy and cloud free part of model grid box.	Analytical solution for the condensation is included by Kokkola et al. (2009). The complete removal of sulfuric acid gas from the cloudy part of model grid box is described in Kazil et al. (2010).
Dust emission	The dust particles is interactively calculated by the Tegen et al. (2002).	East Asia soil properties are updated by the Cheng et al. (2008).
Sea salt emission	The emission of the sea salt particles with the radius range of 2 to 4 µm is included by Stier et al. 2004.	The particle radius between the size range 2 to 4 µm are included by the Monahan et al. (1986).
Atmospheric dynamics	The microphysics of the stratiform cloud is included by the Lohmann and Roeckner (1996) scheme. And the solar radiation scheme is calculated by Fouquart (1980).	Two-moment stratiform cloud microphysics scheme of Lohmann et al. (2007) is used here and the solar radiation scheme is updated by the Cagnazzo et al. (2007).
Aerosol water uptake	The aerosol water uptake considers only the non-organic aerosols by Zeleznik (1991); Stokes and Robinson (1996).	For HAM2, it considers the non-organic and the organic aerosols scheme, based on the k-Köhler theory (Peters and Kreidenweis, 2007; O'Donnell et al. 2011).

2.1.4 micro-physics model-M7

The aerosol microphysical core M7 is an aerosol module of the HAM model (Vignati *et al.* 2004). It calculates the coagulation coefficients and condensation processes following Fuchs 1959, 1964. The nucleation in M7 accounts the effect of the hydratisation and the number of nucleated sulfate particles which are parametrized by Vehkamäki *et al.* 2002. The sea salt particles grow spontaneously with increasing ambient relative humidity (RH) and they do not release the water until the RH falls below the 45 % level (Tang *et al.* 1997). This is known as the Efflorescence Relative Humidity in M7.

2.2 Data for the model initialization

This section is divided into the three sub-sections: (2.2.1) data for the boundary conditions (2.2.2) aerosol climatological data and (2.2.3) aerosol emission in HAM model.

2.2.1 Data for the boundary conditions

The historic SST and SI data is taken from the program for the climate model diagnosis and intercomparison archive and remapped to the ECHAM6 grid. The basic SST data is based on monthly means and it is obtained from Hadley center (Hurrell *et al.* 2008). The parameters for the surface orography are the slope σ, the orientation θ, the standard deviation μ, the anisotropy γ and the minimum, maximum and mean elevation Z. These parameters (σ, θ, μ, γ) are calculated offline and the elevation Z is formulated from the US Navy (10×10) topographic dataset (Baines, Palmer 1990).

The concentration of the well-mixed GHG has been provided by the international institute for applied systems analysis (i.e. IIASA) as a global mean time series. The CO_2 concentration is assumed to be constant in the model atmosphere. The water concentration of the middle atmosphere is influenced by the photo-dissociation and oxidation of the methane (Schmidt *et al.* 2012). A three dimensional ozone climatological data is taken from Cionni *et al.* 2011 and Eyring *et al.* 2010. The satellite data of moderate resolution imaging spectroradiometer is used for the calculation of soil albedo (Hurtt *et al.* 2011; Ramankutty, Foley 1999). The plant functional type of JSBACH is explained in Pongratz *et al.* 2008 and the field capacity in Hagemann 2002. The total solar irradiance variation is reconstructed by Fröhlich, Judith 2004 and it is based on the time series of sunspots. The spectral dependence on the solar irradiance is described in detail by Lean 2000.

2.2.2 Aerosol climatological data

The climatological data of aerosol in ECHAM6 is categorized as tropospheric and stratospheric aerosol. The ECHAM6 utilizes a built in aerosol scheme of Kinne *et al.* 2006. The explanation of HAM-model aerosol in Sections 2.1.3 and 2.1.4 is linked with the interactive aerosol and aerosol microphysical processes. In ECHAM6, the tropospheric aerosol are separated into fine and coarse modes, with a distinct radius difference of 0.5 μm. The coarse mode aerosol particles (AP) are normally emitted from the natural sources and they are further divided into the dust and sea salt aerosol family. The fine mode AP are assumed to be emitted by natural and anthropogenic sources. The ECHAM6 consists on the sulfate, organic and black carbon aerosol. The tropospheric aerosol data is taken from the Kinne *et al.* 2006. This aerosol data is based on the climatology of aerosol optical depth, single scattering albedo and Angström exponent in the vertically integrated column. The fine and the coarse mode aerosol are splitted by ground based aerosol robotic network data and calibrated to climatology as a whole. The stratospheric aerosol data set includes the extension of the Pinatubo dataset and it covers the entire period between 1850 and 1999 (Stenchikov *et al.* 1998).

The previous model versions of Echam utilized the aerosol optical properties developed by Tanre *et al.* 1984 and GADS climatology by Koepke *et al.* 1997. However, these aerosol climatologies had some limitations. The Tanre climatology neglects the Saharan dust seasonal variations which is associated with relatively strong absorption. The GADS climatology was based on the in situ dried sample analysis. This introduced uncertainties, because aerosol are assumed to uptake the water. Another GADS limitation was linked with the data coverage. It had simulated the data just over 2 months, which was inadequate to capture the seasonality.

The Max-Planck-Institute climatology (MAC-v1) attempted to overcome these shortcomings by offering the maps with a longitudinal and latitudinal resolution of $(1 \times 1)^{\circ}$. The MAC-v1 calculated the aerosol optical properties by using the sun or sky photometer robots. It also included the complementary data of the aerosol extinction, aerosol back-scattering profiles and the aerosol vertical distribution by the co-located LiDAR (Aoki 2006; Sugimoto *et al.* 2008; Welton *et al.* 2001). The sun or sky photometer led to more mature satellite retrieval and reduced the diversity of the simulated aerosol optical depth (AOD) in the global models. During the last 15 years, new satellite sensors offer global maps for the AOD. Despite of the sun or sky photometer, the data used from the satellite sensors was usually derived from the changes in the solar reflectance. The MAC-v1 aerosol climatology was based on the monthly mean ensemble and it was also used as an input for the global aerosol emission (Dentener *et al.* 2006; Kinne *et al.* 2006).

2.2.3 Emission inventory of HAM

The emission in ECHAM6-HAM is assumed to mix homogeneously across the model grid box with typical scale of around 100 km. The emission of sea salt and dust is interactively computed by using the techniques of Tegen *et al.* 2002 and Guelle *et al.* 2001, respectively. In HAM-model, the SO_2, SO_4, black carbon and primary organic aerosol is prescribed by the aerosol comparisons between observations and models (AEROCOM) project. The natural emission of dimethyl sulfide is computed online (Kloster *et al.* 2006). The terrestrial emission of dimethyl sulfide is taken from Pham *et al.* 1995.

2.3 Data for the model validation

The model atmospheric radiative energy balance (AREB) data will be validated against the SRB data. The model water cycle will be compared with the GPCP data and the model evaporation data will be with the ERA-Interim data.

2.3.1 Surface radiation budget data (SRB)

The SRB data is available between 1983 to 2007 and the data is downloaded from this website $https://eosweb.larc.nasa.gov/project/srb/srb_table$. The model estimated shortwave and longwave radiation budgets are within the time frame of SRB data. The SRB cloud parameter data is derived by the international satellite cloud climatology project. The ozone column dataset is obtained from the archive of the total ozone mapping spectrometer and it is calculated between 1983 to 2004. The temperature and moisture data is taken from the Goddard EOS data assimilation system (Bloom *et al.* 2005). The surface emissivity data is obtained by the NASA-LaRc project (Wilber *et al.* 1999). The SRB data identified some known data irregularities like the Indian ocean gap artifacts and satellite calibration shifts.

The uncertainty of the downward shortwave radiative flux of the Indian ocean region is estimated as 60 W m^{-2}. The uncertainty range for the longwave radiative flux is computed between 20 W m^{-2} for top of atmosphere (TOA) and 5 W m^{-2} for the surface flux. The satellite calibration affected the calculation of the SRB data from 2006 to onwards, and it caused a strong gradient in the surface albedo over the planet. However, the surface downward flux are less affected due to this. The satellite calibration error may persist when the long time series are computed by the SRB data.

For the model data validation, the SRB data is averaged over the time period of 1995 and 2004. The data resolution is 1.0° latitude and 1.0° longitude. In all sky conditions, the root mean square value for the monthly averaged shortwave flux is estimated between -5.2 W m^{-2} to 23.3 W m^{-2} (Zhang *et al.* 2013).

2.3.2 Global precipitation climatology project data (GPCP)

The model data is analyzed against the GPCP data for the water cycle estimation. The data of the total precipitation is obtained by the GPCP. This data is based on the monthly estimate of the precipitation at $(2.5 \times 2.5)^\circ$ latitude-longitude resolution from 1979 to present. Over the tropical and sub-tropical range, the precipitation estimate is calibrated using a lower orbit satellite special sensor microwave imager data and the geosynchronous-orbit-satellite data. At the higher latitudes, special sensor microwave imager data is combined with the atmospheric infrared sounder. A complete global satellite precipitation is estimated this way.

The GPCP data became available from the world data center of national oceanic and atmospheric administration (i.e. NOAA) and online at $http://precip.gsfc.nasa.gov$. The absolute magnitude of the GPCP products is reliable and the inter-annual changes are robust. However, due to data inhomogeneity, the trends and other small signals should be interpreted cautiously. Especially the precipitation might be underestimated in the mountainous regions (Adler *et al.* 2003; Huffman *et al.* 2009).

2.3.3 ERA-Interim data

The evaporation data is taken from the ERA-Interim archive of the ECMWF. The data for the evaporation is downloaded via the ECWF data server $http://data.ecmwf.int/data$.

This work does not account aerosol indirect effect. It only considers the global aerosol direct and full aerosol effect (i.e. direct and indirect). The indirect effect (e.g. clouds micro-physics, aerosol chemistry) is proved to be important in IPPC reports. Although the IPCC fourth assessment report predicted that the first global aerosol indirect effect is large in the magnitude, but the uncertainties associated to this are even larger (Lohmann, Feichter 2005). The ECHAM6-HAM does not completely conserve the energy therefore model identified persistent error in the cloud scheme, which eventually affects the energy balance of the atmosphere. These errors or biases can be extended over the larger scale and they can be associated with a poor representation of aerosol effects (Stevens *et al.* 2013).

2.4 Experiment design

By using atmospheric general circulation model ECHAM6-HAM, the objective of this study is to quantify the aerosol impact over decadal time scale in comparison to the variability induced by the varying sea surface temperatures (SST) concentration taken by the AMIP data base and the inevitable internal climate noise.

As it has been discussed already in the Introduction part of Chapter-1, the aerosol response to climatic variability is as an important factor. The IPPC fifth assessment report pointed out the uncertainty in estimating the aerosol response for the climate variability. Both the direct and indirect effect of aerosol in IPPC report are evaluated from low to medium scientific understanding compared to GHG concentration. However, IPCC roughly determines the aerosol climatic effect over 50 to 100 years. In MiKlip, the main concept is to develop a system for decadal climate prediction over 10 to 20 years by the climate models. The contribution of this study for the MiKlip is to the quantify aerosol effect over the decadal time scale.

The spatial resolution of the model is set to T63 in spectral space and model one grid box has more than 100 km in length and breadth (i.e. 1.89°). Overall, model has 192 longitudinal and 96 latitudinal grid points. The model vertical resolution is set to 47 levels from the surface up to 0.01 hPa. Four ensemble of sample size ten, each have been created by starting the integration on January 01, 1995 until December 31, 2004 with ten different initial conditions derived from the four control runs over 14 years.

The experiment setup is presented in Table 2.3. The Model initial state is not perturbed for the control experiment but it is perturbed for the ensemble run. The first two ensemble no-aerosol and aerosol simulated the data, when the HAM-model is switched off. The remaining two ensemble HAM-full and HAM-dir are taken into account the aerosol physics of HAM-model. The details of these four ensemble for the ten year time period 1995-2004 is given below:

- A ten member no-aerosol ensemble is based on the observed monthly mean sea surface temperature for 1995-2004 without any aerosol influence. This ensemble served as the background ensemble to characterize the SST effect or the ideal ocean verses the internal climatic noise.

- A ten member aerosol ensemble is based on the observed monthly mean sea surface temperature and it additionally utilized the time varying data sets of the aerosol optical properties like aerosol optical depth, single scattering albedo and extinction coefficient as the input into the solar part of ECHAM6 radiation code (Kinne *et al.* 2006). The aerosol direct effect is estimated when the aerosol climatological data is used in ECHAM6 (i.e. without HAM-model).

- A ten member HAM-full ensemble is based on the observed monthly mean sea surface temperature but now using the aerosol module HAM2.1 coupled with the ECHAM6 (Kinne *et al.* 2006; Stevens *et al.* 2013), HAM2.1 predicts the evolution of the five different internally or externally mixed aerosol modes: sulfate, black carbon, particulate organize matter (POM), sea salt and mineral dust. Moreover, the computation of aerosol processes in HAM-full ensemble is based on the two moment scheme, used for the calculation of the cloud droplet and ice crystals (i.e. hydro-meteors). The HAM-model calculates the prognostic equations for the cloud droplet concentration and the ice crystal number concentration. It incorporates much more complex cloud micro-physical processes which in return have some influence on temperature, precipitation, cloud cover and most important on the aerosol concentration. The HAM-full scheme includes the direct and indirect effect of the aerosol forcing.

- A ten member HAM-dir ensemble is based on the observed monthly mean sea surface temperature using again the aerosol module HAM2.1 coupled with ECHAM6 but now taking into account the direct aerosol effect using one-way cloud droplet and ice crystal scheme.

This type of experimental setup allows by analysis of variance (ANOVA), the separation of the unpredictable internal climate variability from the potentially predictable aerosol and SST induced variability. In this study, the ensemble data will be analyzed using one-way and two-way ANOVA for the model variables of radiative energy balance (i.e. top, surface and atmosphere), aerosol optical depth (AOD), the hydrological cycle components like fresh water fluxes, temperature at 2m and 850 hPa levels and finally the velocity potential (VP) and stream function (SF) both at different pressure levels in the atmosphere to characterize the tropical dynamical changes.

Table 2.3: A brief description about the experiment design

Cases	Echam6 and Echam6-HAM control runs	Echam6 and Echam6-HAM ensemble runs	Comments
1.	Echam6 no-aerosol case (1995-2008)	Echam6 no-aerosol case (1995-2004) 10 ensemble members	For this case, control and ensemble run is without any aerosols concentration at all in the Echam6 radiation code.
2.	Echam6 aerosol case (1995-2008)	Echam6 aerosol case (1995-2004) 10 ensemble members	Aerosols optical properties data by Kinne et al. (2006) is used in the Echam6 radiation code both for control and ensemble runs.
3.	Echam6-HAM full effect (1995-2008)	Echam6-HAM full effect (1995-2004) 10 ensemble members	In this case, the AEROCOM data is utilized by the HAM-model. The model computed the aerosol microphysics interactively and the aerosol sources and sinks are present here.
4.	Echam6-HAM direct effect (1995-2008)	Echam6-HAM direct effect (1995-2004) 10 ensemble members	The same setup is used but this time the aerosol direct effect is estimated here.

2.4.1 A simple comparison between the ECHAM6 and ECHAM6-HAM AOD data

The AOD is an estimation of the extinction of solar radiation by atmospheric aerosol. The knowledge of the AOD is essential because it can affect the climate patterns by altering the radiation budget (Sarkar *et al.* 2005). The interactive aerosol scheme is used in ECHAM6-HAM and the ECHAM6 without HAM is integrated with the aerosol climatological data. The AOD of ECHAM6 and ECHAM6-HAM is shown in Figures 2.1 and 2.2. The model estimated a reasonable pattern of dust aerosol burden over the western Africa, the sea salt aerosol burden over the southern ocean and anthropogenic aerosol burden over the eastern China, as shown in Figure 2.1. The patterns of aerosol load became more pronounced when the AOD data is analyzed with the ECHAM6-HAM, it can be seen in Figure 2.2. The anthropogenic aerosol over north India is well captured by ECHAM6-HAM. The transformation of west African dust towards the Atlantic is also simulated in a good way by the ECHAM6-HAM. A plain difference between HAM interactive aerosol and Kinne aerosol climatology is plotted and shown in Figure 2.3. The maxima in this case are mainly captured for the west of Africa, Atlantic, south Asia and middle East regions.

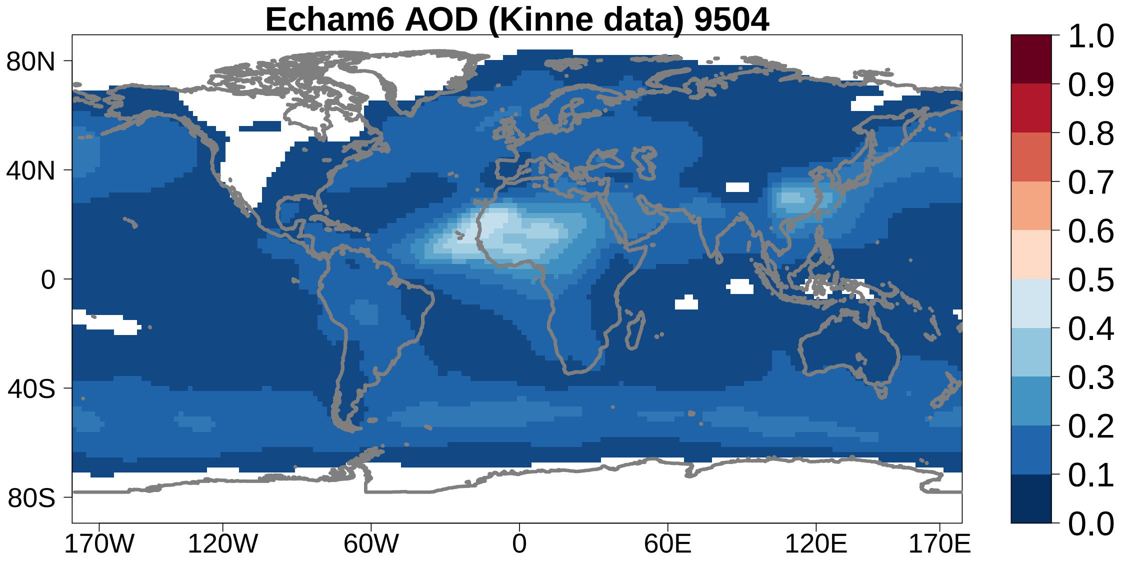

Figure 2.1: The AOD of ECHAM6 is shown here after taking the mean over the number of years and ensemble members. Aerosol direct effect is estimated using the climatological data of aerosol. The data values > 0.05 are plotted as an image over the map. The large values in color bar are associated with a good aerosol burden and vice versa. The data is analyzed between 1995 to 2004.

Zhao *et al.* 2011 studied the radiative effect of west African dust and its impact on the precipitation. The dust over the west Africa has a cooling effect for the surface and has a warming effect in the atmosphere. They also mentioned in their study that the dust aerosol burden changes the surface energy balance and the atmospheric diabatic heating which affects the atmospheric stability. The east China aerosol plume is associated with the heavy urban and industrial emission of aerosol particles, it is investigated by He *et al.* 2011 using the satellite data. Their study further associated the aerosol size distribution with the seasonal cycle. In summer, they found the dominance of fine mode aerosol in east China and during winter the

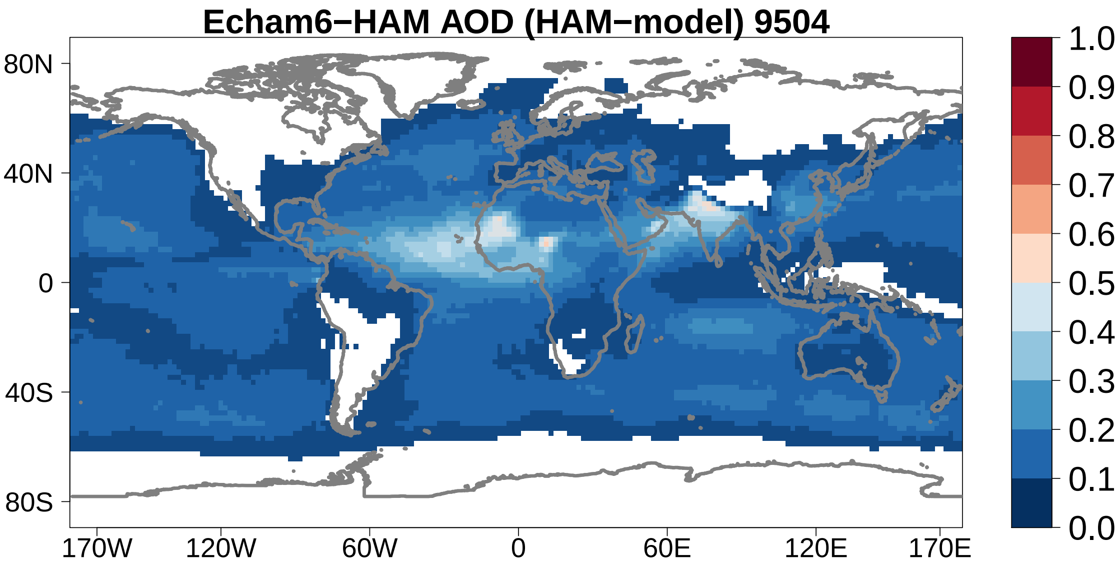

Figure 2.2: Same as Figure 2.1 but for direct aerosol effect estimated by the ECHAM6-HAM (HAM-dir).

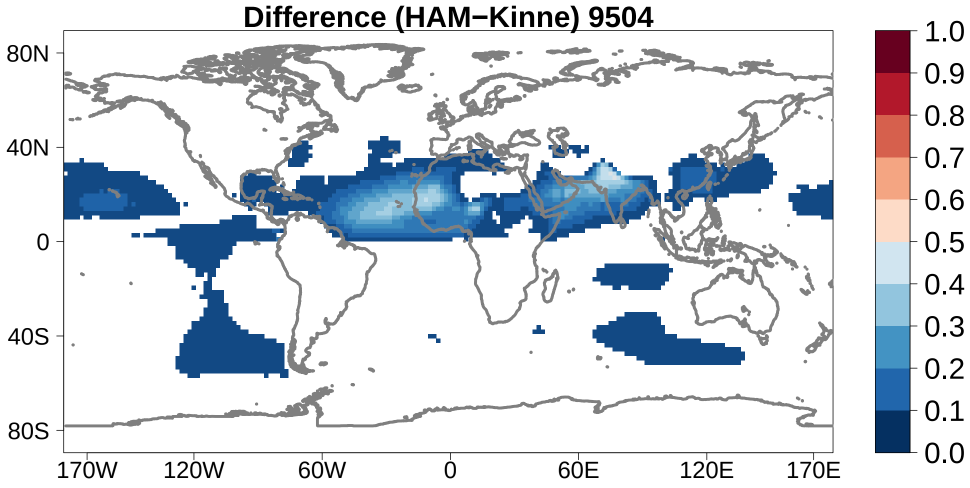

Figure 2.3: Plain difference between the HAM aerosol and Kinne aerosol climatology.

coarse mode aerosol has a dominant role over there. Sarkar *et al.* 2005 suggested that the anthropogenic aerosol and dust aerosol in the north of India play an important role for the aerosol burden.

3 Model validation

The main goal of this chapter is to estimate the global and zonal mean uncertainties of the radiative energy balance and the subsequent comparison between the model realizations and the observation data. The global means will be investigated for the planetary albedo (PA), radiative energy balance and the water balance. The zonal means will be estimated for the top of the atmosphere (TOA)-radiative energy balance (TREB), the surface radiative energy balance (SREB) and the atmospheric radiative energy balance (AREB). Two basic questions will be addressed:

- To which extent, the global mean radiative energy balance (REB) differs between the model realizations and observation?
- How the errors or uncertainties of REB are propagating from global to zonal mean scale?

The experiment setup has been discussed in the Section 2.4. The data for the REB and the water balance has been explained in Section 2.3.

3.1 What is the validation?

The word “valid” means able to generate the desired results or closer to the evidences and the “validation” means the confirmation of the validity of something. In climate sciences, the “validation” word is used to determine the fitness of the intended results. Normally, these results can be compared with observations, field data analysis and sometimes with the results of the other sophisticated models. The strengths and weaknesses of the climate model can be judged through it. In recent years, validation of the model data gained significant importance and it gives the detail overview about the findings of the intended results (Hollingsworth 1993).

The performance deficiencies of the different components of the model can be pointed out by the model validation. The output of ECHAM6-HAM will be evaluated for the global climate characteristics.

3.2 Global mean

The gridded model data is compared for the global mean of PA with the surface radiative budget (SRB) data, the global mean of REB with the SRB data and the global mean of the water balance with the GPCP and ERA-Interim data. For these cases, the uncertainties are estimated over the global scale.

3.2.1 Planetary albedo

The ratio between the reflected and incident shortwave at the TOA represents the PA. The meridional gradient of PA controls the dynamics of the atmosphere from the equator to poles.

It also changes the climate states and exhibits the changes in the meridional heat transport (Enderton, Marshall 2009). Therefore, PA profoundly influences the earth's climate. The changes in the PA are associated with the changes in the atmospheric and surface processes. This represents the important feedback phenomena of PA in response of the climate system to anthropogenic forcing. The climate sensitivity in the global climate model is linked directly with the changes in the PA feedback processes (Bender *et al.* 2006; Bony *et al.* 2006).

The PA mainly depends on the optical properties of clouds, aerosol and water vapor in the atmosphere and it also depends on the characteristics of the ice, ocean, vegetation and earth's surface. It has been found that most of the observed global average PA is influenced by the atmospheric reflection. The clouds and aerosol in the atmosphere can attenuate the surface contribution to the PA by a factor of 3 (Aaron, Battisti 2011). The changes of less than 0.02 units in global average PA could cause the global glaciation of the climate system (Budyko 1969). The PA could surely be affected when the snow and ice sheet of the planet earth is dramatically changed from "no snow cover" to the total glaciation. The cryosphere could melt when the PA will change from 0.30 to 0.20. In contrast to this, cryosphere could be frozen by changing the PA from 0.30 to 0.34 (Aaron, Battisti 2011). The surface reflection is accounted as 25 % of the climatological PA in the ice and the snow covered regions of the planet, the other 75 % of PA is assessed by the clouds and aerosol (Qu, Hall 2005).

There are few studies which are pointing towards the different values of the PA. For example, the satellite observations from Nimbus-7 computed the PA equal to 0.30 (Kiehl, Trenberth 1997). The global and annual mean of PA is estimated between 0.26 to 0.33 by Li *et al.* 1997. The PA is estimated 0.22 by Gorodetskaya *et al.* 2006. They used the satellite shortwave and sea ice cover data. They believe that the value of 0.22 can potentially change the sea ice cover. Rossow, Zhang 1995 indicated the global glaciation with PA value equal to 0.33. Aaron, Battisti 2011 found that the uncertainty range of global mean PA albedo is 0.016, they estimated this value by using different climate models of the coupled model inter-comparison project–3.

Figure 3.1 depicts the relative contribution of atmosphere and surface flux to the PA and its quantification by the model and observations. The 1-σ uncertainty limit for SRB is estimated as ± 0.02. The models no-aerosol and aerosol ensemble overestimate the PA. However, both of these cases are statistically significant because the difference between the SRB and model ensemble are within the uncertainty range of observations. On the other hand, the model HAM-full ensemble overestimates the PA which means that the incoming SW radiations are reflected back to space and cooled the earth's surface. The HAM-dir ensemble underestimates the PA. In this case, the incoming SW radiation is absorbed by the earth's surface compared to observations, resulting in a warming of the planet. The variation among the model realizations compared to observations is due to the current experiment setup. As described earlier that the ECHAM6-HAM is not coupled to the ocean model but it is integrated with the prescribed SST data. Due to this, the imbalances in HAM-model ensemble are more pronounced compared to the ECHAM6 ensemble. Other reason might belong to the tuning of the model code for the cloud micro-physics processes. Model code is tuned for three ensemble named as no-aerosol, aerosol and HAM-full. The data in case of HAM-dir is simulated with a non-tuned code. Mauritsen *et al.* 2012 explained that climate models poorly formulate the clouds and convective processes. They also described that the adjustment or tuning of the cloud parameters in the global models helps to improve the representation of the earth's energy budget.

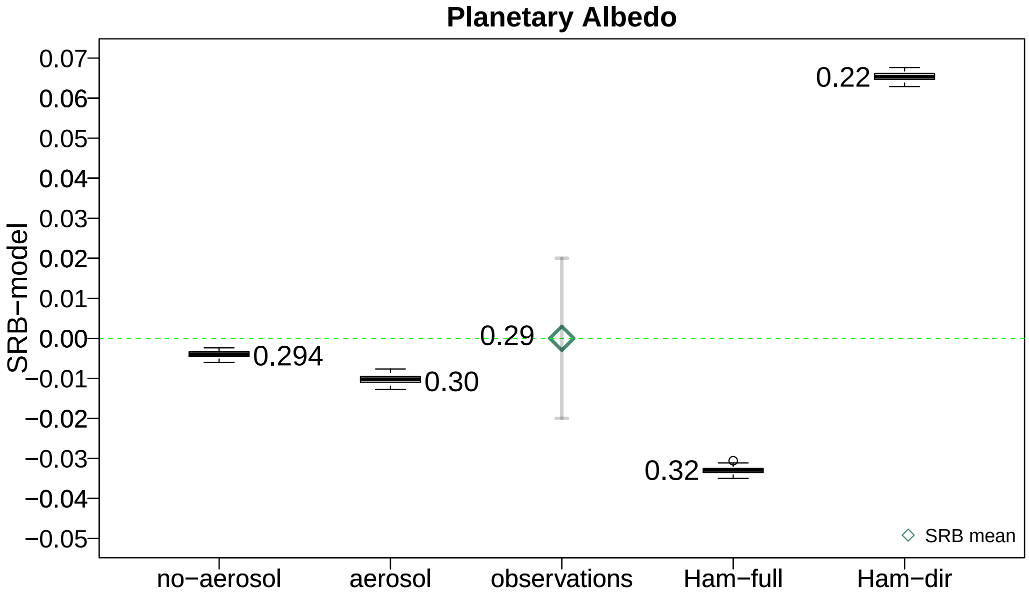

Figure 3.1: The difference between the global mean PA of SRB and model realizations. The text values near the box plots represents the overall mean of PA. The green dotted line highlights the no difference between the model data and observations. The SRB uncertainty limit represents the 1-σ standard deviation over ten years. The variability in the box plots depend on temporal scale (i.e. 10 years and 10 ensemble members) and the PA data is averaged over the spatial scale (i.e. longitude and latitude). The uncertainty limit of observations is considered as a reference range against which the model values are validated. In case the boxes fall onto the green line or within the uncertainty limit of observations then it means that model realization agrees with the satellite data. The x-axis has four different model ensemble like no-aerosol, aerosol, HAM-full and HAM-dir and one observation. The uncertainty range of satellite data is plotted over the mean value of the SRB (i.e. aqua marine diamond) and it varies along the y-axis. The data is analyzed between 1995-2004.

3.2.2 Radiative energy balance

The TREB is the difference between the incoming solar radiation and outgoing solar and thermal radiation at the top of atmosphere (TOA). The SREB is obtained by the difference of solar energy balance and thermal energy balance at the surface. The AREB is the residual between the TOA and surface radiative balances. Mathematically, these three quantities are expressed by the Equations 3.1, 3.2 and 3.2, respectively. The downwards arrow (↓) is for the incoming shortwave (SW) and longwave (LW) radiation. The upwards arrow (↑) represents the outgoing SW and LW radiation.

$$TREB = (\, SW_{TOA} \downarrow \,) - (\, SW_{TOA} \uparrow \text{ - } LW_{TOA} \uparrow \,) \tag{3.1}$$

$$SREB = (\, SW_{surf} \downarrow \text{ - } SW_{surf} \uparrow \,) - (\, LW_{surf} \downarrow \text{ - } LW_{surf} \uparrow \,) \tag{3.2}$$

$$AREB = (TREB - SREB) \tag{3.3}$$

3.2.2.1 TOA radiative energy balance

For the TREB, the part of the incident SW that is reflected back to the space by clouds and aerosol represent the outgoing SW radiation at the TOA. The portion of surface LW radiation which is transmitted through clouds and atmosphere into the space corresponds to the emitted LW radiation at the TOA. For the radiative equilibrium at the TOA, the emitted LW radiation balances the net inflow of SW radiation (see Equation 3.1). The LW radiation which reaches the TOA is affected by gases and aerosol in the atmosphere. The small fraction of the LW which escapes to space comes directly from the surface. The atmosphere acts for it as a "blanket". At TOA, the LW radiative forcing is represented as the difference between the TOA LW flux with and without absorption of the atmospheric gases (Kiehl, Trenberth 1997). The satellite instruments quite efficiently estimate the TOA incoming solar radiation and the reflected solar radiation but it is not easy for these instruments to measure the longwave or thermal radiation. For this purpose, the radiosondes and LiDAR instruments are used for the assessment of the LW radiation (Rossow, Zhang 1995). Stephens *et al.* 2012 estimated the uncertainty limit for the net TREB as ±4 W·m^{-2}. They used the cloud and earth's radiant energy system (CERES) satellite data and associated this uncertainty limit with the instruments calibration errors.

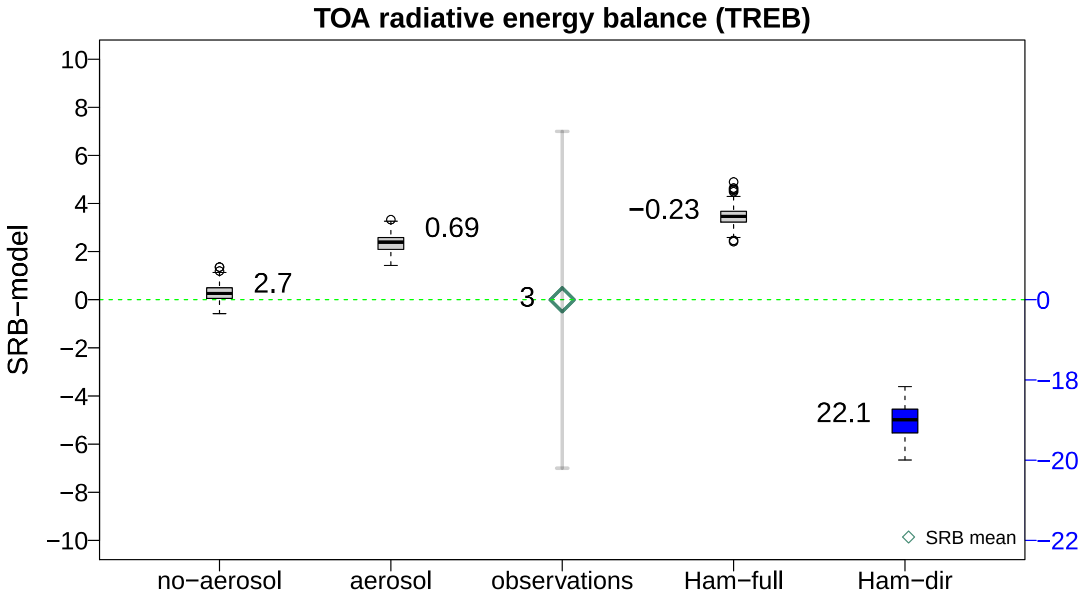

Figure 3.2: Same as in Figure 3.1 but for the TOA radiative energy balance (TREB). The difference between the model ensemble and observation is plotted in W·m^{-2}. The range of difference for the blue box plot is shown on the right side of y-axis.

Upon comparing the values of the different model realizations used in this study with the SRB satellite data, a good agreement is observed between the model ensemble and observations, as shown in Figure 3.2. Approximately 2 W·m^{-2} variability in TREB is recorded due ten ensemble members. For the satellite TREB data, the estimated standard deviation is ±7 W·m^{-2}. Three out of four model realizations are within the observational error range, only the HAM-dir case overestimates the TREB. In this case, the system receives more energy compared to the other three cases. This large discrepancy for HAM-dir case has already been detected for the PA in Figure 3.1.

In another study, the satellite Nimbus-7 and the models estimated an imbalance of 3 W·m^{-2} for the radiative energy balance at the TOA. They associated the lack of proportion with a net radiative heating of the planet (Ardanuy *et al.* 1992; Yu *et al.* 1999). Fasullo, Trenberth 2008 showed a much larger imbalance of 7 W·m^{-2} at the TOA using the CERES satellite data and they linked this increase in radiative energy balance with the increase in concentration of carbon dioxide and other greenhouse gases in the atmosphere. The results of global mean TOA radiative energy balance in this study are in agreement with the results of Wild, Roeckner 2006, except the HAM-dir case.

3.2.2.2 Surface radiative energy balance

As stated earlier in Equation 3.2 that the balance of the incident and scattered SW radiation at the surface is equal to the balance of reflected (i.e. incoming) and emitted LW radiation. The incident SW radiation is the portion of incoming solar radiation that reaches directly to earth's surface without any modification in the lower troposphere and the reflected SW radiation arrives after some changes by the atmospheric processes. The LW incoming radiation is the part of radiation which is emitted from the earth's surface and it is trapped in the earth's atmosphere by the greenhouse gases and reflected back to the earth's surface. This phenomena is known as the greenhouse effect of the atmosphere. The emitted LW radiation represents the loss of the energy from the earth's surface (Kiehl, Trenberth 1997; Wild *et al.* 2013).

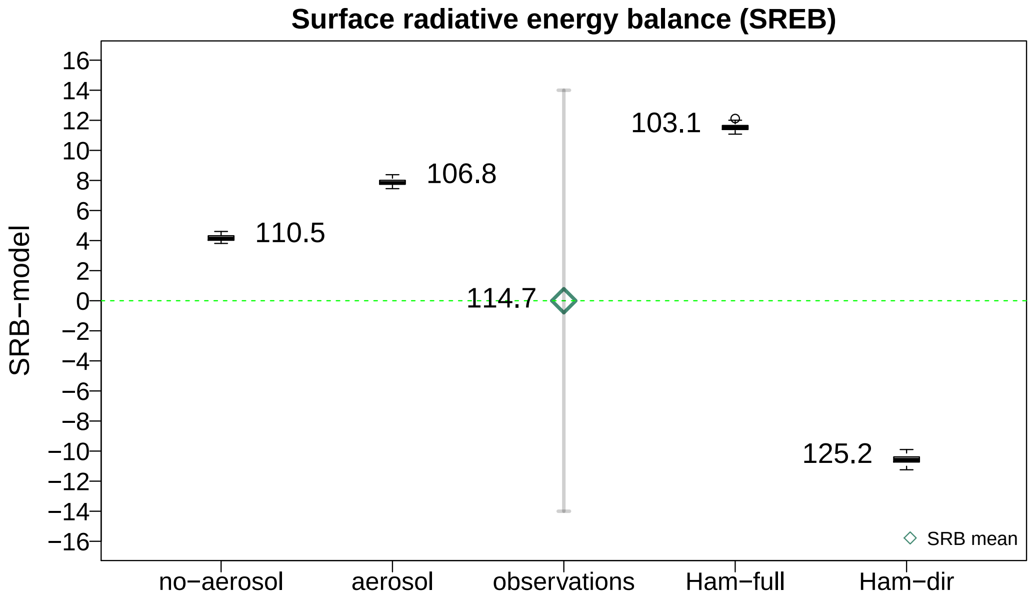

Figure 3.3: Same as in Figure 3.1 but for the surface radiative energy balance (SREB).

Unlike the TREB flux, the SREB flux is estimated mainly for the land areas and cannot be directly computed from the satellites instruments. Most of the uncertainties are originated due to the poor data coverage over the ocean by the ground based instruments (Trenberth *et al.*

2009). The SREB flux can only be calculated from the TREB flux by using the empirical and physical climate models. These models also assessed the atmospheric variability and emission processes and introduces additional uncertainties. A few studies estimated larger uncertainties in SREB than TREB (Stephens *et al.* 2012; Wild *et al.* 2013).

Zhang *et al.* 2004 used the earth radiation budget experiment data and they estimated the uncertainty limit for surface energy balance between ±10 to ±15 W·m^{-2} and associated these errors with the change in near surface temperature. Stephens *et al.* 2012 computed the net surface energy balance and their estimated uncertainty value is ±17 W·m^{-2}. The model used in their study underestimated the low level clouds and absorbing aerosol in the atmosphere. Li *et al.* 1997 assessed the regional net surface flux uncertainty as ±20 W·m^{-2} and reported the large errors due to the inadequate discrepancies in the spectral and angular correction of the satellite radiance.

The standard deviation for the SREB is ±14 W·m^{-2}, as shown in Figure 3.3. Large biases up to ±10 W·m^{-2} are detected for the HAM-model ensemble. However, all of the model ensemble are within the uncertainty range. Three model cases underestimated the SREB which means less energy is radiated in these cases from earth's surface to the atmosphere. However, the HAM-dir overestimated the SREB, because it receives more energy in TREB case, so it has to radiate more energy in SREB case. Wild *et al.* 2013 assessed the value of 106 W·m^{-2} for the global mean net surface flux which is closer to the aerosol case of this study.

3.2.2.3 Atmospheric radiative energy balance

The atmospheric fluxes are obtained as the residual of the TOA radiative energy balance and surface radiative energy balance. The standard deviation for the AREB is estimated as ±10 W·m^{-2}m, it can be seen in Figure 3.4. The AREB data has some biases while assessing the HAM-model ensemble and these biases might come from Equation 3.2. The model realizations overestimate the AREB but they are within the uncertainty range of the observations in particular for the no-aerosol and aerosol ensemble. The overall mean values shows the less loss of radiative energy for HAM-model cases. For the HAM-dir ensemble, the atmosphere absorbs more energy compared to other cases.

The atmospheric processes are driven by the AREB. In the atmosphere, the radiative energy is balanced by the convective sensible fluxes and latent energy fluxes. The smaller AREB in absolute values therefore requires the smaller convective fluxes and this will imply a higher stability in the atmosphere. Even a non-tuned HAM-dir ensemble of this study exhibited a stable atmosphere. However, the best estimate of radiative fluxes are possible with the tuned model code. Wild *et al.* 2013 assessed the global mean AREB as -105 W·m^{-2} and it is quite similar to AREB aerosol, AREB HAM-full and AREB HAM-dir cases of this work. The major part of this energy surplus at the surface or the deficit in the atmosphere depends on the hydrological cycle.

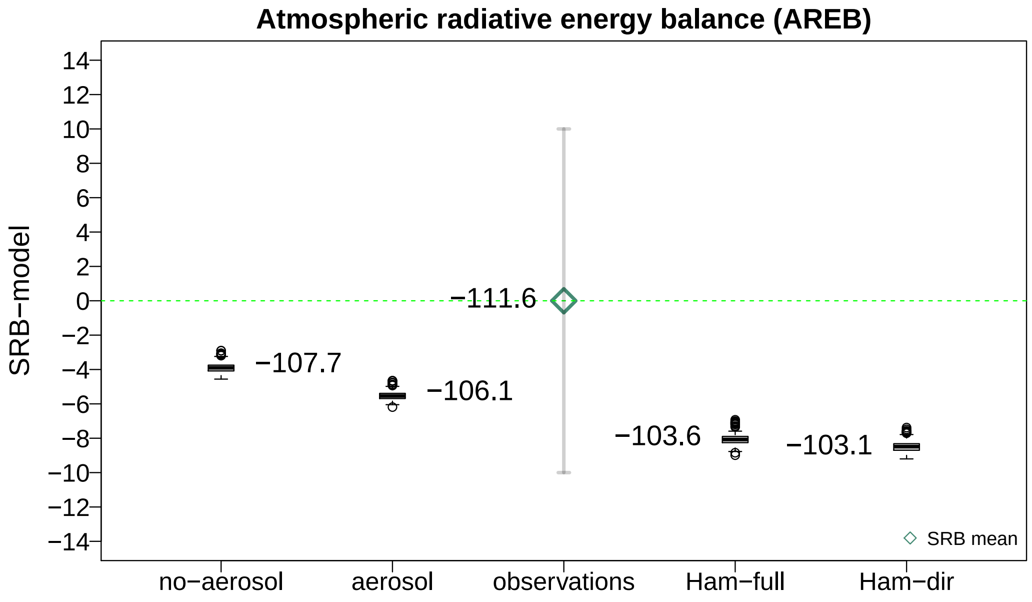

Figure 3.4: Same as in Figure 3.1 but for the atmospheric radiative energy balance (AREB).

3.2.3 Water balance

The global and annual mean water cycle will be analyzed in response of TREB and SREB flux. The TREB of HAM-dir ensemble showed an imbalance of order -19.2 W·m^{-2} compared to observations and the SREB of HAM-dir ensemble assessed a discrepancy of order -10.6 W·m^{-2}. These inconsistencies in the radiative energy balance further turned this research towards the analysis of the water balance.

Solar heating plays an important role in the evaporation of the water from the ocean and land surface. The evaporated water is transported by the winds and form the clouds and precipitation falls over land and oceans. The excessive precipitation joins streams and rivers and through it the oceans get fresh water (Trenberth *et al.* 2007a). Thus water plays an important role in earth's climate. The global water or hydrological balance is recognized as the ratio between the water inflow and outflow over the spatial and temporal scales. The water balance determines specific climate features from the land use, water management and landscape of any territory. The water circulation in the atmosphere-hydrosphere-lithosphere can be influenced by the natural factors and the human activities. Precipitation, evaporation and fresh water are considered as the basic quantities in determining the water balance. Besides the basic quantities, the water loss or the water gain can also be observed through the smaller water bodies. For example, water processes in the atmosphere and surface can lead to such losses or gains. However, these minor processes did not play a significant role when one considered them over the global scale. Fresh water is mainly used for the different human needs and it is taken as an important factor for the life on earth. Some of the fresh water is returned in the atmosphere due to the evaporation (i.e. water loss) from the surface and sub-surface runoff (e.g. irrigation lands and water reservoirs). For the appropriate water balance calculation, this must be taken into account (Shiklomanov 1993).

In the atmosphere, the water vapor acts as a greenhouse gas and is responsible for the strong feedback in the climate system (Kiehl, Trenberth 1997). Fasullo, Sun 2001 found that an increase of 4 % of water vapor feedback will increase the radiative effect by about 1.5 $W{\cdot}m^{-2}$ (Trenberth *et al.* 2007a). Kim, Ramanathan 2008 determined that the increase in water vapors in the atmosphere will increase the absorption in the atmosphere to few $W{\cdot}m^{-2}$.

In principle, the global precipitation is equal to the global evaporation. The errors in the precipitation data can occur due to the wind effects, data sampling and gauges. The GPCP data is reliable for the precipitation estimation. It is blend of the satellite and gauge data (Adam *et al.* 2006; Adler *et al.* 2003). The standard deviation of total precipitation is estimated as ± 0.64 and the global mean value of GPCP is 2.68 mm/day, as shown in Figure 3.5. The value of the total precipitation over land and ocean is 2.69 mm/day (Adler *et al.* 2012). The model realizations do have a good agreement with the GPCP, however all model realizations slightly overestimated the total precipitation.

For the Evaporation, the different ensemble of the model do agree with ERA-Interim data, as shown in Figure 3.6. The standard deviation for the evaporation is ± 1.25. All the model values are within the uncertainty range of observations. Fujihara *et al.* 2014 estimated the root mean square error and relative error for different observations products like GPCP and ERA-Interim. They recommended others to use the GPCP total precipitation and ERA-Interim evaporation for the analysis of the water balance.

The fresh water flux is the difference between the total precipitation and evaporation. The standard deviation of the fresh water is ± 1.89, it can be seen in Figure 3.7. In general, the model realizations agree with observations but they slightly overestimate the fresh water. The global mean of fresh water is approximately zero. It means the imbalances in TREB and SREB of HAM-dir ensemble is not due to the latent heat fluxes but it is due to the sensible heat fluxes (e.g. depends on the temperature change).

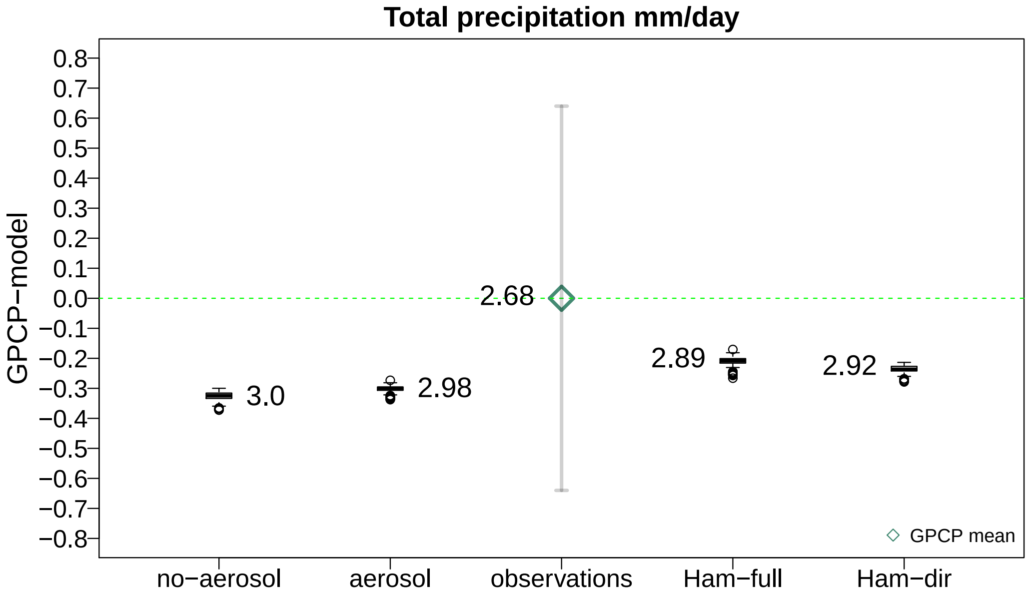

Figure 3.5: Same as in Figure 3.1 but for the total precipitation. The difference between the global mean is plotted in mm/day.

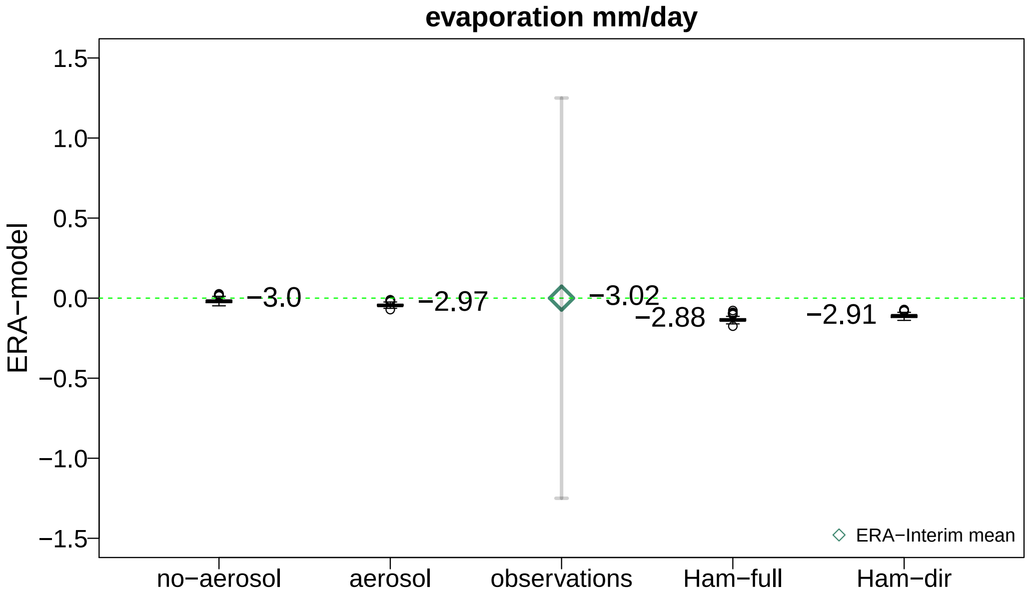

Figure 3.6: Same as in Figure 3.1 but for the evaporation.

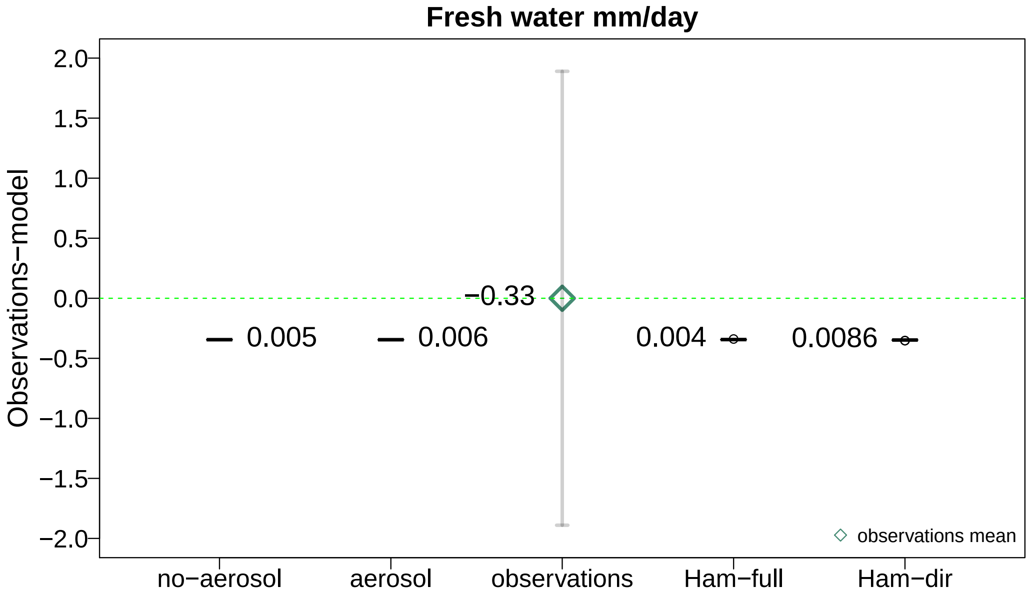

Figure 3.7: Same as in Figure 3.1 but for the fresh water.

3.3 Zonal mean

The global uncertainties have already been assessed for the radiative energy balance. It will be interesting to further investigate how these uncertainties are generated over the meridional scale. The zonal mean of the radiative energy balance will give the information about the radiation patterns from the equator and poles. The uncertainties and differences between the zonal mean of model realizations and observations is also plotted in this section.

3.3.1 TOA radiative energy balance

The Figure 3.8 shows the simulated ECHAM6-HAM and satellite observations SRB zonal mean profiles of TREB over 10-years. Using the left side of y-axis, it can be seen that all model realizations do agree with observations, except the HAM-dir ensemble. Other three model simulations are within the grey band which means the model data is significant especially between 30S to 30N. For the TOA, It is observed that the equator and tropics receive more SW radiation compared to the poles, as expected.

The difference on the right side of y-axis tells about the deviation of the model realizations with respect to observations. The model overestimates TREB when the difference value is positive, it underestimates when it is negative. Model and observations are in good agreement when the difference between them is near to zero. The radiative fluxes are less reliable in the polar regions due to scene identification problems in the area of snow or ice. The imbalance in HAM-dir ensemble is already observed in the global mean case and it is also projected in the zonal mean case. The other model realizations show a good agreement, with an exception over the polar regions. A surplus of energy can be seen for HAM-dir ensemble.

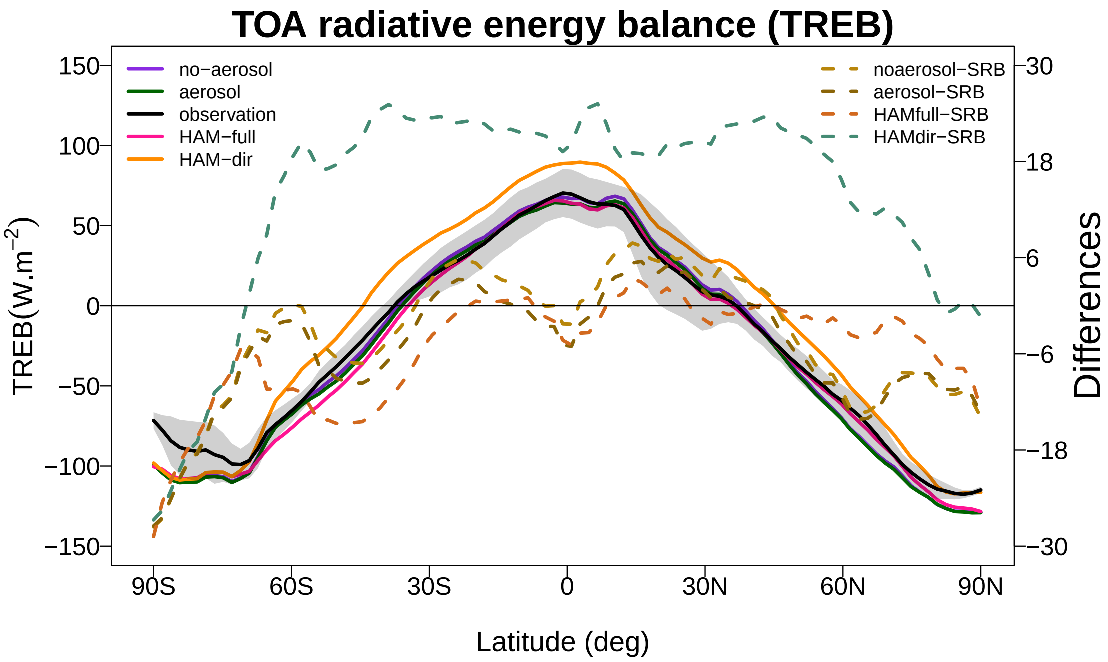

Figure 3.8: The solid lines in the left side legend represent the absolute values of the zonal mean TOA radiative energy balance (TREB) for the model realizations and observations. The unit of the data values is W·m^{-2}. The absolute values are estimated by taking the mean over all dimensions of the data, except the latitude. The differences between model and observations are plotted as in dashed lines. The values of the model realizations for the difference plot are described by the right side legend. The grey band over the model realizations and observations is representing the inter-annual variability of the TREB. This grey band is actually the standard deviation of satellite data. The absolute values of the zonal mean model realizations are significant when they fall within this grey band. The data is analyzed between 1995 and 2004.

3.3.2 Surface radiative energy balance

The zonal mean profiles of SREB for ECHAM6-HAM and satellite data is shown in Figure 3.9. The absolute values of the model realizations do agree with the observations especially over tropics. The equator and tropics radiate more energy than the polar regions. From 35° to 90° latitude, these regions indicated towards a deficit of energy. The HAM-dir ensemble overestimates the SREB compared to the other three ensemble which has already been observed in global mean case. Other model realizations do agree with observations, however they slightly underestimate the SREB, similar they did for the global mean of SREB.

The difference plot on the right side of y-axis also verifies that the HAM-dir ensemble overestimates the SREB as compared to the other realizations. The radiation flux near the north of equator are mostly overestimated between 5 °N and 10 °N. The pattern between these latitudes in SREB case might be related to the anthropogenic emission of the biomass burning (Williams *et al.* 2010).

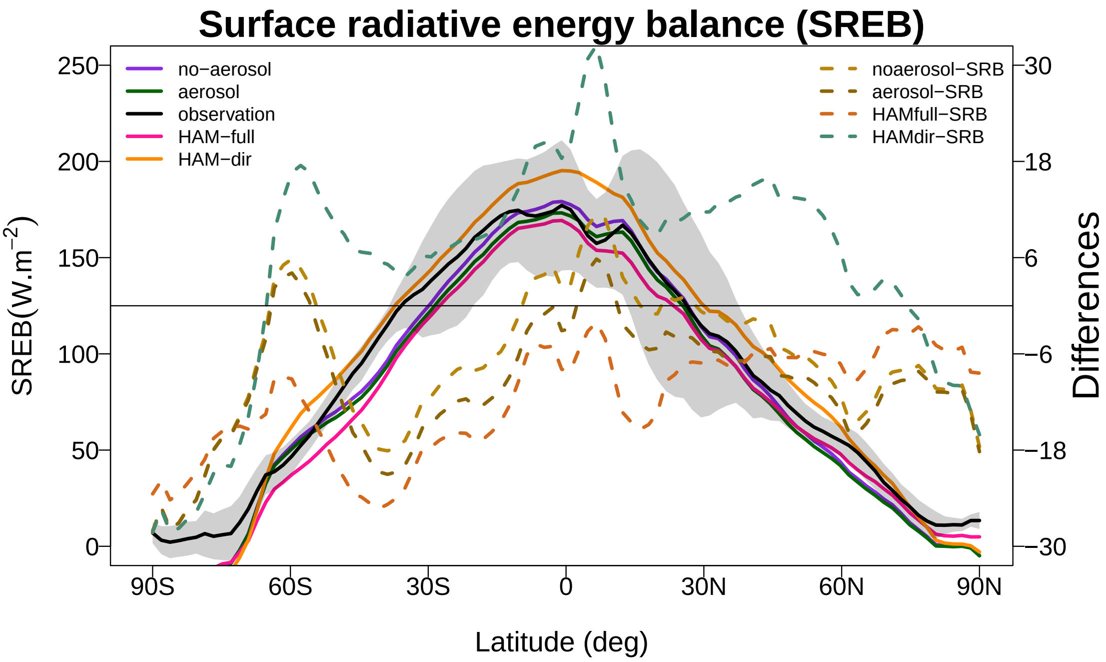

Figure 3.9: Same as in Figure 3.8 but for the SREB case.

3.3.3 Atmospheric radiative energy balance

The net gain in energy or the absorption due to the different aerosol ensemble for the zonal mean AREB case is shown in Figure 3.10. By following the solid lines and grey band, the model realizations has a good agreement with observations, because most of the values are residing under the grey band. However, the model realizations show some deviation from the observations between 20S to 50S latitude. All ensemble here show a strong absorption compared to SRB and the model data over these latitude is overestimating the AREB. The difference plot also indicates that model values are exaggerating the AREB between 20S to 50S.

The global and zonal mean radiative energy balance and water balance uncertainties have been estimated in this chapter. Overall the model realizations and observations show a good agreement with each other. However, the HAM-dir case is considered as sensitive in assessing the TREB and SREB. Particularly in this case, the model code is not tuned for the cloud microphysics and thus it is estimating a different climatic scenario for the radiative energy balance. However, almost all model realizations have agreed with the observation for the AREB case. It is a recommendation for others, do not use the non-tuned model code. Stevens *et al.* 2013 pointed towards the marine boundary layer cloud biases in ECHAM6 model. Due to this, more shortwave radiation is absorbed by the reflecting aerosol and thus leads to a bright surface in the tropical regions. They suggested that these biases of tropical cloudiness can be reduced when the model is integrated with the high spectral resolution compared to the low resolution.

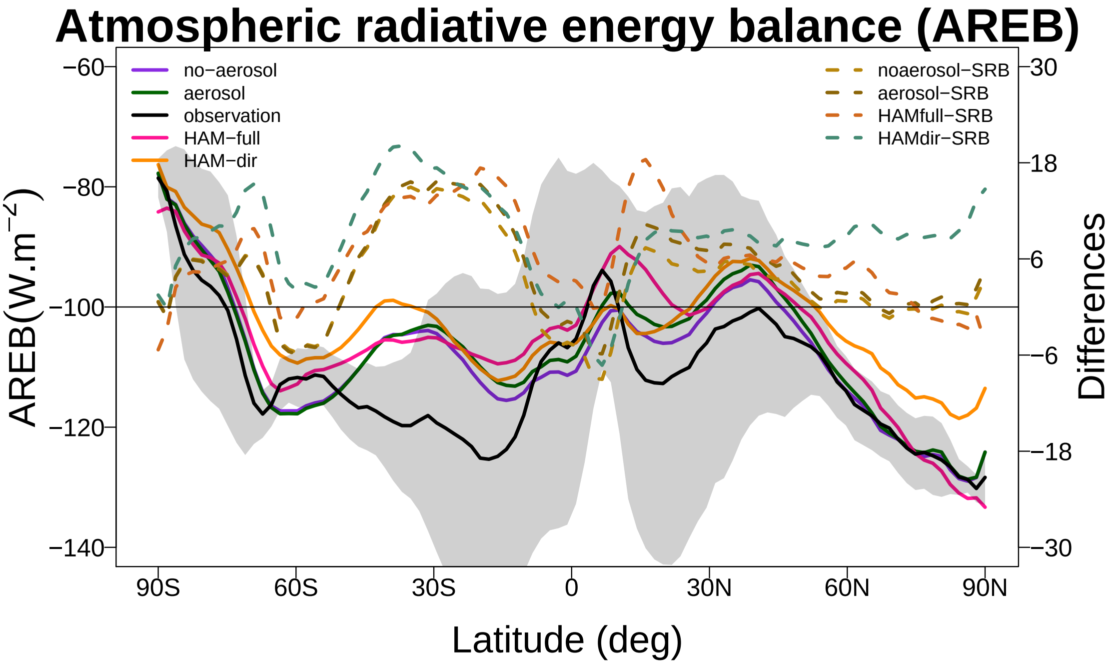

Figure 3.10: Same as in Figure 3.8 but for the AREB case.

4 Statistical methodologies

This chapter introduces statistical methods such as ensemble generation, ensemble techniques, analysis of variance (ANOVA) and correlation coefficients. The following questions are addressed in this chapter:

- Why is it important to create the ensemble?
- How do the ensemble techniques work and which ensemble method is used in this study?
- What is the ANOVA model? Why is it important to do the data analysis with one-way and two-way ANOVA?
- What is the linear regression model and how are the correlation coefficients are estimated by this model?

4.1 Ensemble generation

The first numerical weather prediction model (NWP) was started working in 1950, but the original code of NWP was developed in early 20th century by Richardson 1922. It was based on quasi-geostrophic assumptions and predicted the atmospheric flow patterns for the next few days. In recent years, the global and regional climate models and the NWPs are becoming a powerful tool for climate and weather forecasts. These models calculate the physics and dynamics in precise way than the classical models. However, the parametrization techniques used in these models are often based on empirical knowledge rather than the physical equations. The data from the satellite instruments is inherently incorporated in the model using complex data assimilation techniques. The distribution of this data on the model grid resolution is quite sparse especially over the ocean. Therefore, the model output data contains the ingrained deficiencies in its description of the atmospheric processes (Hense 2005; Leutbecher, Palmer 2008). This contributes to the forecast error by the model (Lorenz 1982). One has to understand that neither the model nor the analysis of the initial atmospheric state is ideal.

Lorenz 1963 found that some small errors in the model initial state exponentially can evolve the uncertainties which affects the model data not only for the local scale but with the passage of time, it also affects the regional and global scale. This phenomenon is known as the butterfly effect. The most appropriate way to predict model errors is to generate a set of ensemble members. The generation of the model ensemble can be computationally expensive because it requires a huge amount of computational time and a large number of data samples. The ensemble can be based on the single NWP model forecasts with different initial conditions and different parameter settings or they can be based on the forecasts of different NWP models, known as multi-model ensemble. The ensemble forecasts performed by a single model is used in all global ensemble prediction system including climate prediction, where the unperturbed forecast is normally known as 'control run' and the perturbed forecast as an 'ensemble run' (Keller 2008).

The ensemble prediction system has great benefit compared to the model control run (Hagedorn *et al.* 2005). The decadal prediction requires the sampling strategies for the spread of possible outcomes to be consistent with the initial condition uncertainties. On the global scale, both internal variability and the external forcing (e.g. greenhouse gases concentration) are important sources of the potential predictability. However, on the regional scale the significance of the external forcing is largest over the tropical oceans and the contribution of the internal variability is larger over the middle and high latitude ocean regions.

For this study, it is worthful to predict the aerosol and SST variability on the decadal time scale. Pohlmann *et al.* 2009 concluded that in general the role of uncertainties due to the anthropogenic emission of the aerosol is likely to be smaller when projected over a decade or two ahead. However, there are some exceptions in the regions where the uncertainties in forcing results from the spatially heterogeneous tropospheric aerosol (Schulz *et al.* 2006). Moreover, the role of the natural forcing such as solar variability and volcanic eruption cannot be predicted in a real forecasting system (Meehl *et al.* 2009).

4.2 Ensemble techniques

Normally, the perturbation of the model initial state requires a huge computational power because of the large numbers of degrees of freedom (df) generated by the model run. The large df also leads to a large number of random uncertainties and results in forecasting errors (Leith 1974). These errors or uncertainties can be reduced by the implementation of three methods known as the singular vectors, bred vectors and perturbed observations. An overview about the different ensemble techniques is presented in this Section. The singular vector method was designed by the ECMWF. This method is computationally very expensive because it creates the number of perturbation for the weather forecasts or the maximum perturbation growth rate for a finite time range (Buizza, Palmer 1995). The bred vector method was developed at the National Centers for Environmental Prediction in 1992. It is computationally not expensive and mainly based on the perturbation of the initial conditions. The breeding perturbation used previous ensemble and obtained the growing component of the errors or uncertainties (Keller 2008). The observation perturbation technique was developed at the Meteorological service of Canada. In this method, the ensemble data is produced by perturbing the observations used for the further analysis (Houtekamer, Derome 1995; Houtekamer, Mitchell 1998). All these illustrated techniques are related to weather forecasting methods.

In contrast to the above described methods, the ensemble members for this study are generated with almost independent initial conditions. The ensemble technique used here is quite simple and different from the weather forecasting techniques. It considers the model control runs and re-sampled the initial conditions every year and then proceeded under a common forcing, in this case SST and the aerosol forcing.

4.3 Analysis of variances (ANOVA)

Statistical methods like linear regression model, ANOVA and correlation coefficients are the part of general linear models family. The techniques of general linear model fits well to the experiment setups designed by the psychologist, sociologist, climate scientist and agricultural scientists. It is a simplest and flexible data analysis method.

The climate models are built for the mathematical representations of the climate. Therefore, a careful method is needed to determine whether a model has achieved the expected goals in determining the climate variability or not. ANOVA is a classical technique and It was generally developed for the agricultural experiments (Chapman *et al.* 1994; Gough, Welch 1994). The parametrization of the various sub-grid scale processes can be easily evaluated by applying the ANOVA technique. It explains that which sources contribute significantly to the variation of the data obtained from the experiments. Generally, a distinction is made between one-way ANOVA and two-way ANOVA with interaction.

ANOVA is based on the dependent and independent variables. It finds the way how the variance of the dependent variable is depending upon the one or more independent variables. The variance of a numerical variable represents the dependent variable. The different conditions of the experiments setup is linked to the one or more categorical variable and it recognized the independent variable. Four experiment setups (e.g. no-aerosol, aerosol, HAM-full and HAM-dir) differ in the description of the aerosol scheme. Thus, the aerosol variability should expect to contribute a reasonable part in the model output. Instead of the ocean model, the ECHAM6 is integrated with the prescribed SST data. therefore, it is expected that the SST variability will play a dominant role in the model output data. The remaining variability after the aerosol and SST forcing will belong to the internal climatic noise.

4.3.1 One-way ANOVA

The one-way ANOVA model is used to assess the variance of SST and the climatic noise and to test the null hypothesis $H_{(null)}$. The SST variability for the decadal climate will be projected through this way. One-way ANOVA is implemented on the AOD data of HAM-full ensemble. The dependent variable in this case is AOD and SST induced variability (SIV) is the independent variable.

$$H_{1ij} = \mu_1 + R_{1i} + \varepsilon_{1ij} \tag{4.4a}$$

$$\overline{\mu_1} = \overline{H_{100}} \tag{4.4b}$$

$$\overline{R_{1i}} = \overline{H_{1i0}} - \overline{\mu_1} \tag{4.4c}$$

$$\varepsilon_{1ij} = H_{1ij} - \overline{\mu_1} - \overline{R_{1i}} \tag{4.4d}$$

$$\varepsilon_{1ij} = H_{1ij} - \overline{H_{1i0}} \tag{4.4e}$$

One-way ANOVA model is explained by Equation 4.4a. The explanation of different constituents used in this model is described by the remaining equations. In this setup, the H_{1ij} denotes the dependent variable and $\overline{R_{1i}}$ is a independent variable. The average over time and ensemble members is represented by $\overline{\mu_1}$. The internal climatic noise is denoted by ε_{1ij}. The subscripts i and j in Equation 4.4 represent the variation of AOD data over 10-years and 10-ensemble members (i.e. i= 1,2,....,10 and j= 1,2,....,10). The SST variability $\overline{R_{1i}}$ is the difference between the $\overline{H_{1i0}}$ and the overall mean $\overline{\mu_1}$. The term $\overline{H_{1i0}}$ is estimated when the AOD data is averaged over the ensemble members. The $\overline{R_{1i}}$ do not show any variability when the difference between the $\overline{H_{1i0}}$ and $\overline{\mu_1}$ is closer to zero. A reasonable difference among the ensemble members gives the best estimate of $\overline{H_{1i0}}$ and therefore it computes the larger $\overline{R_{1i}}$ values instead of the ε_{1ij} data values. The internal climatic noise ε_{1ij} of the data is associated with a term that whatever is leftover after the average value $\overline{\mu_1}$ and SST effect $\overline{R_{1i}}$. This makes sense because the experiment design contains the effect of $\overline{\mu_1}$ and $\overline{R_{1i}}$.

$$SS_{H_{1ij}} = SS_{R_{1i}} + SS_{\varepsilon_{1ij}} \tag{4.5a}$$

$$SS_{R_{1i}} = j\sum_{i=1}^{10}(\overline{H_{1i0}} - \overline{\mu_1})^2 \tag{4.5b}$$

$$SS_{\varepsilon_{1ij}} = \sum_{i=1}^{10}\sum_{j=1}^{10}(H_{1ij} - \overline{H_{1i0}})^2 \tag{4.5c}$$

$$SS_{H_{1ij}} = \sum_{i=1}^{10}\sum_{j=1}^{10}(H_{1ij} - \overline{\mu_1})^2 \tag{4.5d}$$

Table 4.1: ANOVA degrees of freedom description

Sources	Sum of squares	df
SST effect	$SS_{R_{1i}}$	(i-1)
Climate noise	$SS_{\varepsilon_{1ij}}$	i(j-1)
Total variability	$SS_{H_{1ij}}$	ij-1

The sum of squares of $SS_{R_{1i}}$ and $SS_{\varepsilon_{1ij}}$ data values is further investigated by using the ANOVA model of Equation 4.4. All the values of $SS_{R_{1i}}$ and $SS_{\varepsilon_{1ij}}$ in Equation 4.5 are added to obtain the $SS_{H_{1ij}}$. The values of $SS_{R_{1i}}$ and $SS_{\varepsilon_{1ij}}$ cannot be compared directly, because these values have been taken from the different independently estimated parameters, for this case, the number of years and the ensemble members.

In Table 4.1, the sum of the squares of the SST effect (i.e. $SS_{R_{1i}}$) is taken over the i deviations (i.e. time) that sum to zero, therefore, it has (i-1) degrees of freedom (df). The climate noise term (i.e. $SS_{\varepsilon_{1ij}}$) is taken over the deviations that are subject to the i constraints and the deviations within j (i.e. ensemble members) are sum to zero, eventually it has i(j-1) df. The total sum of squares has only one constraints i.e. ij and consequently it has ij-1 df.

$$MS_{R_{1i}} = \frac{SS_{R_{1i}}}{(i-1)} \tag{4.6a}$$

$$MS_{\varepsilon_{1ij}} = \frac{SS_{\varepsilon_{1ij}}}{i(j-1)} \tag{4.6b}$$

$$MS_{H_{1ij}} = MS_{R_{1i}} + MS_{\varepsilon_{1ij}} \tag{4.6c}$$

The average value of sum of squares gives the mean square values in Equation 4.6. It is obtained by dividing the $SS_{R_{1i}}$ and $SS_{\varepsilon_{1ij}}$ with the df. The df is associated with the number of independent values of these quantities. The mean square values are examined for making a comparison between the variance of SST and climatic noise.

$$F_{ratio.R_{1i}} = \frac{MS_{R_{1i}}}{MS_{\varepsilon_{1ij}}} \tag{4.7}$$

$$R^2_{value.R_{1i}} = \frac{MS_{R_{1i}}}{MS_{H_{1ij}}} \tag{4.8a}$$

$$R^2_{value.\varepsilon_{1ij}} = \frac{\varepsilon_{1ij}}{MS_{H_{1ij}}} \tag{4.8b}$$

Finally, the F_{ratio} and the R^2_{value} are computed in Equations 4.7 and 4.8 by using the mean square values. The F_{ratio} is a ratio between the predictable variance of $MS_{R_{1i}}$ and the unpredictable variance of climate noise $MS_{\varepsilon_{1ij}}$. The R^2_{value} is determined for the predictable variance $MS_{R_{1i}}$ and unpredictable variance $MS_{\varepsilon_{1ij}}$ and these values are divided with the total variance $MS_{H_{1ij}}$.

It is important to test the null hypothesis (i.e. $H_{(null)}$), because through the null hypothesis it can be found that some of the $F_{ratio.R_{1i}}$ values are different from the zero.

If $H_{(null)}$ is true: $F_{ratio.R_{1i}} < F(1-\alpha, i-1, i(j-1))$

Do not reject the null hypothesis on all α significant levels

If $H_{(null)}$ is not true: $F_{ratio.R_{1i}} > F(1-\alpha, i-1, i(j-1))$

Reject the null hypothesis on all α significant levels

The α represents the confidence level with 95 % confidence for testing the null hypothesis $H_{(null)}$. The accurate values of the data are obtained through this way, F_{ratio} is investigated for testing the null hypothesis and results or the plots of R^2_{value} will be further shown in Chapter-5. For the simplicity, the variable $R^2_{value.R_{1i}}$ is named as SSB and $R^2_{value.\varepsilon_{1ij}}$ is named as SSE. Here, SSB represents the transient SST effect and SSE is the internal climatic noise estimated for the AOD of HAM-full ensemble. The one-way ANOVA is further used to analyze the AOD of HAM-dir ensemble.

4.3.2 Two-way ANOVA

Two-way ANOVA with interaction term is used for this study, because it has flexibility to estimate the three treatments effect: one due to SST, second due to aerosol and third due to their interaction term. The model variable AREB is a dependent variable whereas the aerosol and SST terms are two independent variables.

$$H_{2ijk} = \mu_2 + R_{2i} + S_{2j} + (R_2 \cdot S_2)_{ij} + \varepsilon_{2ijk} \tag{4.9a}$$

$$\overline{\mu_2} = \overline{H_{2000}} \tag{4.9b}$$

$$\overline{R_{2i}} = \overline{H_{2i00}} - \overline{\mu_2} \tag{4.9c}$$

$$\overline{S_{2j}} = \overline{H_{20j0}} - \overline{\mu_2} \tag{4.9d}$$

$$\overline{(R_2 \cdot S_2)_{ij}} = \overline{H_{2ij0}} - \overline{\mu_2} - \overline{R_{2i}} - \overline{S_{2j}} \tag{4.9e}$$

$$\overline{\varepsilon_{2ijk}} = H_{2ijk} - \overline{\mu_2} - \overline{R_{2i}} - \overline{S_{2j}} - \overline{(R_2 \cdot S_2)_{ij}} \tag{4.9f}$$

$$\overline{H_{2ij0}} = \overline{(R_2 \cdot S_2)_{ij}} + \overline{\mu_2} + \overline{R_{2i}} + \overline{S_{2j}} \tag{4.9g}$$

The complete setup of two-way ANOVA model and its components are explained by Equations 4.9. The AREB data is represented by H_{2ijk} and the SST and aerosol variability is estimated by $\overline{R_{2i}}$ and $\overline{S_{2j}}$, respectively. Aerosol effect $\overline{S_{2j}}$ is computed by taking the mean over the number of years and ensemble and it accounts the static variability for aerosol effect. In contrast to this, the mean over ensemble members and ensemble gives the transient SST effect. The mean over the all dimensions of the data (i.e. time, ensemble members and ensemble) gives the $\overline{\mu_2}$. The interaction term $\overline{(R_2 \cdot S_2)_{ij}}$ depends on both the aerosol and SST effect and it explains to which extent the effect of SST differs across the levels of aerosol variability. It is obtained by subtracting the mean over ensemble from the overall mean and the variability of SST and aerosol. The ε_{2ijk} is estimated by taking the difference between H_{2ijk} and the $\overline{H_{2ij0}}$. The subscripts i and j have already been discussed in one-way ANOVA, however, two-way ANOVA includes an additional subscript of k for the ensemble of AREB (e.g. no-aerosol and aerosol).

$$\sum_{j} \overline{(R_2 \cdot S_2)_{ij}} = 0 \tag{4.10a}$$

$$\sum_{i} \overline{(R_2 \cdot S_2)_{ij}} = 0 \tag{4.10b}$$

Equation 4.10 is evaluated for all i and j values. The values of $\overline{(R_2 \cdot S_2)_{ij}}$ are zero only when the values of aerosol variability are observed over the same levels of SST variability. However, those values can be far from zero, when the values of aerosol variability are observed over the different levels of SST variability (Miller, Haden 2006).

$$SS_{H_{2ijk}} = SS_{R_{2i}} + SS_{R_{2j}} + SS_{(R_2 \cdot S_2)_{ij}} + SS_{\varepsilon_{2ijk}} \tag{4.11a}$$

$$SS_{R_{2i}} = kj \sum_{i=1}^{10} (\overline{H_{2i00}} - \overline{\mu_2})^2 \tag{4.11b}$$

$$SS_{S_{2j}} = ki \sum_{j=1}^{10} (\overline{H_{20j0}} - \overline{\mu_2})^2 \tag{4.11c}$$

$$SS_{(R_2 \cdot S_2)_{ij}} = k \sum_{i=1}^{10} \sum_{j=1}^{10} (\overline{H_{2ij0}} - \overline{\mu_2} - \overline{R_{2i}} - \overline{S_{2j}})^2 \tag{4.11d}$$

$$SS_{\varepsilon_{2ijk}} = \sum_{i=1}^{10} \sum_{j=1}^{10} \sum_{k=1}^{2} (H_{2ijk} - \overline{\mu_2} - \overline{R_{2i}} - \overline{S_{2j}} - \overline{(R_2 \cdot S_2)_{ij}})^2 \tag{4.11e}$$

The sum of the squares for the two-way ANOVA is estimated using Equation 4.11, rest of the procedure for the calculation of MS, F_{ratio} and the estimation of the R^2_{value} is similar to the one-way ANOVA computed in Section 4.3.1. The null hypothesis is tested for three treatments of two-way ANOVA named as $F_{ratio.R_{2i}}$, $F_{ratio.S_{2j}}$ and $F_{ratio.(R_2 \cdot S_2)_{ij}}$.

At the end, the R^2_{value} of S_{2j} is recognized as SSA, the R_{2i} as SSB, the interaction term $\overline{(R_2 \cdot S_2)_{ij}}$ as SSI and the ε_{2ijk} as SSE term. In this research, the model data of AREB, temperature, velocity potential and stream function will be analyzed using the two-way ANOVA interaction, because this ANOVA scheme has possibility to estimate the three treatments (i.e. SST and aerosol and interaction term).

4.4 Regression and correlation coefficient

In climate studies, it is possible that one variable Y has some effect onto the other variable X. The Y is the predictand or the dependent variable and the X is the predictor or independent variable. Regression analysis is mainly used to estimate the parameters values and the standard errors. It selects a line, which identifies the least error for the predicted variable given the predictand variable and it also helps in estimating the best possible outcome of the sum of errors or the uncertainties within the data. The linear model is described in Equation 4.12.

$$Y = a + bX \tag{4.12}$$

and the average value of Equation 4.12 is,

$$\overline{Y} = a + b\overline{X} \tag{4.13}$$

Both Y and X should be normally distributed. The parameter a is represented as an intercept (i.e. value of Y, when $X = 0$) and parameter b is a slope value (i.e. change in Y divided by the change in X). For this research, the observational data of AOD and SST will be considered as the X (i.e. predictor) and the model 2m temperature data is considered as the Y (i.e. predictand). The slope and intercept values estimate the most likely data values and in statistics it is known as the maximum likelihood estimation of the two data sets.

The average value of Y is given in Equation 4.13. The difference between the values of Y and mean value of $\overline{Y}$ gives the residual or leftover values of the data. It is the vertical difference between the data points and the straight line of the regression model. It evaluates the appropriate value of the predicted variable X (i.e. AOD data).

$$d = Y - \overline{Y} \tag{4.14}$$

By substituting the value of $\overline{Y}$ from Equation 4.13 into Equation 4.14, d will become:

$$d = Y - a - b\overline{X} \tag{4.15}$$

$$\sum d^2 = \sum (Y - a - b\overline{X})^2 \tag{4.16}$$

The square of the residual Equation 4.15 will estimate the lack of fit to the model data values, as it is stated in Equation 4.16. The positive and negative values in the sum of residuals of the 2m temperature and AOD can cancel each other. The corrected sum of squares of the temperature residuals is estimated by dividing it with the df. The minimum number of the independent data values that goes into the estimate of a parameter is known as df. The estimated sum of squares of the predicted variance SSX_{AOD}, predictand variance SSY_{2m} and the covariance of these two quantities $SSXY_{AOD\cdot 2m}$ are described by Equations 4.17.

$$SSX_{AOD} = \sum X^2 - \frac{(\sum X)^2}{n} \tag{4.17a}$$

$$SSY_{2m} = \sum Y^2 - \frac{(\sum Y)^2}{n} \tag{4.17b}$$

$$SSXY_{AOD\cdot 2m} = \sum X \cdot Y - \frac{(\sum X) \cdot (\sum Y)}{n} \tag{4.17c}$$

For the AOD, the sum is taken over the number of years and for the 2m temperature, it is over the number of years and number of ensemble members. The maximum likelihood of the slope b for both AOD and 2m temperature is given below in Equation 4.18:

$$b = \frac{SSXY_{AOD \cdot 2m}}{SSX_{AOD}} \tag{4.18}$$

As stated earlier in Equations 4.12 and 4.13, the mean value of the $Y = a + bX$ is taken as $\overline{Y} = a + b\overline{X}$. The intercept equation is written below in Equation 4.19:

$$a = \overline{Y} - b\overline{X} = \frac{\sum Y}{n} - b\frac{\sum X}{n} \tag{4.19}$$

The Equation 4.16 can be re-written as:

$$SSE_{AOD \cdot 2m} = \sum (Y_{2m} - a - bX_{AOD})^2 \tag{4.20}$$

The unexplained variation in the predictand variance SSY_{2m} and the sum of residuals $SSE_{AOD \cdot 2m}$ compute the coefficient of determination i.e. $r^2_{AOD \cdot 2m}$.

$$r^2_{AOD \cdot 2m} = \frac{SSY_{2m} - SSE_{AOD \cdot 2m}}{SSE_{AOD \cdot 2m}} \tag{4.21}$$

In Equation 4.21, the case $r^2_{AOD \cdot 2m} = 1$ implies that the variation of the 2m temperature is explained by the variation in the AOD. The case $r^2_{AOD \cdot 2m} = 0$ shows that none of the variation in the 2m temperature is due to the AOD.

The correlation coefficient $r_{AOD \cdot 2m}$ can be estimated by using Equation 4.21. However, a different formula is used to retain the sign of positive and negative correlation between X and Y. It is given below:

$$r_{AOD \cdot 2m} = \frac{Cov(X_{AOD}, Y_{2m})}{s_{AOD} \cdot s_{2m}} = \frac{SSXY_{AOD \cdot 2m}}{\sqrt{SSX_{AOD} \cdot SSY_{2m}}} \tag{4.22}$$

From the Equation 4.22, the $SSXY_{AOD \cdot 2m}$ is the covariance between AOD and 2m temperature, the SSX_{AOD} is the sum of squares of the AOD variation and the SSY_{2m} is the 2m temperature variation, all these values are stated in Equation 4.17 (Crawley 2013).

5 Results

In this chapter, the results of one-way and two-way ANOVA will be discussed. The chapter's main scheme is illustrated in Figure 5.1. The relationship between the aerosol optical depth (AOD) and the SST induced variability (SIV) will be investigated by utilizing the one-way ANOVA. The results of atmospheric radiative energy balance (AREB) over the global and zonal mean scales are already discussed in Chapter 3. Now, the local projection of aerosol will be analyzed here. For this, the two-way ANOVA interaction setup will be utilized and the data of AREB, temperature and large scale circulation will analyzed through it. Only the significant part of the aerosol and SST variability will be shown in this chapter.

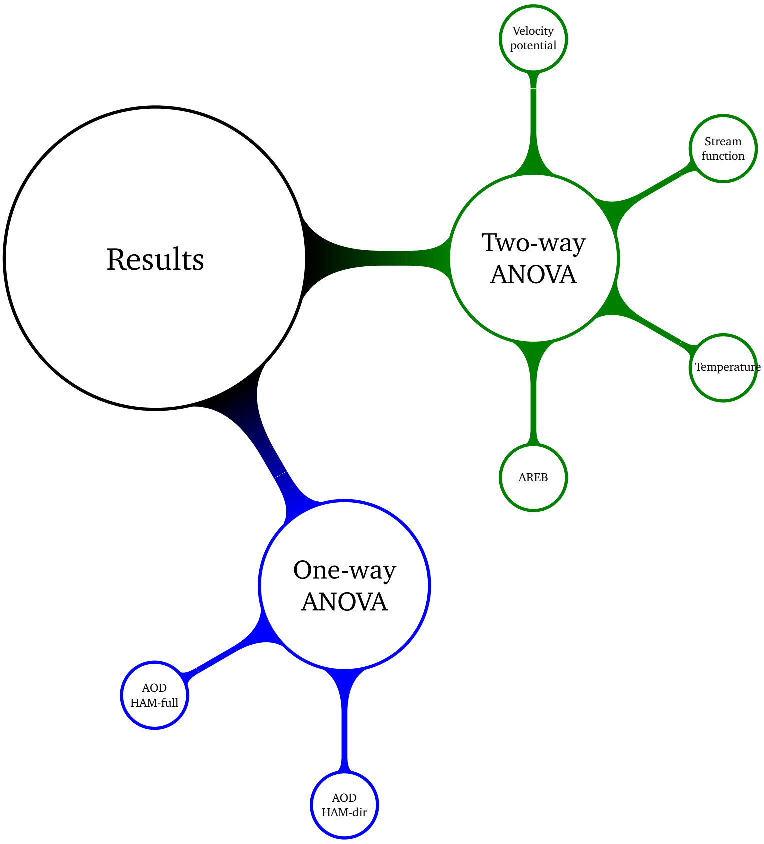

Figure 5.1: Schematic diagram of ANOVA model results

5.1 Results of the one-way ANOVA

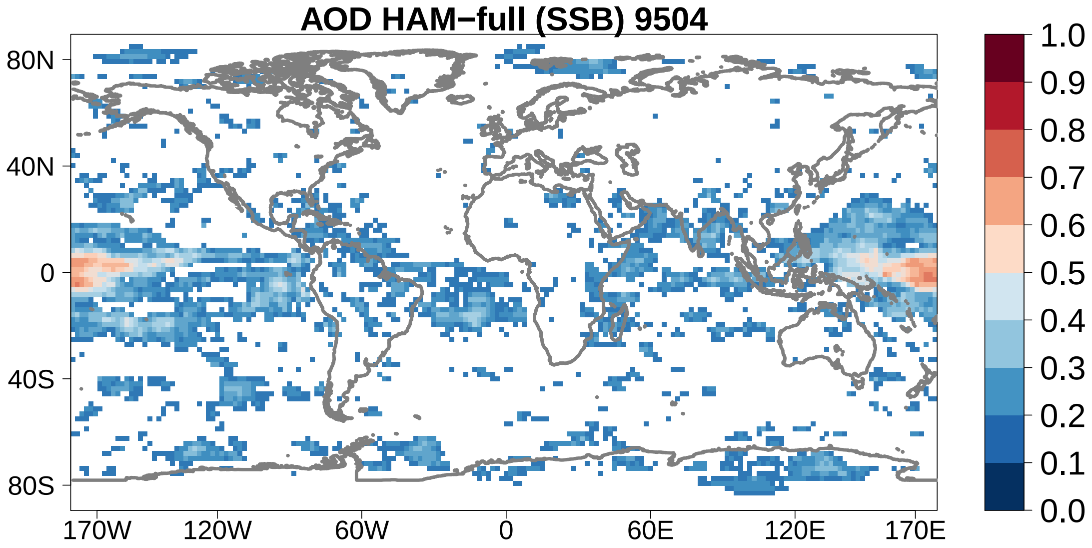

Figure 5.2: The projection of SST induced variability out of the AOD is estimated using one-way ANOVA. The variable AOD is the part of the HAM-full ensemble. The non-significant values less than 5 % are not plotted because the null hypothesis is not rejected for those values. The data is analyzed between 1995 to 2004.

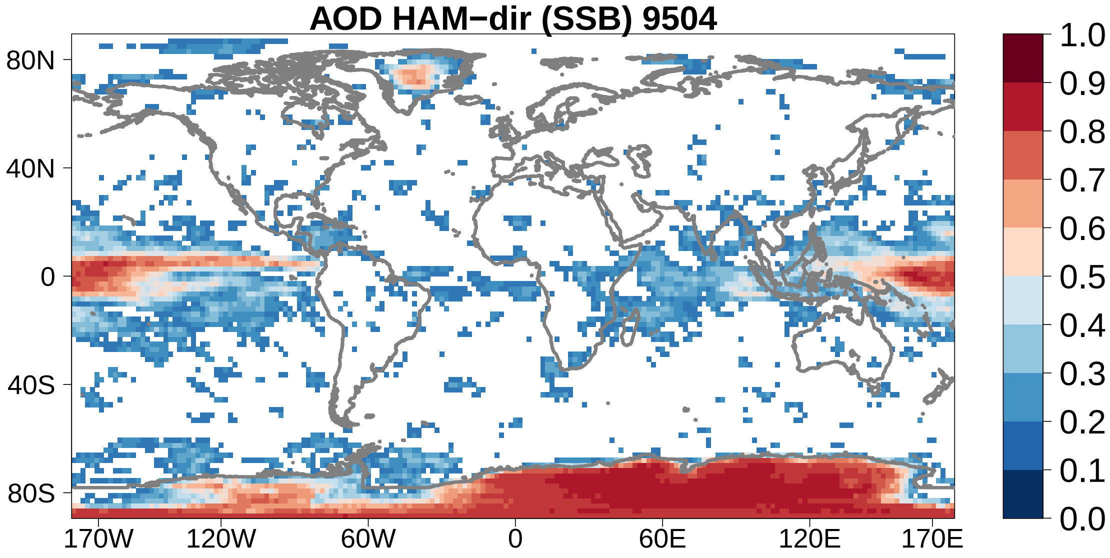

Figure 5.3: Same as in Figure 5.2 but for HAM-dir ensemble.

One-way ANOVA is used to analyze the relationship between the SIV and AOD of HAM-full and HAM-dir ensemble. Figures 5.2 and 5.3 exhibits the results of SIV concluded by the ANOVA. In case of HAM-full ensemble, the projection of SIV does not show any relationship with the AOD and only a signal due to SST forcing is observed over the central Pacific, as shown in Figure 5.2. A similar structure of SIV can be seen in Figure 5.3 but in this case the signal is pronounced when the HAM-dir ensemble is analyzed. The variability over the polar region might be due to the prescribed sea ice data. The difference between two simulation depends on the different aerosol treatment utilized in making these ensemble. The SIV signal over central Pacific might be due to the strongest El-Niño response between the 1997 and 1998 (http://ggweather.com/enso/oni.htm).

Most of the variability in both cases is due to the internal climatic noise but it is not plotted here, because it is just the reciprocal of SIV. Statistically, SIV can only be changed by the internal climatic noise (i.e. SSE) of ANOVA. The strong maxima of SSE will lead to a weaker SST signal and vice versa.

5.2 Results of two-way ANOVA

The two-way ANOVA considers three independent variables. The aerosol induced variability (AIV) is represented by the SSA term, the SIV is given by the SSB term and the interaction term between aerosol and SST is denoted by the SSI. The model variables named as AREB, temperature, velocity potential and stream function are investigated by using the two-way ANOVA. This statistical technique mainly deals with the two ensemble: (1) no-aerosol vs aerosol, (2) aerosol vs HAM-full and (3) aerosol vs HAM-dir. Through this sequence the model variables will be investigated in next sections. In general, aerosol directly affects the atmospheric energy balance and temperature. The AREB is mainly related to the diabatic heating which is proportional to the temperature tendency.

5.2.1 Atmospheric radiative energy balance as a static variable

(1) no-aerosol vs aerosol: The AREB variability is categorized into four components: (i) spatial scale (ii) ten years (iii) ten ensemble members and (iv) two ensemble. The aerosol induced variability (AIV) is obtained by taking the mean over ensemble (i.e. no-aerosol and aerosol) and the mean over ten years. The AIV of the ECHAM6 AREB case is approximately 80 % significant over the tropical and sub-tropical regions, as shown in Figure 5.4. The projection of the tropical aerosol variability show that these aerosol have potential to affect the AREB.

The green contours indicates the absorption of up to 2 W·m^{-2} in the atmosphere and the gain in AREB. The magenta contours show a reduction of up to -0.2 W·m^{-2} in the AREB. In this case, all energy can transmit through the atmosphere and can reach to the earth's surface. The energy surplus due to aerosol absorption is mainly concentrated over Africa, south American and Indian continents and the loss of the energy is assessed mainly over south Pole. Kim *et al.* 2010 also found that over west Africa and eastern Atlantic, the aerosol direct radiative forcing increases the atmospheric stability and reduces the convective precipitation. Similarly, Sena *et al.* 2013 critically pointed out that the biomass burning and the deforestation of the Amazon strongly affects the convection, cloud development and carbon uptake by the forest.

(2) aerosol vs HAM-full: The relative contribution of the AIV in HAM-full ensemble compared to patterns in Figure 5.4 is shown in Figure 5.5. Most of the AIV between 70 % to 80 % reside within the tropical and the subtropical range. In the contour plot, the gain in AREB due to the absorption of atmospheric aerosol is up to 2 W·m^{-2} and the maxima of this variability is observed over the Pacific, American and Eurasian continent, south pole and Africa. The loss

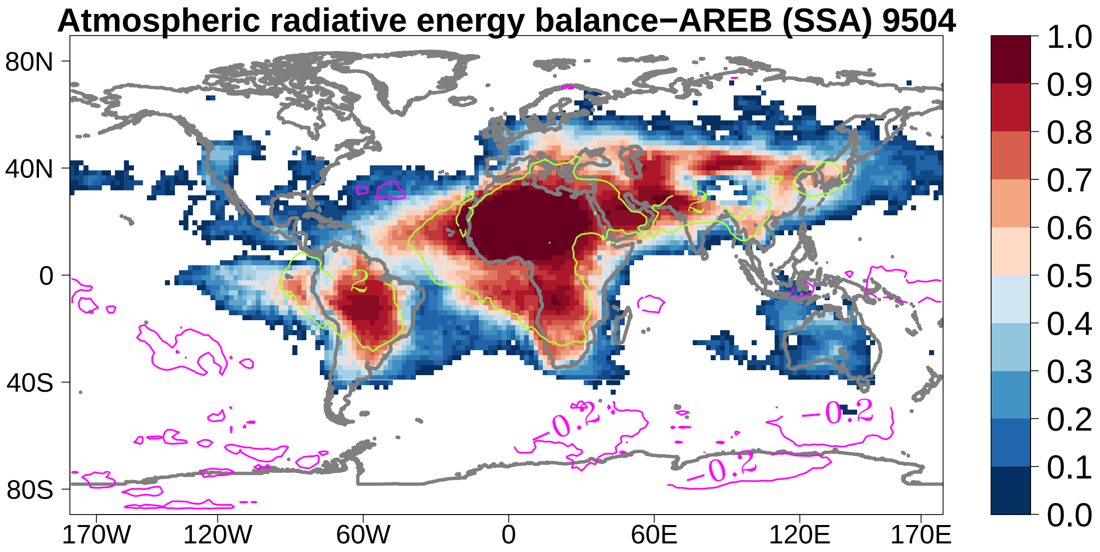

Figure 5.4: The projection of aerosol induced variability of the AREB is estimated using two-way ANOVA. It is estimated using the transient aerosol climatology of the Kinne et al, (2006). SSA is the relative contribution of the aerosol effects upon the total variability compared to the no-aerosol ensemble which is used to estimate the SST induced and internal variability (i.e. no-aerosol vs aerosol ensemble). The non-significant values less than 5 % are not plotted because the null hypothesis is not rejected for those values. The contour plot represents the simple difference between no-aerosol ensemble and aerosol ensemble for the AREB. The green contour values indicate the reduction in the radiative energy loss up to 2 W·m^{-2} and the change in the horizontal energy transports and the divergences. The magenta contour values represents the radiative energy loss of up to -0.2 W·m^{-2}. The data is analyzed between 1995 to 2004.

in the AREB for the aerosol case is up to -2 W·m^{-2} and it mainly affects the eastern China, Indian ocean, north Africa and the coast near Australia. It might be associated with the natural aerosol activity in those region.

(3) aerosol vs HAM-dir: In Figure 5.6, the relative contribution HAM-dir ensemble is sensitive in estimating the AIV compared to the patterns in Figures 5.4 and 5.5. Particularly, this case overestimates the global and zonal mean of AREB, see Sections 3.2 and 3.3. More than 80 % of the AIV projection is detected over tropical regions. From the contours, the energy gain in the HAM-dir ensemble is up to 2 W·m^{-2} and its maxima is located over the American and Eurasian continents, Pacific, south Africa and southern oceans and over the Pacific. The reduction in the energy for the aerosol case is up to -2 W·m^{-2} and it is seen over the north Africa, Indian ocean and Atlantic.

The HAM-model ensemble compute the AIV interactively and aerosol sources and the sinks are present in this case. The patterns of aerosol projection in the HAM-model ensemble is quite sparse. The absorption due to dust aerosol over north Africa strongly affects the AREB of ECHAM6 ensemble compared to the AREB of HAM-model cases, which might also link with short life time of aerosol in HAM-model cases. The patterns in the Figures 5.5 and 5.6 are associated with the absorption of the natural or anthropogenic aerosol.

For the HAM-model ensemble, the projection over the Polar region is interpreted as the higher sensitivity of the radiative aerosol effects due to the surface albedo over ice. The overall

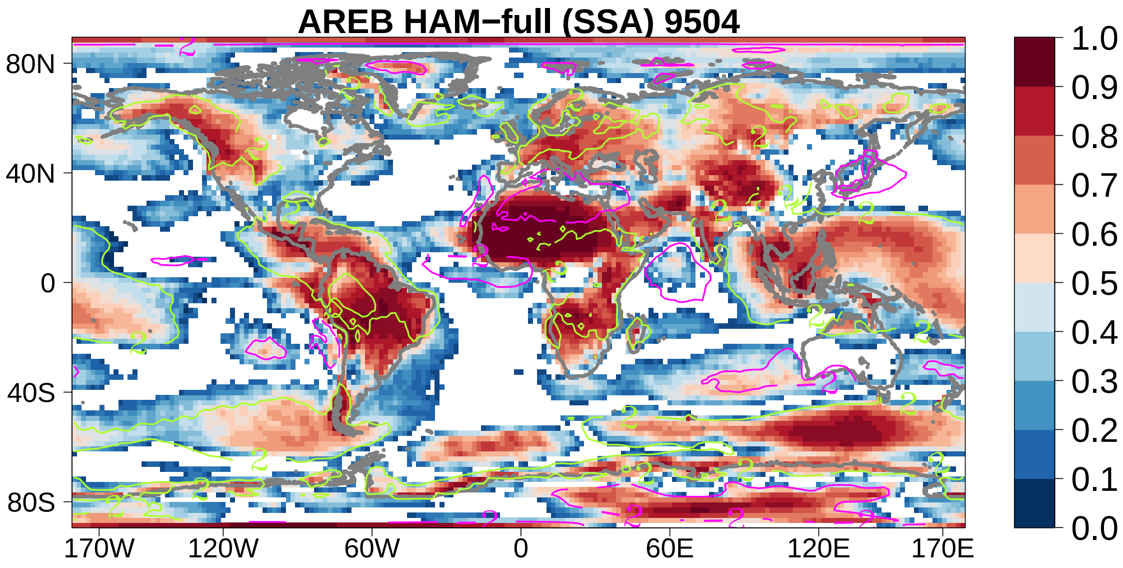

Figure 5.5: It represents the relative change of the pattern of aerosol induced variability from Figure 5.4 to Figure 5.5. It is for the aerosol vs HAM-full ensemble. The green contour values indicate the reduction in radiative energy loss up to 2 W·m^{-2} and magenta contour indicates the loss of radiative energy up to -2 W·m^{-2}.

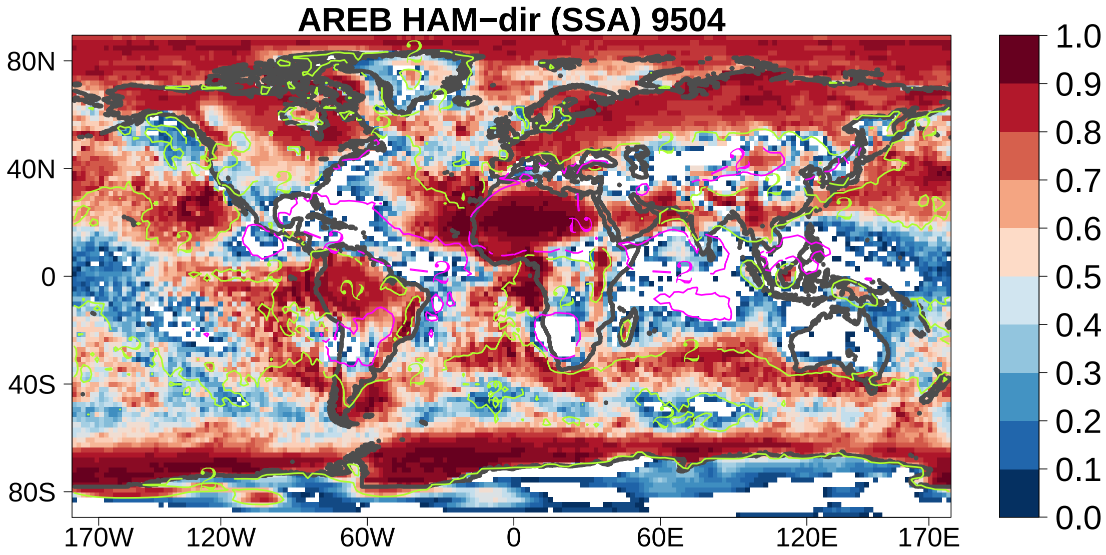

Figure 5.6: It represents the relative change of the pattern of aerosol induced variability from Figure 5.4 to Figure 5.6. It is for the aerosol vs HAM-dir ensemble. The green contour indicates the less loss of radiative energy up to 2 W·m^{-2}. Over west of Africa, the magenta contour indicates a small but significant reduction in radiative energy up to -2 W·m^{-2} as compared to Figure 5.4.

effect upon AREB might be small but the AIV is still significantly different from zero. The aerosol projection over the tropics has ability to affect the AREB. Herman *et al.* 1997 showed the major aerosol source regions for the absorbing aerosol are in the south America (Brazil), Africa, Arabian peninsula and the north part of India. Furthermore, they described that the forest fire or the agricultural burning in eastern China, Indonesia and Amazon region is also projected as the source region for the absorbing aerosol. Each year, these absorbing aerosol of Africa and Brazil are injected into the atmosphere and the atmospheric wind system advect these aerosol outside of their source regions.

The major maxima of AREB in all ensemble are observed over the tropics. In the troposphere, aerosol optical properties changes the radiation budget. The changes in incoming solar radiation due the aerosol particles affect the atmospheric temperature. The changes in the temperature can be balanced by a lot of other atmospheric processes like convection and the horizontal and vertical large-scale transports of pollutants. Webster, Chou 1980 highlighted the changes in the vertical velocity is related to the divergence flow field and the tropical divergence flow has potential to affect the rotational flow field. Therefore, the model data is further analyzed for the temperature and large scale circulation.

5.2.1.1 AREB due to interactive term and climate noise

The predicted variance of AREB for the ECHAM6, HAM-full and HAM-dir ensemble is due to the AIV. In contrast to AIV, the SIV did not show any strong trend for all of the AREB's realizations and hence not plotted. The interaction term (SSI) depends on both, AIV and SIV variability. In this case, the SIV is nearly zero, so it will not possible to get a reasonable signal for SSI. The climatic noise SSE is just opposite to the SIV, therefore it is not shown here.

5.2.2 Temperature as a thermodynamical variable

Aerosol can change the thermodynamical structure of the atmosphere. Bony *et al.* 2004 suggested that it is difficult to estimate the changes in temperature that results from the aerosol variability. Ramanathan, Collins 1991 found a strong correlation between the radiative forcing (RF) and SST over the tropics. Pierrehumbert 1995 suggested that the temperature over the tropics can be taken as the boundary condition for the extra-tropical climate and it is important in regulating the global climate. The AIV can affect temperature as it has been discussed earlier in Section 5.2.1.

5.2.2.1 2m temperature due to aerosol induced variability

(1) no-aerosol vs aerosol: The changes in the near surface 2m temperature due to aerosol forcing are analyzed in this section. The predictable variance of AIV is shown in Figure 5.7. The AIV for the 2m temperature contributed up to 40 % over the west African region and the maxima in this case interprets the local effect of aerosol. In the contour plot, the near surface temperature is projected up to 0.2 °C over the west of Africa. The positive temperature near surface might be due to the radiative energy transmission from atmosphere to the surface when there are no-aerosol in the atmosphere. Usually, aerosol in the atmosphere block the SW radiation and heat the atmospheric column, therefore they cool the surface. The magenta contour represents the cooling of -0.2 °C over the American and Eurasian continents and also over the central and south of Africa regions. Some regional model studies predicted the cooling due to the dust aerosol over the west of Africa (Marcella, Eltahir 2014). However they did not take into account the LW radiation effect which could change the heating signal. Klein, Hartmann 1993 pointed out that the reduction in aerosol concentration is associated with the increase in surface temperature. An increase in the surface temperature is related to

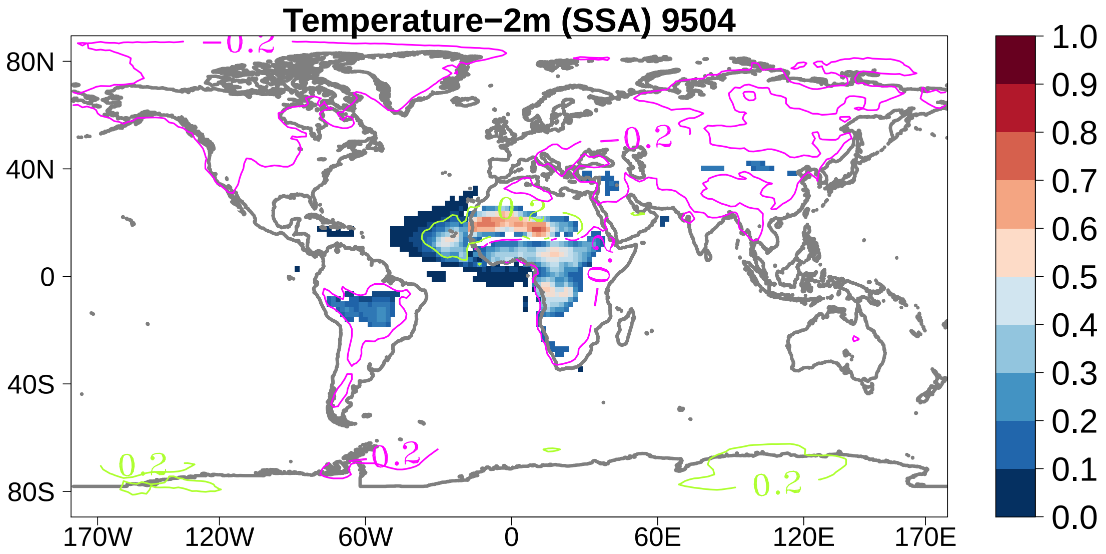

Figure 5.7: Same as in Figure 5.4 but for the 2m temperature of no-aerosol vs aerosol ensemble. The contour plot represents the simple difference between no-aerosol ensemble 2m temperature and aerosol ensemble 2m temperature. The green contour values indicate an increase in the temperature or warming of up to 0.2 °C, when $Temp_{(no-aerosol)} > Temp_{(aerosol)}$. The magenta contour values represents the decrease in temperature or cooling of up to −0.2 °C as $Temp_{(aerosol)} > Temp_{(no-aerosol)}$. The data is analyzed between 1995 to 2004.

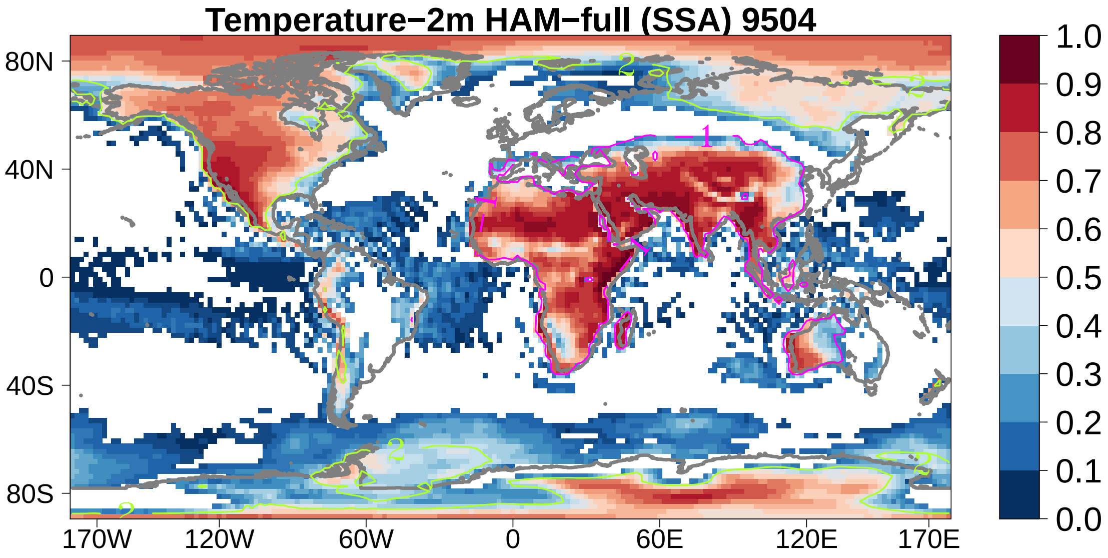

Figure 5.8: It represents the relative change of the pattern of aerosol induced variability from Figure 5.7 to Figure 5.8. The green contour indicates the warming of up to 2 °C and the magenta contour represents the cooling of up to −1 °C.

the low-level static stability. In convective systems, precipitation efficiency increases with the temperature (Del Genio, Kovari 2002).

(2) aerosol vs HAM-full: The HAM-full case in Figure 5.8 represents the relative change to the pattern in Figure 5.7. The predictable portion of the AIV for the 2m temperature is mostly

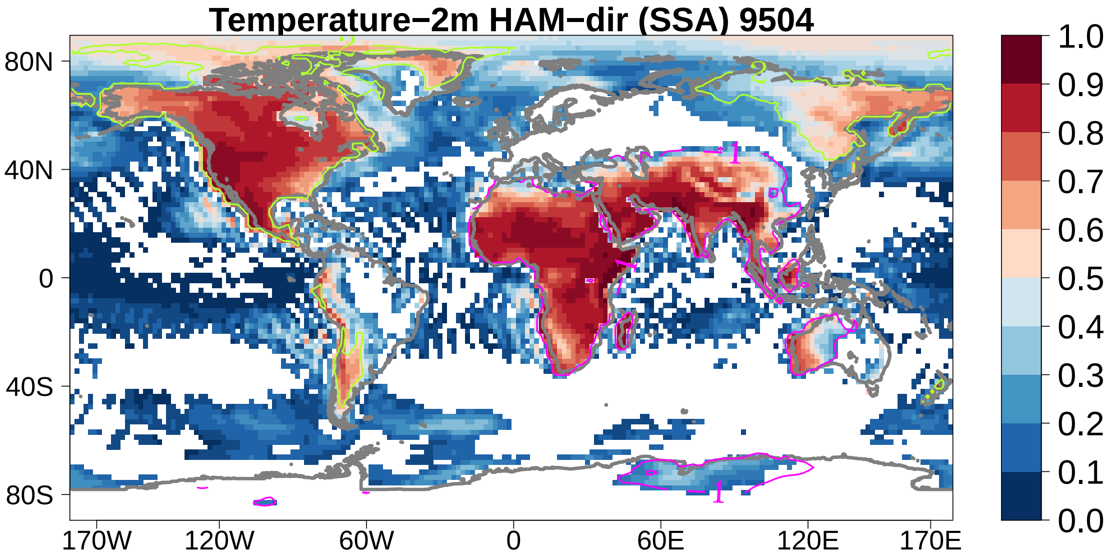

Figure 5.9: It represents the relative change of the pattern of aerosol induced variability from Figure 5.7 to Figure 5.9. The contour description is same as in Figure 5.8

concentrated over the tropical regions and it is 50 to 70 % significant. Part of this variability over the mid and high latitude area might come due to the random effects. Over the north of America and polar regions, a warming trend of up to 2 °C is observed when the $Temp_{(aerosol)} > Temp_{(HAM-full)}$ in green contour and the cooling effect of up to −1 °C over the Australia, Africa and Asia, when the $Temp_{(HAM-full)} > Temp_{(aerosol)}$ in magenta contour.

(3) aerosol vs HAM-dir: Again the relative contribution of HAM-dir ensemble shown some sensitivity in estimating the 2m temperature, as shown in Figure 5.9. Though the structure of the maxima showed some similar patterns over north of America, Africa and Asia, as it has been already shown for the HAM-full ensemble. The AIV for the 2m temperature detected comparatively a good signal of up to 80 % significance over the tropical region. The plain difference between aerosol and HAM-dir in the contour plot showed a cooling pattern. The near surface temperature is showing a warming trend of 2 °C over the American continent and eastern Russia and a cooling of −1 °C over the same region described earlier in Figure 5.8. For 2m temperature, only the relative contribution of HAM-full and HAM-dir ensemble show a reasonable projection due to aerosol variability, the direct effect of aerosol is quite strong in this case.

5.2.2.2 2m temperature due to SST induced variability

(1) no-aerosol vs aerosol: The second predictable part of two-way ANOVA is assessed after taking the mean over the ensemble and ensemble members of the 2m temperature, it gives the transient SIV effect. A good SIV projection for the 2m temperature can be seen in Figure 5.10. The SIV maxima are related to the prescribed SST data used in model. Most of the SST variability is concentrated over the oceanic regions especially over the central Pacific.

(2) aerosol vs HAM-full and (3) aerosol vs HAM-dir: The similar patterns of the SIV for the relative contribution of the HAM-model ensemble can be observed in Figures 5.11 and 5.12. The SIV for the 2m temperature is decreased from 80 % in Figure 5.10 to 70 %, as the

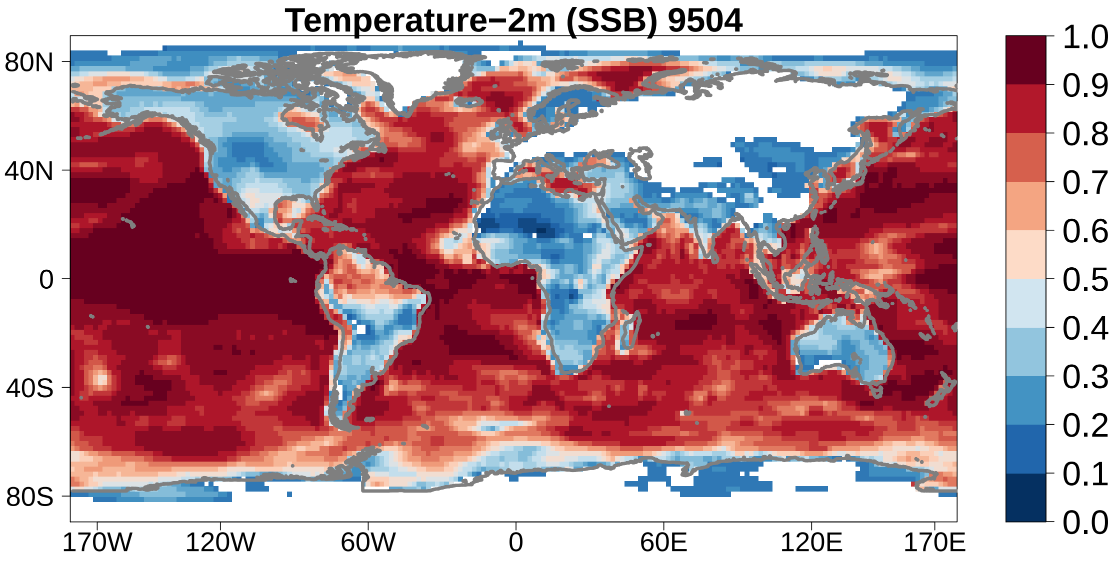

Figure 5.10: The projection of SST induced variability of the 2m temperature is estimated using two-way ANOVA. The variable 2m temperature is the part of the no-aerosol vs aerosol ensemble. The non-significant less than 5 % are not plotted because the null hypothesis is not rejected for those values. The data is analyzed between 1995 to 2004.

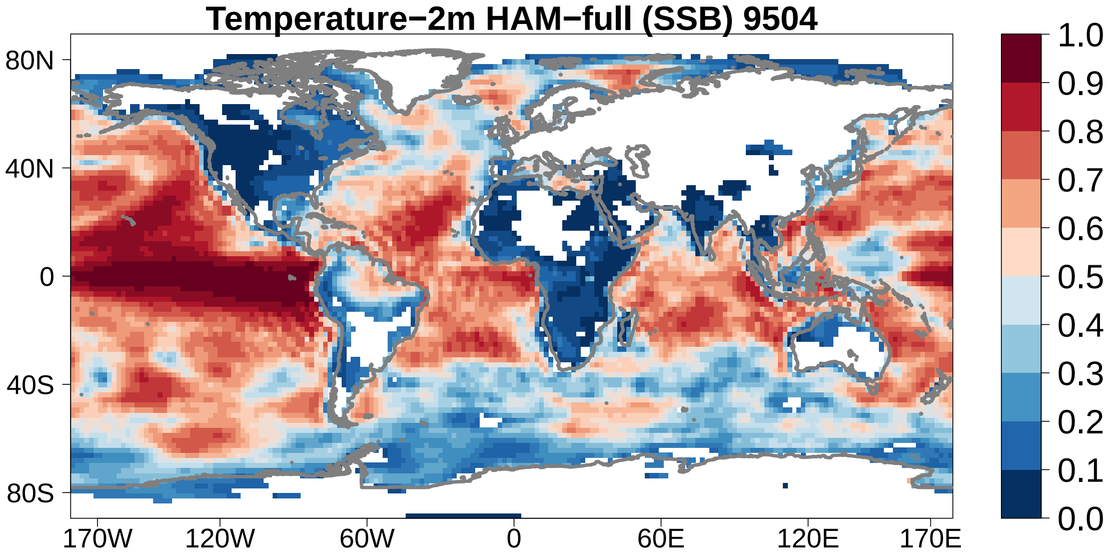

Figure 5.11: It represents the relative change of the pattern of SST induced variability from Figure 5.10 to Figure 5.11. It is for aerosol vs HAM-full ensemble.

interactive aerosol scheme of HAM-model is turned on in ECHAM6.

5.2.2.3 temperature at 850 hPa due to aerosol induced variability

(1) no-aerosol vs aerosol: The lower troposphere temperature at 850 hPa is further investigated to check how the aerosol variability is propagated in the lower atmosphere. The aerosol

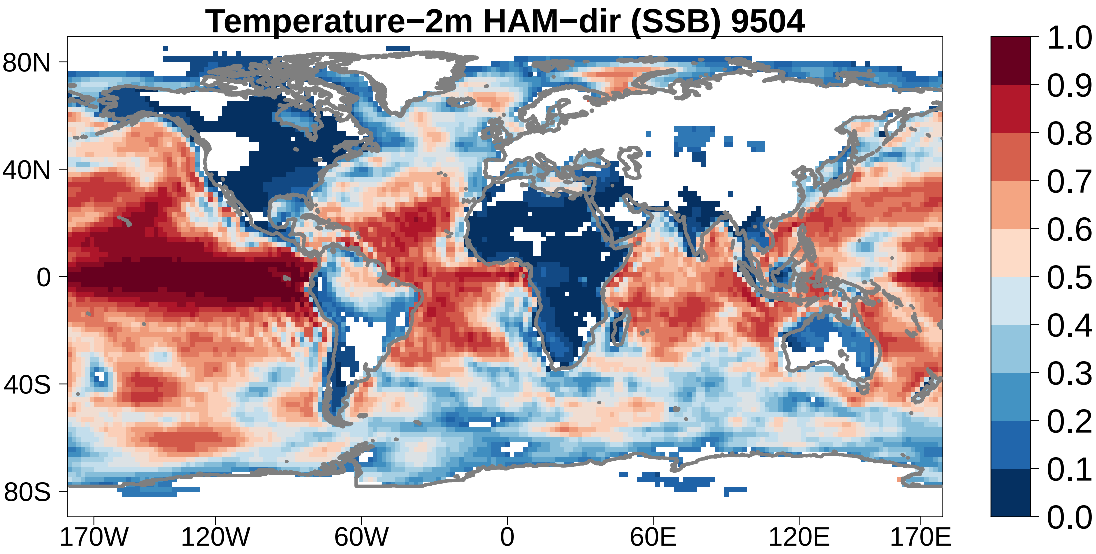

Figure 5.12: It represents the relative change of the pattern of SST induced variability from the Figure 5.10 to Figure 5.12. It is for aerosol vs HAM-dir ensemble.

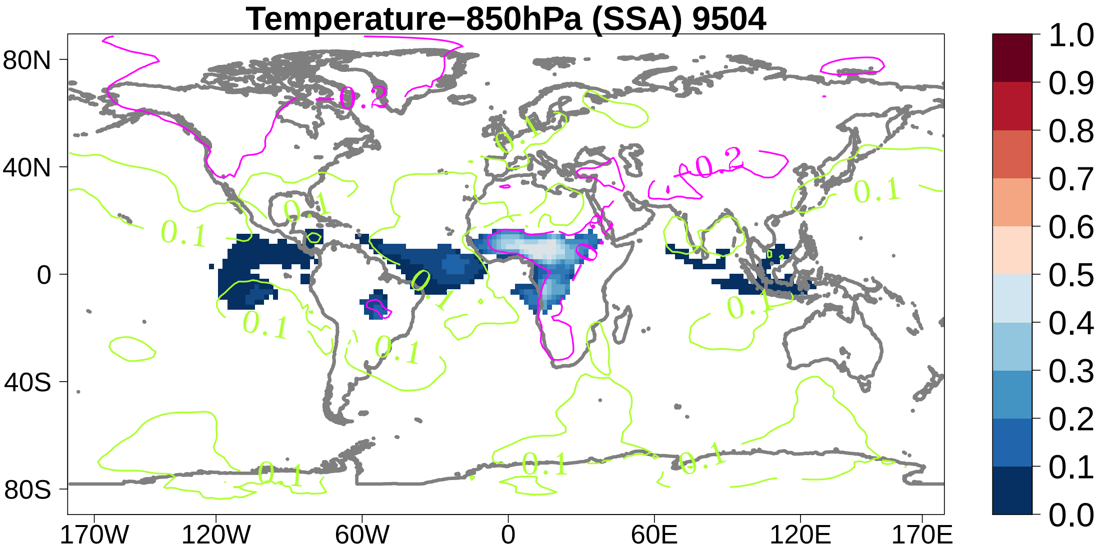

Figure 5.13: Same as in Figure 5.4 but for the temperature at 850 hPa of no-aerosol vs aerosol ensemble. The contour plot represents the simple difference between no-aerosol ensemble temperature at 850 hPa and aerosol ensemble temperature. The green contour values indicate an increase in the temperature or warming of up to 0.1 °C when $Temp_{(no-aerosol)} > Temp_{(aerosol)}$. The magenta contour values represents the decrease in temperature or cooling of up to -0.2 °C as $Temp_{(aerosol)} > Temp_{(no-aerosol)}$. The data is analyzed between 1995 to 2004.

signal for temperature at 850 hPa is damped down compared to 2m temperature, it can be seen by comparing Figure 5.7 with Figure 5.13. The AIV shown 20 % to 30 % significance and the projection of this variability is recorded mainly over the central Africa. The contours have

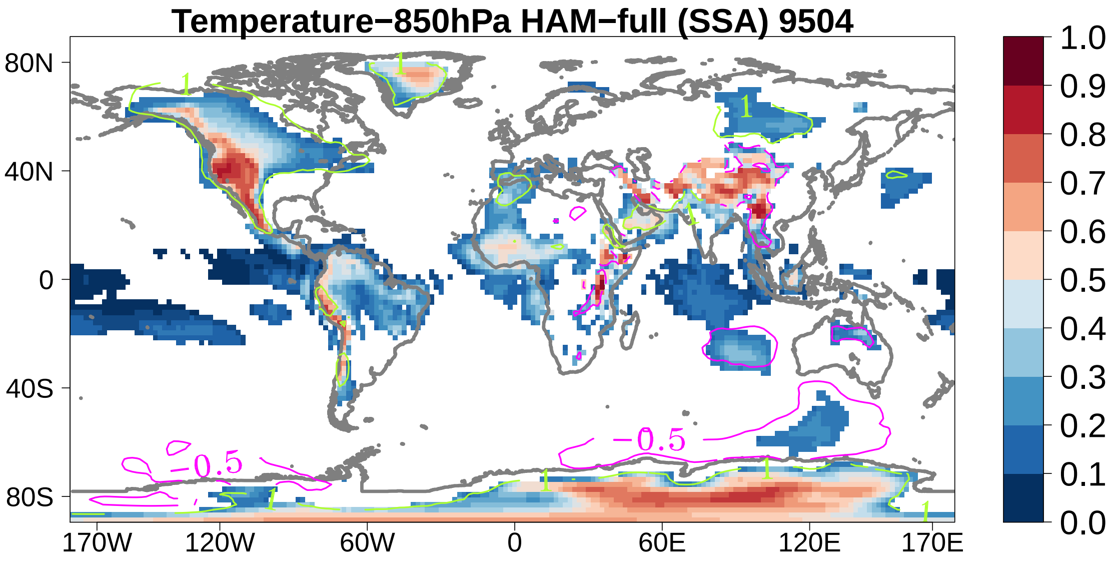

Figure 5.14: It represents the relative change of the pattern of aerosol induced variability from Figure 5.13 to 5.14. It is for aerosol vs HAM-full ensemble. The green contour indicates the warming of up to 1 °C and the magenta contour represents the cooling of up to −0.5 °C.

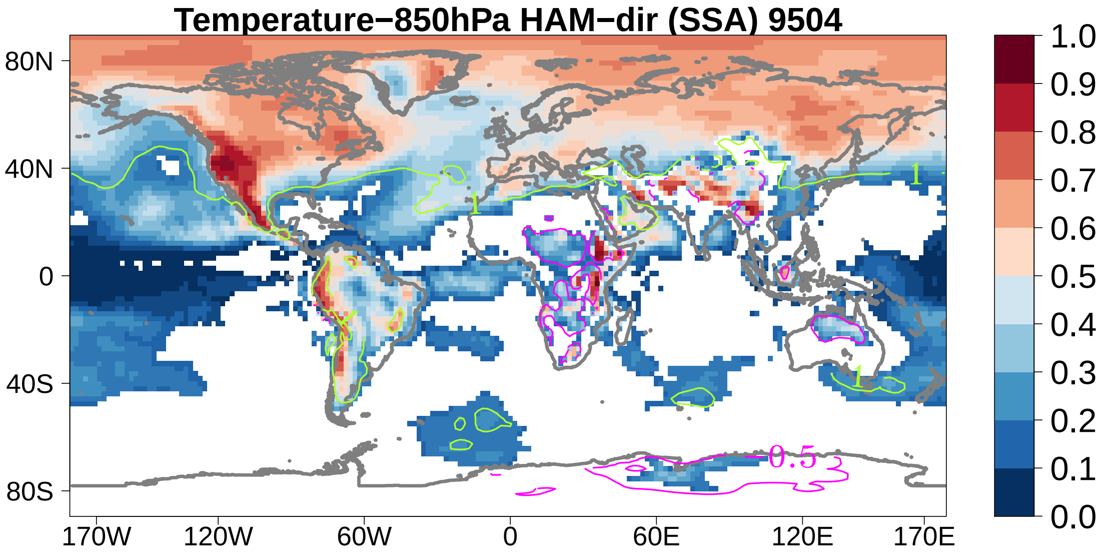

Figure 5.15: It represents the relative change of the pattern of aerosol induced variability from Figure 5.13 to 5.15. It is for aerosol vs HAM-dir ensemble. The contour description is same as in Figure 5.14

been already explained for the 2m temperature but the $Temp_{(aerosol)} > Temp_{(no-aerosol)}$ at 850 hPa warmed the lower atmosphere of the tropics up to 0.1 °C, it is depicted by green contour and the $Temp_{(no-aerosol)} > Temp_{(aerosol)}$ at 850 hPa cooled down the temperature for the central Africa, north of America, Iran and China up to −0.2 °C.

(2) aerosol vs HAM-full: The change in the relative contribution of HAM-full AIV compared to Figure 5.13 for the temperature at 850 hPa is shown in Figure 5.14. The AIV did not show a robust signal here, but for the HAM-full 2m temperature it detected a reasonable signal. The projection of this variability over the western American continent, Greenland, India and south Pole is significant and relatively warm to the no-aerosol vs aerosol ensemble in Figure 5.13. The AIV is recorded between 20 % to 30 % significance over the west and east of Africa. The green contour shows warming of up to 1 °C over the American continent, Greenland, middle East and south Pole and the magenta contour indicates about the cooling of up to -0.5 °C over the part of Indian ocean and continent and the ocean near the south Pole.

(3) aerosol vs HAM-dir: The relative contribution of the HAM-dir AIV compared to the Figure 5.13 is presented in Figure 5.15. The maxima of AIV for the temperature at 850 hPa is reduced as compared to the HAM-dir 2m temperature in Figure 5.9. However this case is relatively warmer than the two other cases in Figures 5.13 and 5.14, especially in the norther Hemispheric regions. The value of this variability is within the range of 20 % to 30 %, mainly over the Arabian ocean. The green contour indicates the warming of up to 1 °C over the northern Hemisphere and parts of south America whereas the magenta contour indicates the cooling of up to -0.5 °C over central and south of Africa and part of south Pole. The AIV for the 2m temperature and temperature at 850 hPa estimated by two-way ANOVA did not project a good signal as compared to the AREB.

5.2.2.4 temperature at 850 hPa due to SST induced variability

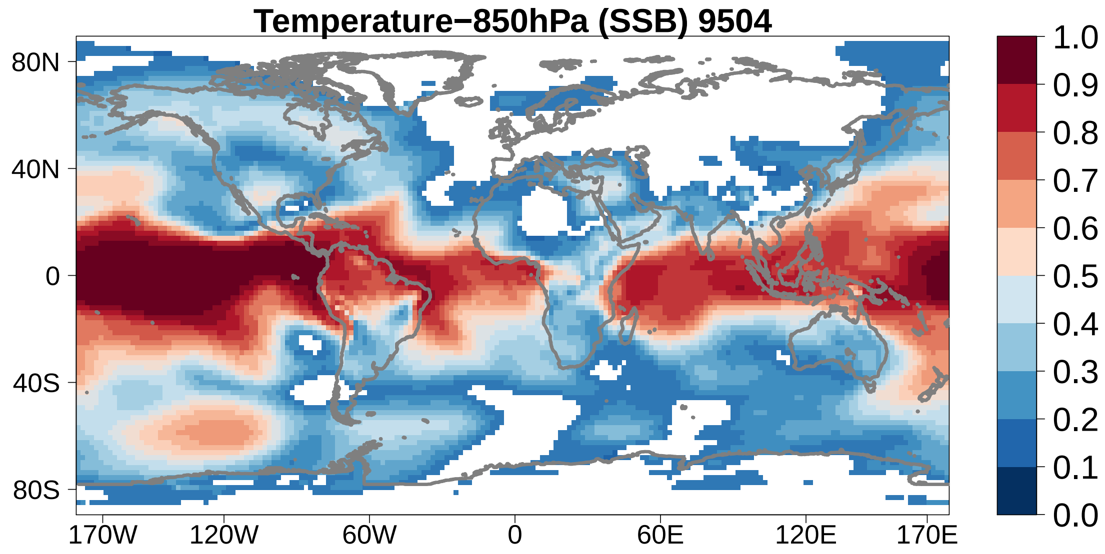

Figure 5.16: Same as in Figure 5.10 but for the temperature at 850 hPa. It is the part of the no-aerosol vs aerosol ensemble.

(1) no-aerosol vs aerosol: The SIV for the temperature at 850 hPa is dropped down to 50 % over the oceanic regions, as shown in Figure 5.16. However, the SST signal over central Pacific is still projecting a reasonable trend of up to 80 % significance.

(2) aerosol vs HAM-full and (3) aerosol vs HAM-dir: A similar spatial structure can be seen for the HAM-model cases, it can be seen in Figures 5.17 and 5.18. The SIV for the temperature at 850 hPa is decreased from 50 % to 40 % for HAM-model ensemble compared to no-aerosol vs aerosol ensemble.

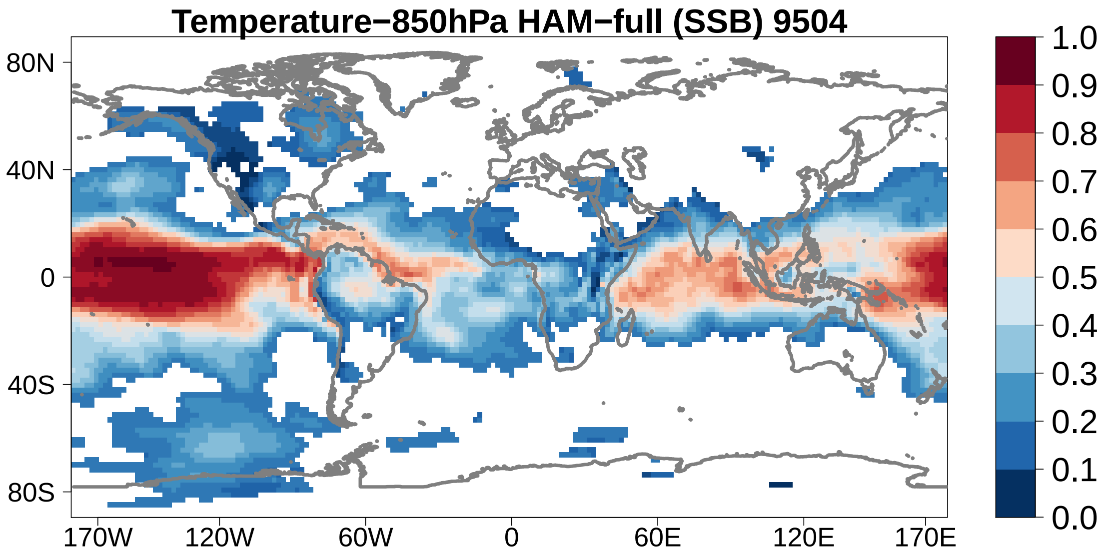

Figure 5.17: It represents the relative change of the pattern of SST induced variability from Figure 5.16 to Figure 5.17. It is for aerosol vs HAM-full ensemble.

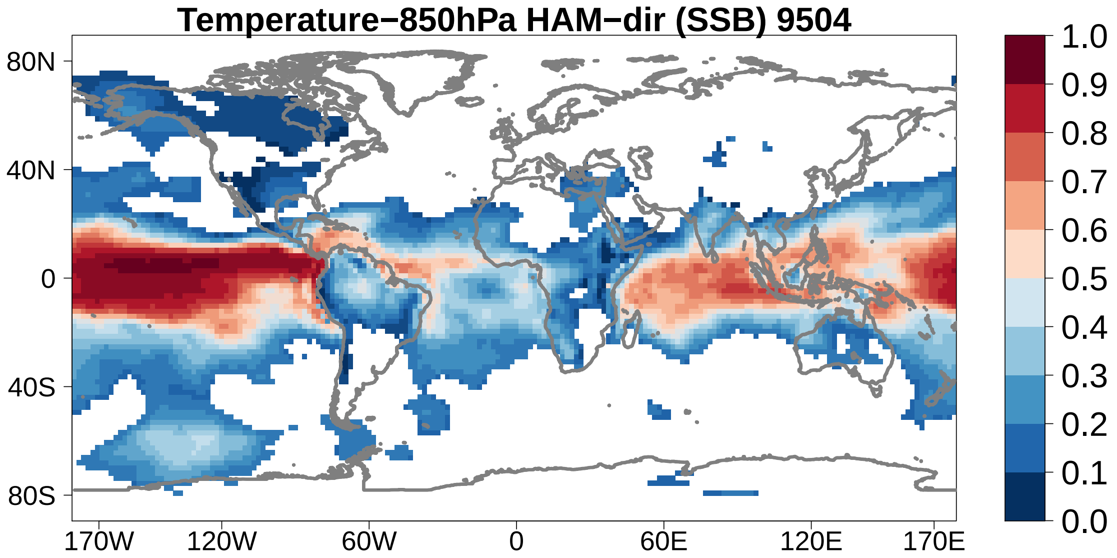

Figure 5.18: It represents the relative change of the pattern of SST induced variability from Figure 5.16 to Figure 5.18. It is for aerosol vs HAM-dir ensemble.

It has been stated earlier that ECHAM6-HAM is not coupled with the ocean model and it utilized the prescribed SST data as an alternative. It means no real ocean is included in this study. Therefore, the SIV signal is pronounced because no actual feedback exists between the atmosphere and ocean. The variability of SST which injected into the system, it resides there. However, the SIV is decreased when the aerosol model HAM is integrated with the ECHAM6, because in this case the aerosol have sources and sinks. The SIV is not much affected when the aerosol climatological data is utilized in ECHAM6.

5.2.2.5 Temperature vertical profile for aerosol and SST induced variability

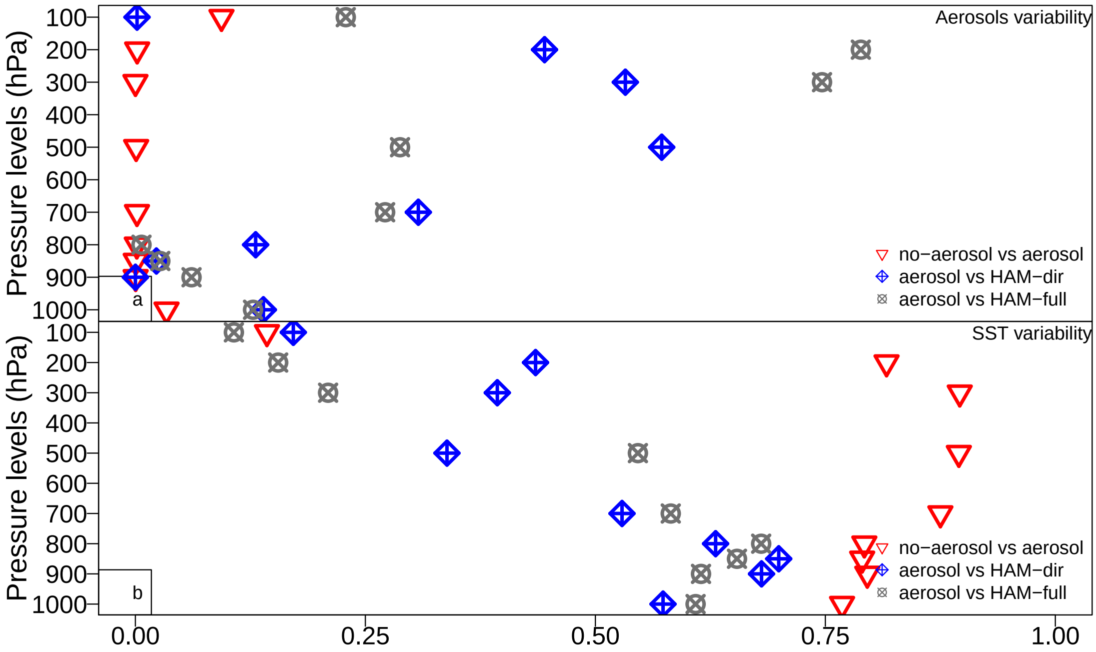

Figure 5.19: The vertical profile of temperature is estimated by using two-way ANOVA for all model realizations. On the x-axis, the $R^2 - value$ (i.e. a ratio between the treatment variance and the total variance) of ANOVA is plotted and it is in percentage (%). On the y-axis, the pressure levels from 1000 hPa (surface) to 100 hPa (atmosphere) are shown. First, the mean over all grid points is taken, except the vertical pressure levels. Second, the ANOVA model is implemented on the data. (a) The AIV is affecting up to 5 % the near surface temperature for no-aerosol vs aerosol ensemble, between 10 % to 20 % the near surface temperature and between 25 % to 75 % the middle and upper tropospheric temperature for aerosol vs HAM-full ensemble and between 10 % to 20 % the near surface temperature and between 25 % to 55 % the middle and upper tropospheric temperature for aerosol vs HAM-dir ensemble. (b) The SIV is strongly affecting the atmospheric temperature between 70 % to 80 % for no-aerosol vs aerosol ensemble, between 30 % to 70 % for aerosol vs HAM-full ensemble and between 30 % to 70 % for aerosol vs HAM-dir ensemble. The data is analyzed between 1995 to 2004.

As most of the AIV is concentrated between 30°N and 30°S for the AREB and in the temperature variables. Therefore, the treatment affect of the AIV and SIV for the temperature vertical profile is analyzed in Figure 5.19. The AIV is approximately zero for the no-aerosol vs aerosol ensemble. It strongly affected the middle and upper tropospheric temperature by the relative contribution of the aerosol vs HAM-model ensemble. The HAM-model cases have approximately 50 % higher AIV compared to the no-aerosol vs aerosol ensemble especially between 500 to 200 hPa. However, the SIV is showing a strong trend for the temperature in no-aerosol vs aerosol case. The value of the SIV is decreased for the aerosol vs HAM-model cases. The ANOVA results obtained for the 2m temperature and temperature at 850 hPa do have a agreement with the temperature vertical profile of ANOVA. It can be observed here that as the AIV is increased then the SIV is decreased and vice versa. Both these quantities depend on each other.

For the temperature, most of the predictable variance is due to the SIV and in a small proportion it is due to AIV. The SSI variability for the temperature is approximately zero. Therefore, it is not presented here. Bony *et al.* 2004 describes that the temperature variability is often associated with the circulation patterns in the atmosphere.

5.2.3 Large scale circulation

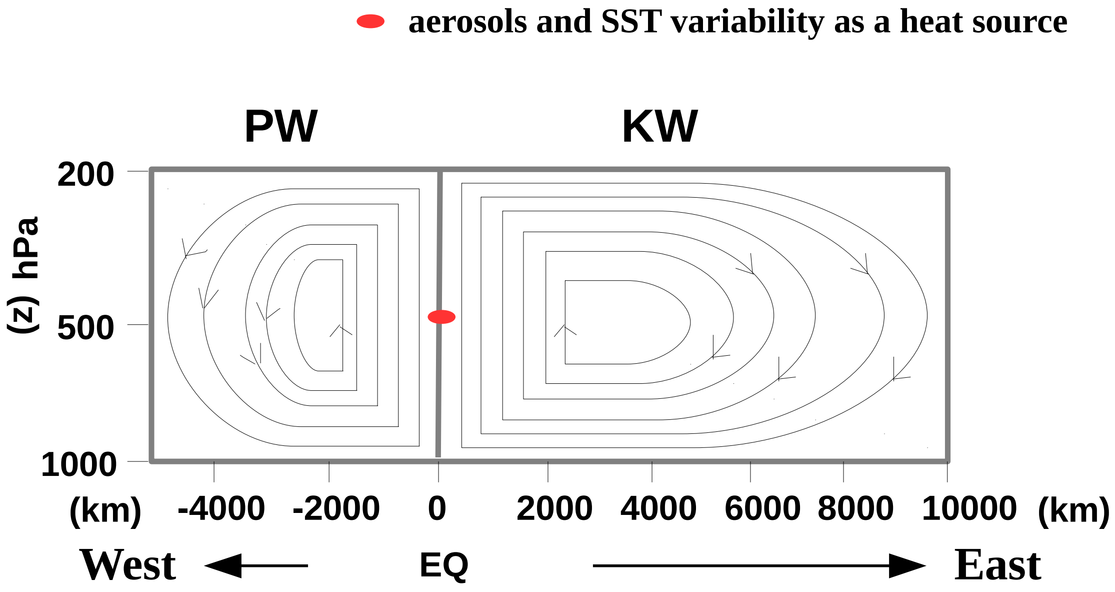

(a) Deep response (aerosols and SST variability) and faster baroclinic mode

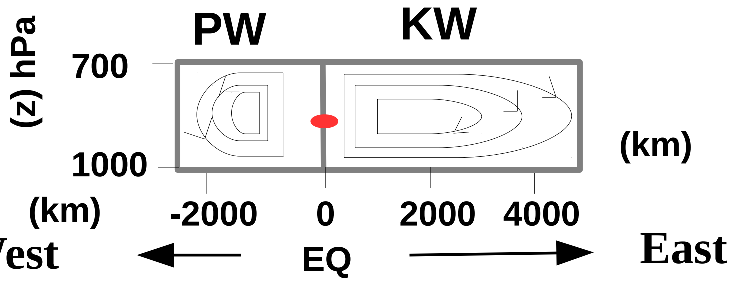

(b) Shallow response (aerosols and SST variability) and slower baroclinic mode

Figure 5.20: The Structural phase velocity diagram of the tropospheric atmosphere (a) aerosol and SST variability vertical response deep response (b) aerosol and SST variability vertical shallow response.

In the real atmosphere, net heating is not zonally symmetric, but the incoming solar radiation is symmetric. Therefore, the total heating in the atmosphere depends on the distribution of clouds or aerosol as well as on the surface properties. This chapter elucidates that how aerosol changes the diabatic heating, convective intensity and regional circulation under different environmental conditions. The direct and indirect effects of the aerosol can enhance the regional convergence (i.e. deep convective clouds) and lead to the top-of-atmosphere heating, they can potentially affect regional circulation and alter the weather system (Bony *et al.* 2004).

The dynamical response of the atmosphere to the imposed heating due to AIV and SIV is shown in Figures 5.20a and 5.20b. The fastest and longest baroclinic mode (BM) for the AIV and SIV in the atmosphere can be seen in Figure 5.20a. The atmosphere which shapes the cyclones and anticyclones is characterized as a baroclinic atmosphere. The tropical atmosphere basically reacts through the baroclinic modes due to the vertical structure of the internal heating which peaks at some intermediate level in the troposphere. The difference between the 200 and 1000 hPa indicates the projection on the faster baroclinic mode (FBM). Here, the Kelvin waves (KW) are propagating in eastern direction and planetary waves (PW) or Rossby waves are propagating in the western direction. The PW decays faster than the KW due to the friction and covers the smaller area. The influence of heating expands more to the eastwards but the amplitude of the response is more dominant to the westwards. These waves can strengthen the convection over the Indian and western Pacific ocean (Gill 1982). According to phase velocity model shown in Figure 5.20a, the AIV and SIV do have potential to affect the circulation over the large scale. The rising motion initiates over the heating region (i.e. due to aerosol and SST) and it sinks within the vicinity of thousands kilometers.

The slowest or shortest BM for the AIV and SIV can be seen in Figure 5.20b. The difference between 700 and 1000hPa denotes the projection on the slower baroclinic mode (SBM). For this mode, the KW and the PW cover only the short distance in eastwards and westwards, respectively. Also, the rising motions here is associated with the heating due to the AIV and SIV and it sinks after covering the distance of few thousands kilometers.

In both cases, the subsidence occurs in the heat sink region with the convergence in the upper atmospheric levels and divergence in the lower atmospheric levels. These motions are characterized as the weak cyclonic and anticyclonic circulations, away from the Equator. It means that the flow field is typically baroclinic as stated earlier and the upper level flow field do have opposite sign to those at the lower level flow field. In high latitude areas, the height contours become nearly parallel to the flow and indicates the dominance of the rotational flow (Gill 1982). The subsidence motion in tropics is associated to the low-level clouds like stratus and strato-cumulus. The ascending motion in tropics is associated to convective clouds between the shallow and deep atmospheric layers. These clouds are sensitive to the temperature changes and can affect the large scale radiation budget (Bony *et al.* 2004).

The atmospheric circulation over the tropics can be analyzed by considering velocity potential (VP) and stream function (SF). The VP represents the large scale tropical divergence flow field and the SF denotes the rotational flow field. It will be investigated further in following sections that which component of flow field contributes distinctly than other.

5.2.3.1 Velocity potential for faster baroclinic mode due to aerosol induced variability

(1) no-aerosol vs aerosol: The deep response of aerosol variability is analyzed for the VP data of no-aerosol and aerosol ensemble and no signal is detected in this case, as shown in Figure 5.21. The low level flow is at 1000 hPa and the upper level flow is at 200 hPa and the difference of these two flow fields (200-1000) hPa represents the projection on the FBM. The green contour in this represents the ascending motion over Atlantic, Africa and south Pole and the magenta contour indicates towards the descending motion over the Pacific.

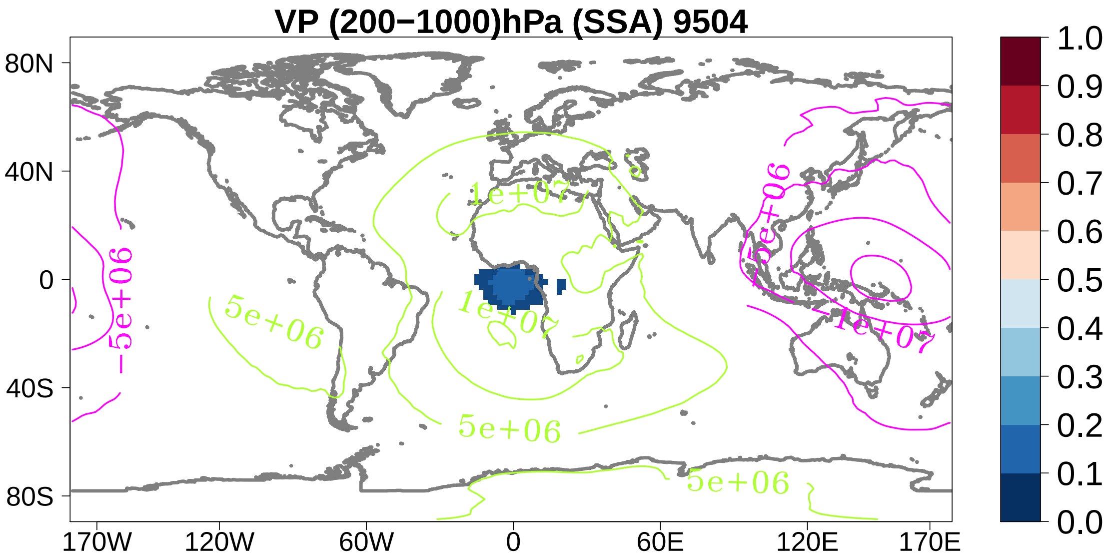

Figure 5.21: Same as in Figure 5.4 but for the velocity potential (200-1000) hPa of no-aerosol vs aerosol ensemble. The contour plot represents the simple difference between the no-aerosol ensemble and aerosol ensemble. The contour interval is $10^6 m^2/s$. The green contour might represent the ascending air motion due to heating and the magenta contour might indicate the descending air motion due to less heating. The data is analyzed between 1995 to 2004.

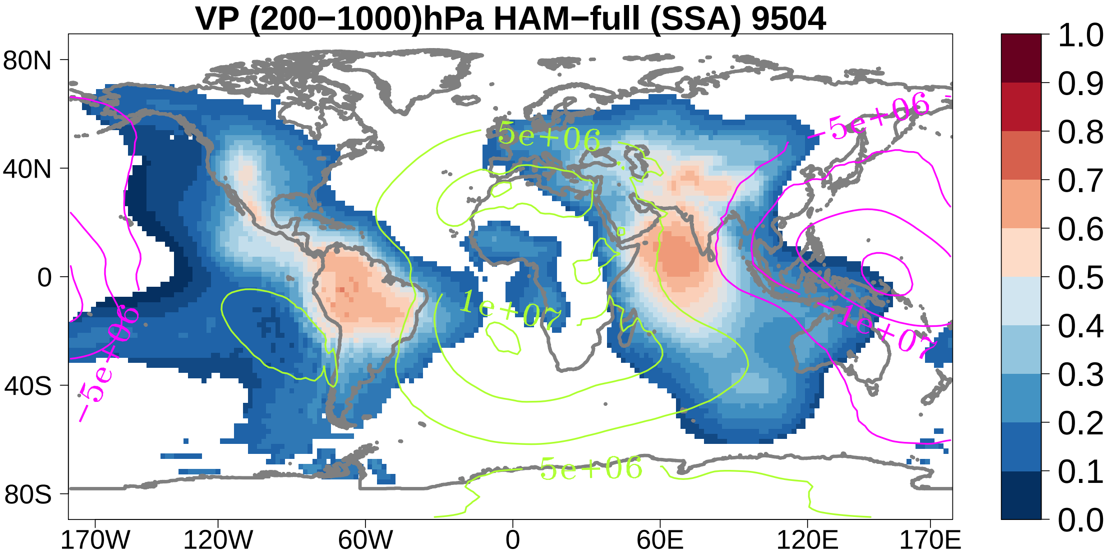

Figure 5.22: It represents the relative change of the pattern of aerosol induced variability from Figure 5.21 to 5.22. It is for aerosol vs HAM-full ensemble. The contour description is same as in Figure 5.21.

(2) aerosol vs HAM-full: The aerosol vs HAM-full case is a test case for the implementation of the BM shown in Figure 5.20. In this case, the mean value of VP (200+1000) hPa for the barotropic mode is greater than the difference value of VP (200-1000) hPa for the faster

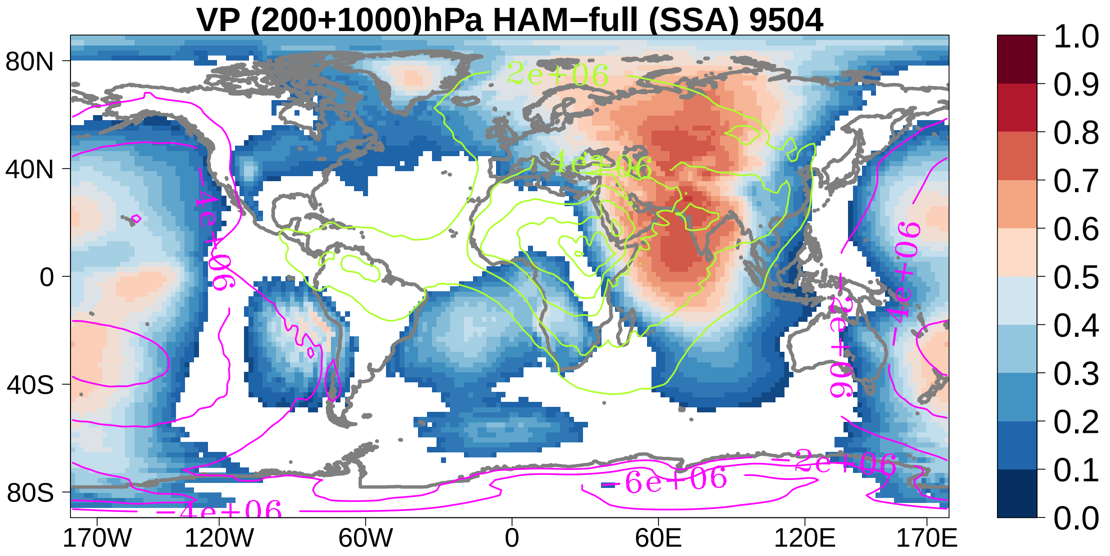

Figure 5.23: It represents the barotropic mode of aerosol vs HAM-full ensemble (200+1000) hPa

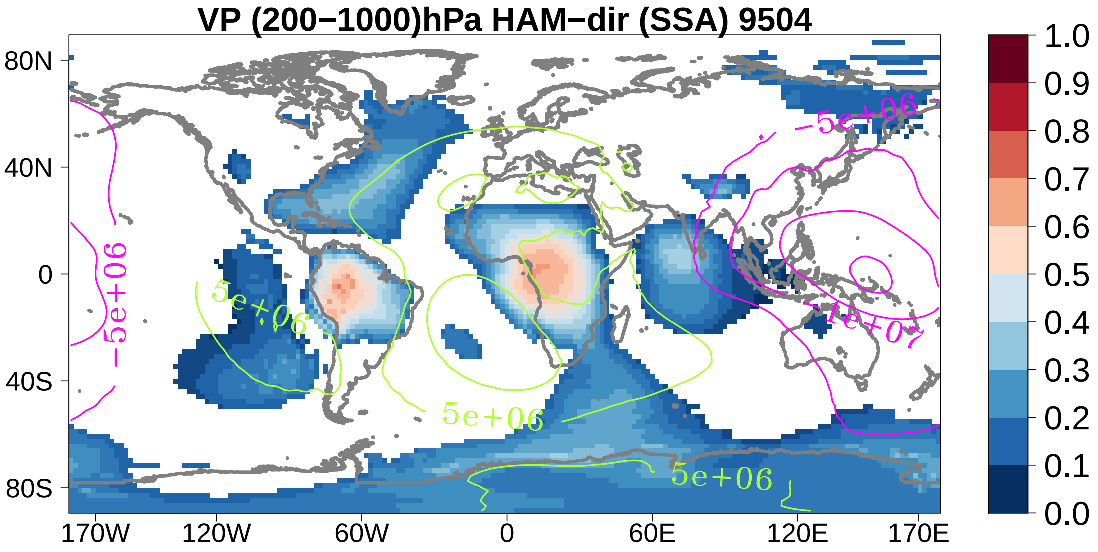

Figure 5.24: It represents the relative change of the pattern of aerosol induced variability from Figure 5.21 to 5.24. It is for aerosol vs HAM-dir ensemble. The contour description is same as in Figure 5.21.

baroclinic mode, it can be seen in Figures 5.22 and 5.23, which means the patterns of the AIV for the VP do not agree with the BM, because the source of the heating in this case is anywhere in the troposphere but not in the middle and hence the atmosphere is not the baroclinic (i.e. no cyclones and anticyclones). In Figure 5.23, the heating signal over Asia is pointing out towards a good barotropic signal. A barotropic atmosphere does have the homogeneous troposphere with no fronts and no thermal advection. The BM will be accepted only when the mean value would be less than the difference value over FBM and the heating source will be in between 200 and 1000 hPa.

In aerosol vs HAM-full case, an enhanced patterns of the aerosol heating for the VP is observed especially over the south America, India and Indian ocean, as shown in Figure 5.22. The AIV maxima over these region are estimated between 40 % to 50 % significance level. The AIV for the mean of VP between the 200 and 1000 hPa further intensified the heating signal over the Asian continent, Indian ocean and a relatively dimmed signal over the Pacific, it can be seen in Figure 5.23. The maxima show 50 % to 70 % significance. The AIV heating signal over the Indian ocean is statistically significant in both cases. The aerosol projection for the VP do not agree with the faster and slower BM.

(3) aerosol vs HAM-dir: In Figure 5.24, the AIV for the VP of HAM-dir ensemble is within the range of 40 % to 50 % over the south of America and Africa but no signal over the India. It means the aerosol scheme used in HAM-dir case possibly reduced the heating signal over the India. The contour description for all plots are same i.e. descending motion due to less heating over Pacific and ascending motion over tropical land areas due to heating.

5.2.3.2 Velocity potential for faster baroclinic mode due to SST induced variability

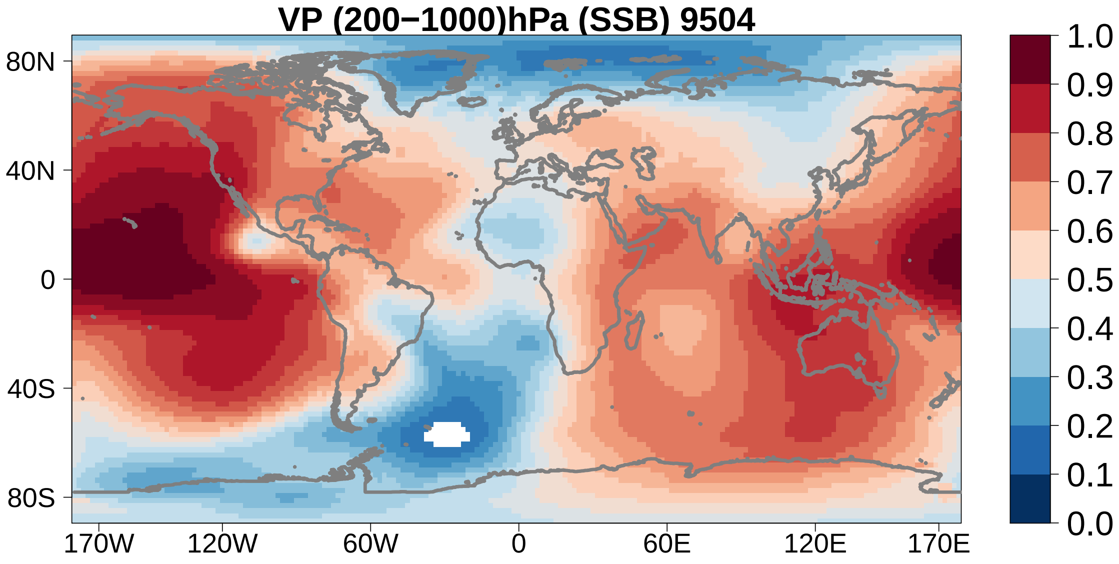

Figure 5.25: Same as in Figure 5.10 but for the velocity potential (200-1000) hPa. It is the part of the no-aerosol vs aerosol ensemble.

(1) no-aerosol vs aerosol: The convection in the atmosphere is a key process for the atmosphere dynamics. Convection over the tropical ocean can be affected by SIV. The SST heat source in the middle of the atmosphere generates the low level convergence and upward vertical motion (Sabin *et al.* 2013).

The SIV for the VP of ECHAM6 ensemble is shown in Figure 5.25. The strong SST projection over the Pacific and Indian ocean is due to the deep response of SST heating over these regions. The portion of this variability is estimated between 60 % to 80 % significant. In the current setup, the SIV has potential to enhance the convection patterns.

(2) aerosol vs HAM-full: The intensity and frequency of the signal became weaker when the SIV for the VP data is analyzed with the aerosol vs HAM-full ensemble, it can be seen in Figure 5.26. The SST projection in this case is related to the the weak convection due to less

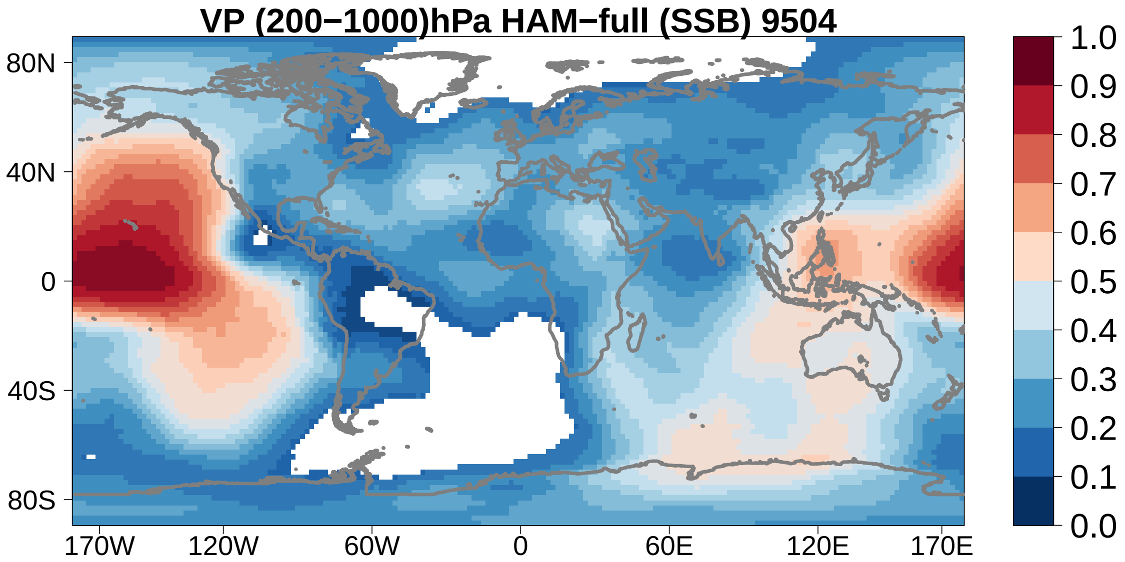

Figure 5.26: It represents the relative change of the pattern of SST induced variability from Figure 5.25 to Figure 5.26. It is for aerosol vs HAM-full ensemble.

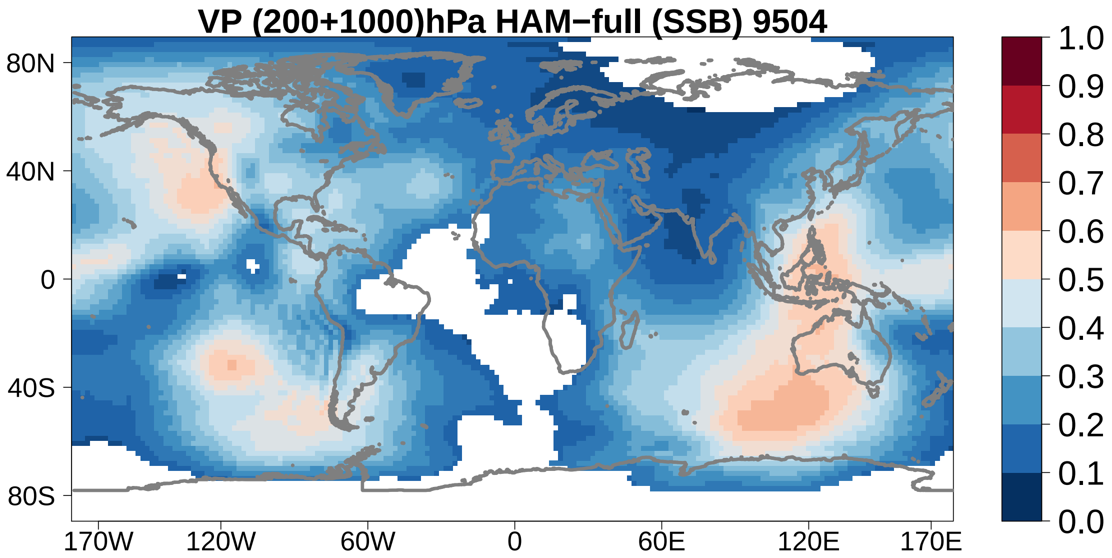

Figure 5.27: It represents the barotropic mode of aerosol vs HAM-full ensemble (200+1000) hPa.

heating in the FBM compared to no-aerosol vs aerosol ensemble, the maxima of this variability are estimated as 50 % to 70 % significant over the Pacific, Indonesia and Philippines. The mean value of SIV out of velocity potential for the barotropic mode is damped down compared to the difference value of SIV, it can be seen by comparing Figure 5.26 with Figure 5.27. Therefore, it is concluded that the BM in Figure 5.20 can be implemented only to the SIV but not to the AIV. The source of heating due to the SST induced variability is situated in the middle of the atmosphere and it has ability to generate cyclones and anticyclones. The SIV heating signal is 30 % to 50 % significant and it is projected over Indonesia, Philippines, Indian ocean and Pacific.

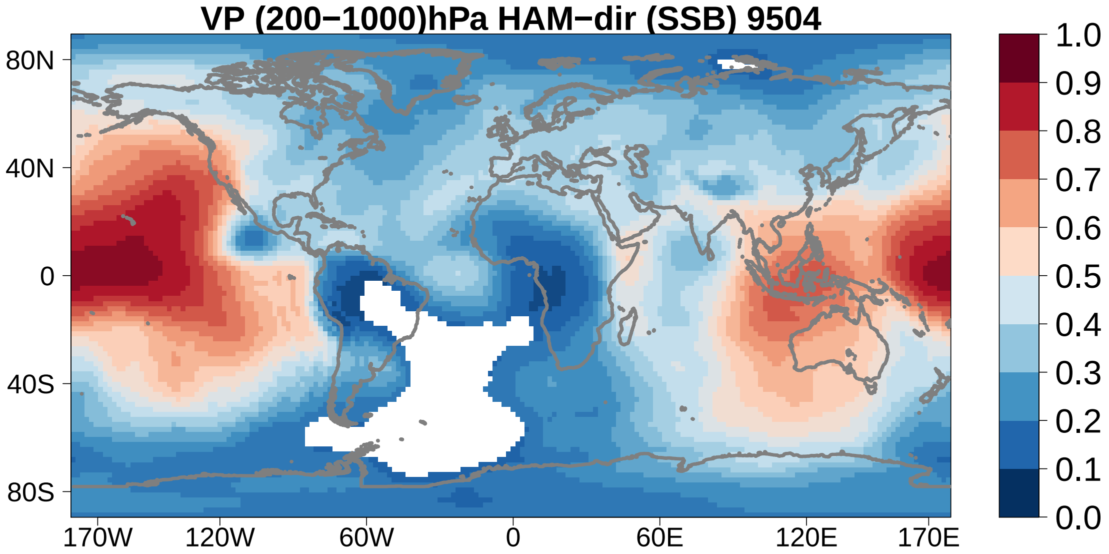

Figure 5.28: It represents the relative change of the pattern of SST induced variability from Figure 5.25 to Figure 5.28. It is for aerosol vs HAM-dir ensemble.

(3) aerosol vs HAM-dir: The change in the relative contribution of the HAM-dir SIV compared to the Figure 5.25 is shown in Figure 5.28. The aerosol vs HAM-dir case has spatial resemblance with the aerosol vs HAM-full case, except over the Indonesia, Philippines and Malaysia. It might be linked with the cyclones activity in those regions.

Graham, Barnett 1987 proposed that the SST and atmospheric convection over the tropical Indian, Pacific and Atlantic oceans are associated with the major climate events. They explained that the convection events normally occur at the SST of about 28 °C in many locations of the Pacific and Indian ocean. More than this SST value (28 °C), a deep convection can be occurred and below this value of SST (28 °C), convection does not occur.

5.2.3.3 Velocity potential for slower baroclinic mode due to aerosol induced variability

(1) no-aerosol vs aerosol: The AIV for the VP of no-areosol vs aerosol ensemble is shown in Figure 5.29. The maxima in this case are associated with the shallow response of the heating due to aerosol variability. A reasonable AIV signal is assessed in the lower troposphere and the range of the projection show significance between 30 % to 40 % for the central Africa.

(2) aerosol vs HAM-full and (3) aerosol vs HAM-dir: The AIV for the VP of HAM-model can be seen in Figures 5.30 and 5.31. A marginal shallow response of heating for the VP of HAM-full ensemble is observed over the American continent, Greenland, north of Africa and Australia as shown in Figure 5.30. The projection of the variability is estimated between 30 % to 50 % over these regions. A reasonable projection of heating for the VP of HAM-dir is recorded over the American continent, Africa, Indian ocean and Australia as shown in Figure 5.31. The projection of AIV in aerosol vs HAM-dir case covers large spatial area compared to no-aerosol vs aerosol and aerosol vs HAM-full ensemble. The portion of this variability is estimated between 30 % to 50 % significance.

The shallow and deep AIV heating response exhibited a reasonable signal for the aerosol vs HAM-model ensemble.

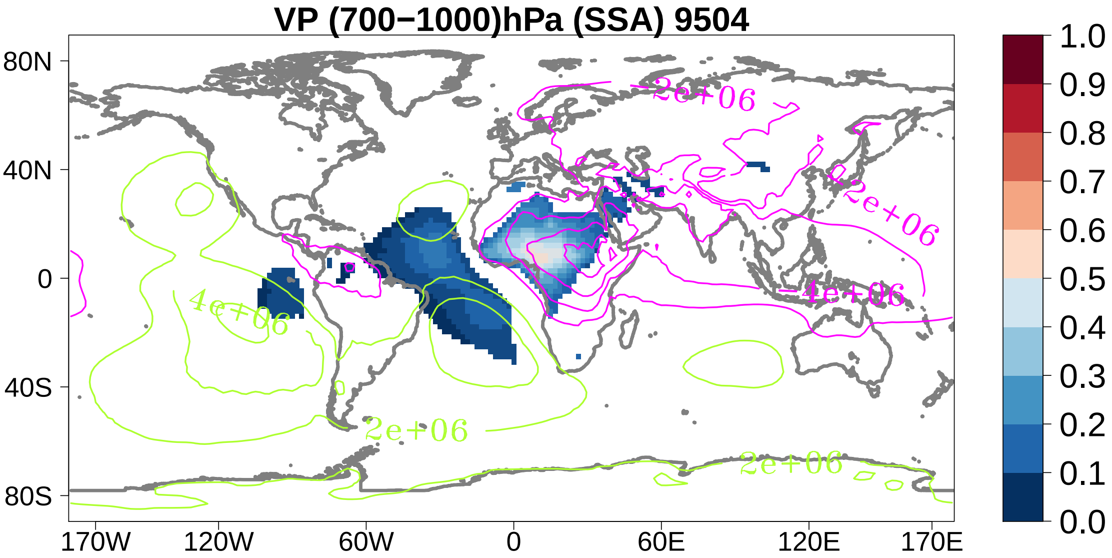

Figure 5.29: Same as in Figure 5.4 but for the velocity potential (700-1000) hPa of no-aerosol vs aerosol ensemble. The contour description is same as in Figure 5.21.

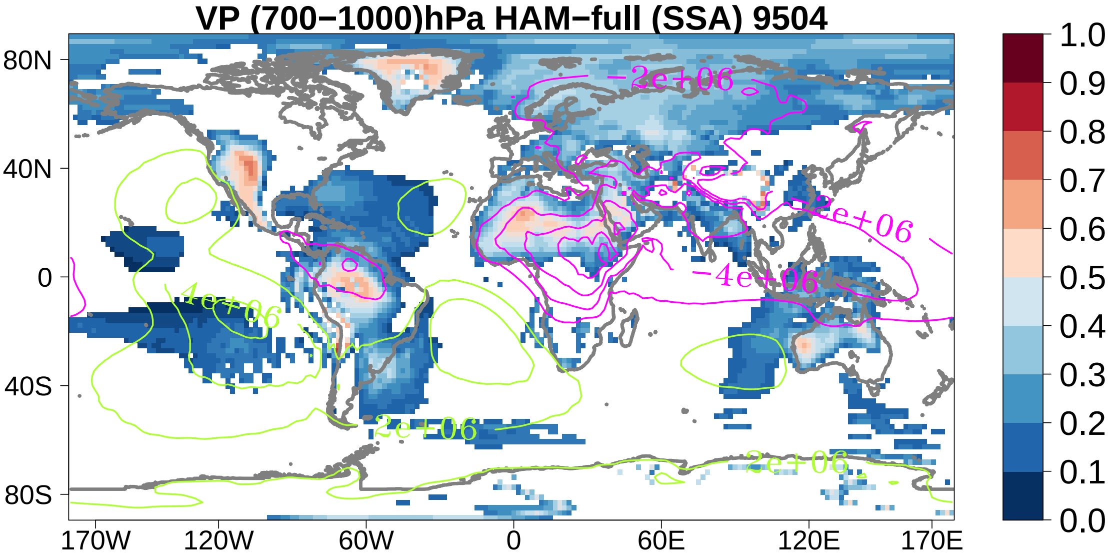

Figure 5.30: It represents the relative change of the pattern of aerosol induced variability from Figure 5.29 to 5.30. It is for aerosol vs HAM-full ensemble. The contour description is same as in Figure 5.29.

5.2.3.4 Velocity potential for slower baroclinic mode due to SST induced variability

(1) no-aerosol vs aerosol: The SIV for the VP of no-aerosol vs aerosol ensemble captured a good SST signal in the lower troposphere, it can be seen in Figure 5.32. A good SST signal in the lower troposphere can be seen here and The maxima in this case is related to the shallow convection due the SST heating over the central Pacific, American continent and Indian ocean. For this case, the aerosol projection is estimated between 50 % to 70 % significant over the

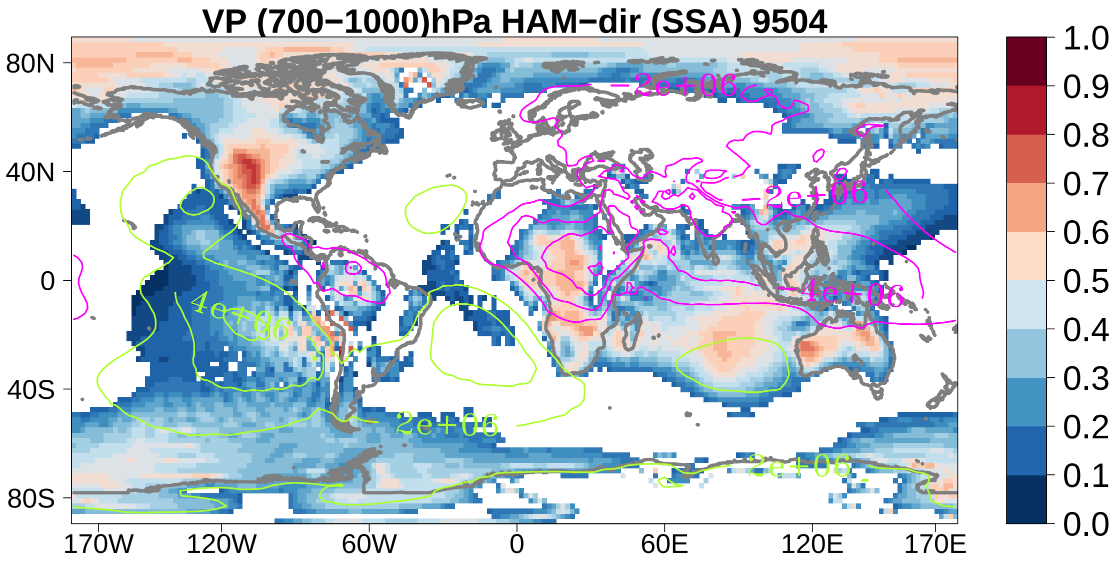

Figure 5.31: It represents the relative change of the pattern of aerosol induced variability from Figure 5.29 to 5.31. It is for aerosol vs HAM-full ensemble. The contour description is same as in Figure 5.29.

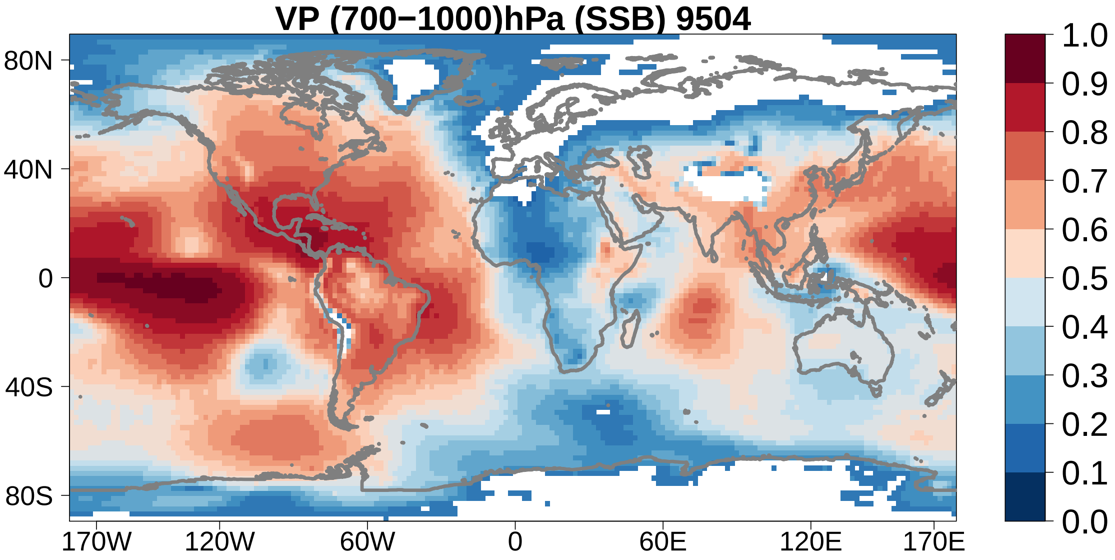

Figure 5.32: Same as in Figure 5.10 but for the velocity potential (700-1000) hPa. It is the part of the no-aerosol vs aerosol ensemble.

central Pacific and American continent and it is recorded between 30 % to 40 % significant over the Indian ocean.

(2) aerosol vs HAM-full and (3) aerosol vs HAM-dir: The patterns of SIV for the HAM-model cases are quite similar, as shown in Figures 5.33 and 5.34. However, in the lower atmospheric layers the SST variability does show a reasonable trend in case of HAM-model ensemble. However, most of variability in this case is induced by the upper atmospheric layers. The intensity of the SIV maxima are decreased and SIV heating reduced the convection for

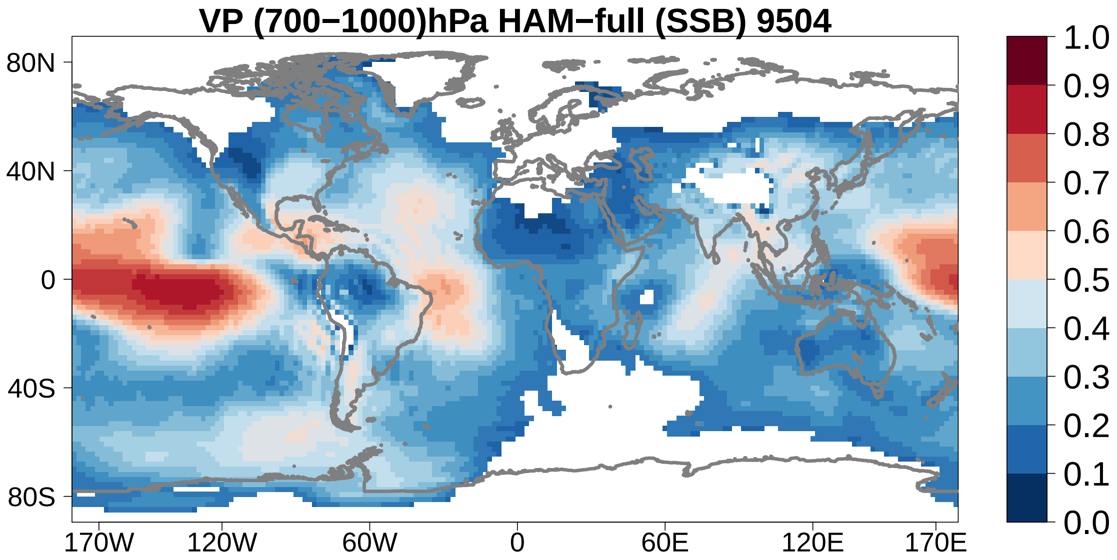

Figure 5.33: It represents the relative change of the pattern of SST induced variability from Figure 5.32 to Figure 5.33. It is for aerosol vs HAM-full ensemble.

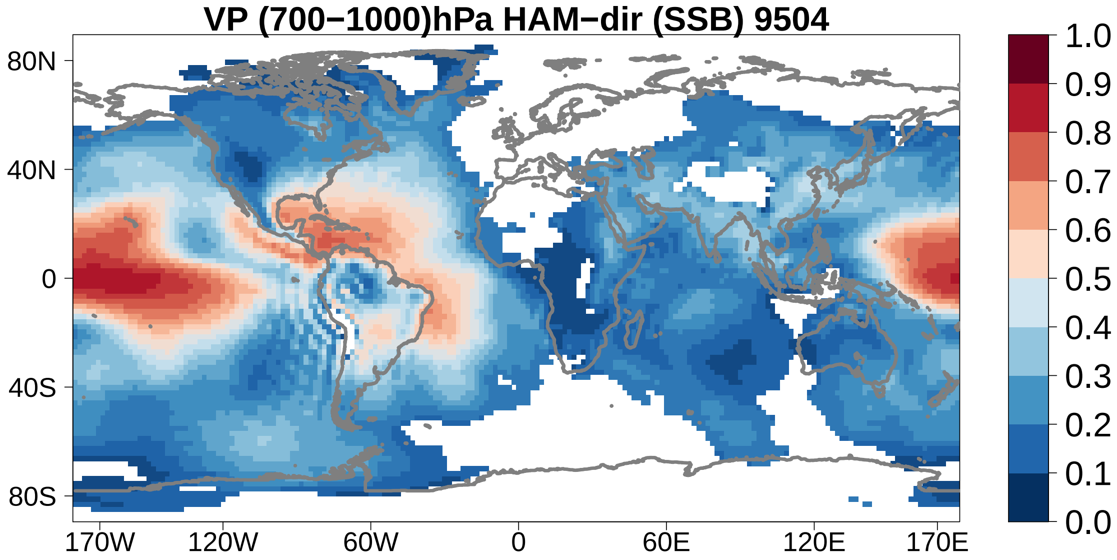

Figure 5.34: It represents the relative change of the pattern of SST induced variability from Figure 5.32 to Figure 5.34. It is for aerosol vs HAM-dir ensemble.

both of the HAM-model cases compared to the no-aerosol vs aerosol case. The predictable SIV is assessed around 40 % to 60 % over the central Pacific and American continent. For the velocity potential, the SIV showed the strong maxima for the no-aerosol vs aerosol case both in the shallow and deep atmospheric layers rather than the HAM-model cases. The deep response of heating due to SIV and the convection signal related to this is analyzed for the FBM of the baroclinic model. The SIV signal is strong in this case, however SIV contribution for the SBM of the baroclinic mode cannot be neglected even though the signal became weaker in SBM than the faster baroclinic mode. In contrast to this, the AIV projected a good heating signal for the SBM than the FBM.

For the divergent wind flow or the velocity potential, the shallow and deep response of the SIV is associated to the convection in the atmosphere. In this study, it is not possible to separate out the PW and KW for the VP as stated in the baroclinic model. Jonko *et al.* 2009 briefly explained a method which splits out the PW and KW using the VP, SF and geopotential height data.

5.2.3.5 Velocity potential vertical profile for aerosol, SST and SSI induced variability

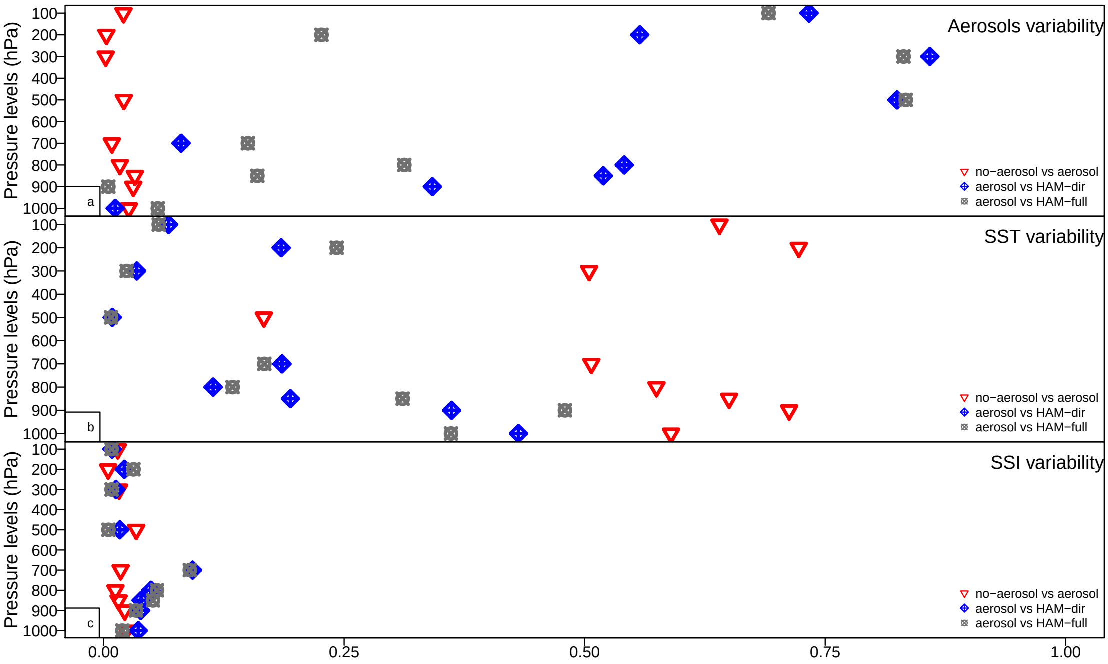

Figure 5.35: Same as in Figure 5.19 but for the velocity potential. (a) The AIV is affecting between 10 % to 15 % the near surface divergence flow field for no-aerosol vs aerosol ensemble, between 10 % to 50 % the near surface divergence flow field and between 25 % to 75 % the middle and upper tropospheric divergence flow field for aerosol vs HAM-full ensemble and between 10 % to 30 % the near surface divergence flow field and between 25 % to 75 % the middle and upper tropospheric divergence flow for aerosol vs HAM-dir ensemble. (b) The SIV is also affecting the divergence flow field between 50 % to 75 % for no-aerosol vs aerosol ensemble, between 10 % to 45 % the divergence flow field for aerosol vs HAM-full ensemble and between 10 % to 50 % the divergence flow field for aerosol vs HAM-dir ensemble (c) The SSI induced variability (SSI) is also not affecting the divergence flow field for all model realizations but it gives unexpected signal for the aerosol vs HAM-model cases between 10 % to 15 %. The data is analyzed between 1995 to 2004.

The AIV is estimated for the VP of no-aerosol vs aerosol ensemble and it can be seen in Figure 5.35, It is approximately zero in this case. The relative contribution of the aerosol variability for HAM-model ensemble are indicating a good signal in the atmosphere.

In contrast to AIV, the SIV for the VP of no-aerosol vs aerosol is playing a major role for the divergence flow in troposphere, as shown in Figure 5.35b. For the HAM-model cases, the SIV did not show a good trend in affecting the VP compared to the ECHAM6 case. The aerosol vs

HAM-full ensemble has less SIV compared to the other two ensemble.

Unexpectedly, the SSI term showed a reasonable signal at 700hPa for the HAM-model. It might be due to the contribution of both aerosol and SST variability. On the map, SSI does not show any variability and hence it is not plotted.

5.2.3.6 Stream function for faster baroclinic mode due to aerosol induced variability

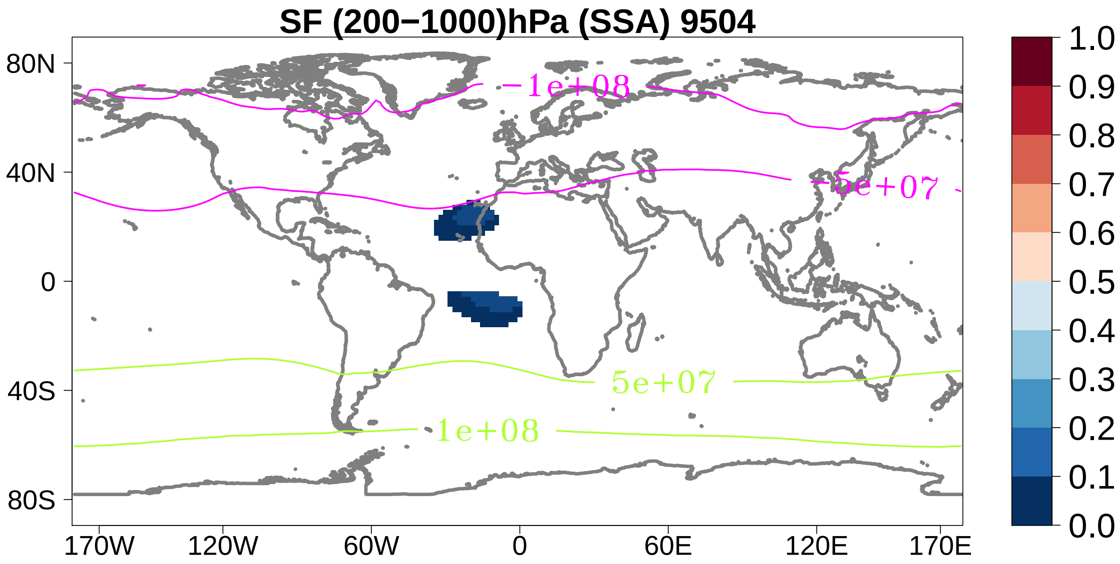

Figure 5.36: Same as in Figure 5.4 but for the stream function (200-1000) hPa of no-aerosol vs aerosol ensemble. The contour values (green and magenta) can cancel each other. The contour plot represents the simple difference between no-aerosol ensemble and aerosol ensemble. The contour interval is $10^6 m^2/s$. The green contours indicate that the PW have downward perturbation the magenta contours indicate that the PW have upward perturbation. The data is analyzed between 1995 to 2004.

(1) no-aerosol vs aerosol: The AIV for stream function of no-aerosol vs aerosol ensemble does not show any patterns in the FBM, as shown in Figure 5.36.

(2) aerosol vs HAM-full An enhanced AIV pattern for the stream function is projected for the HAM-full case and the heating signal due to the aerosol variability is between the range of 10 % to 30 %, as shown in Figure 5.37. The maxima of AIV projection are showing over Africa, Indian ocean and south Pole.

(3) aerosol vs HAM-dir: For the HAM-dir case, a pronounced aerosol heating signal is observed over the north and south America, south of Africa and east of Russia, it can be seen in Figure 5.38. The projection patterns over the America and south of Africa is assessed between 40 % to 50 % and over the east of Russia the AIV is between 50 % to 60 % significant. The presence of aerosol over these regions is affecting the rotational flow. The interpretation of the contour is same as it is stated in Figure 5.36.

For the FBM, an ehanced heating signal for the deep response of AIV is detected for the HAM-model ensemble.

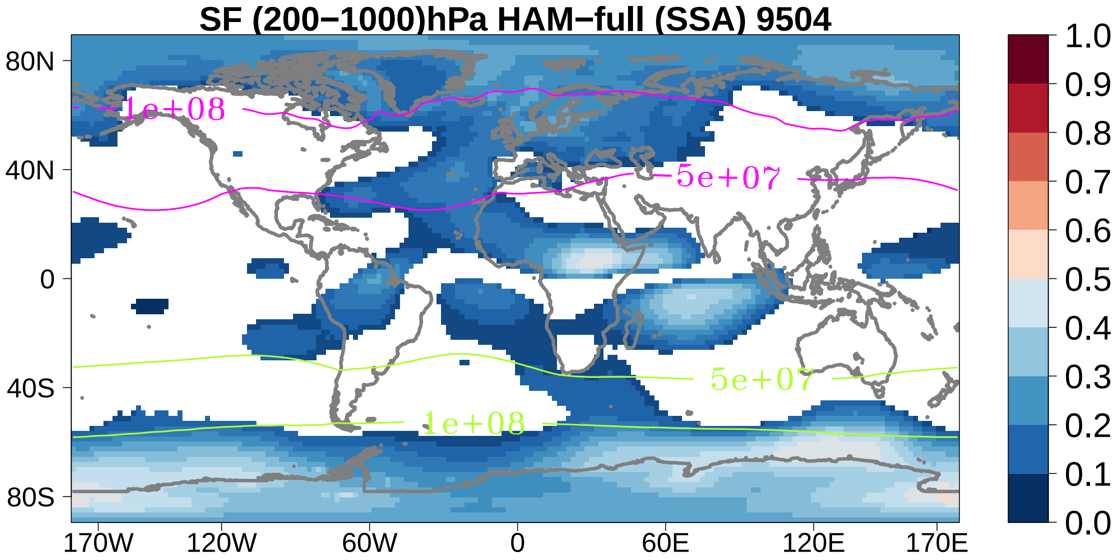

Figure 5.37: It represents the relative change of the pattern of aerosol induced variability from Figure 5.36 to 5.37. It is for aerosol vs HAM-full ensemble. The contour description is same as in Figure 5.36

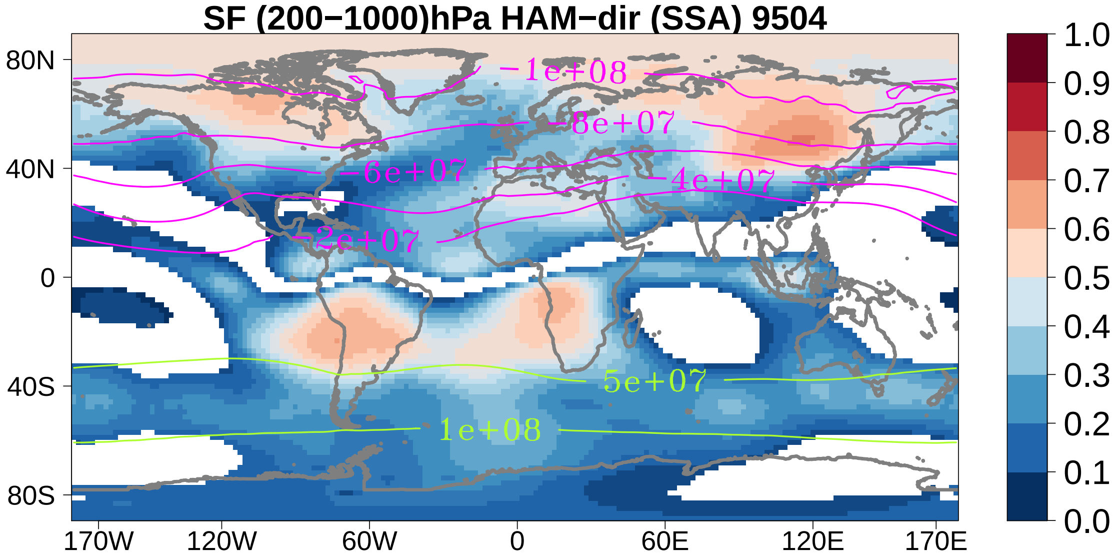

Figure 5.38: It represents the relative change of the pattern of aerosol induced variability from Figure 5.36 to 5.38. It is for aerosol vs HAM-full ensemble. The contour description is same as in Figure 5.36

5.2.3.7 Stream function for faster baroclinic mode due to SST induced variability

(1) no-aerosol vs aerosol: The SIV for the SF of no-aerosol vs aerosol ensemble depicts a deep SST response or significant enhancement of the SST signal in the FBM. In this case, it is possible to show the patterns of PW and KW for the SF, as shown in Figure 5.39. The divergence flow dominates near the equator, it has been seen in Figure 5.25. The green contour over the

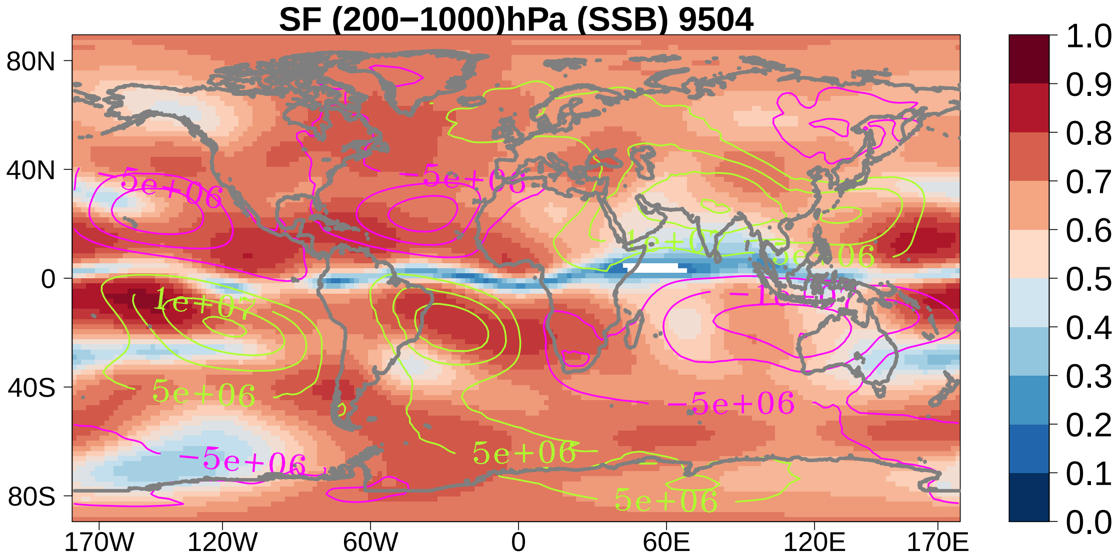

Figure 5.39: Same as in Figure 5.10 but for the stream function (200-1000) hPa. It is the part of the no-aerosol vs aerosol ensemble. The contour interval is $10^6 m^2/s$ and it is showing the propagation of PW and KW in tropics and sub-tropics. The contours basically represents the zonal mean anomaly of SF i.e. When the zonal mean of SF is subtracted from the SF data. The green contours pointed out the anticyclones activity in tropics for aerosol ensemble and the the magenta contours pointed out the cyclones activity in tropics for no-aerosol ensemble. This plot also shows the coupling of the tropical PW and KW with the high latitudes.

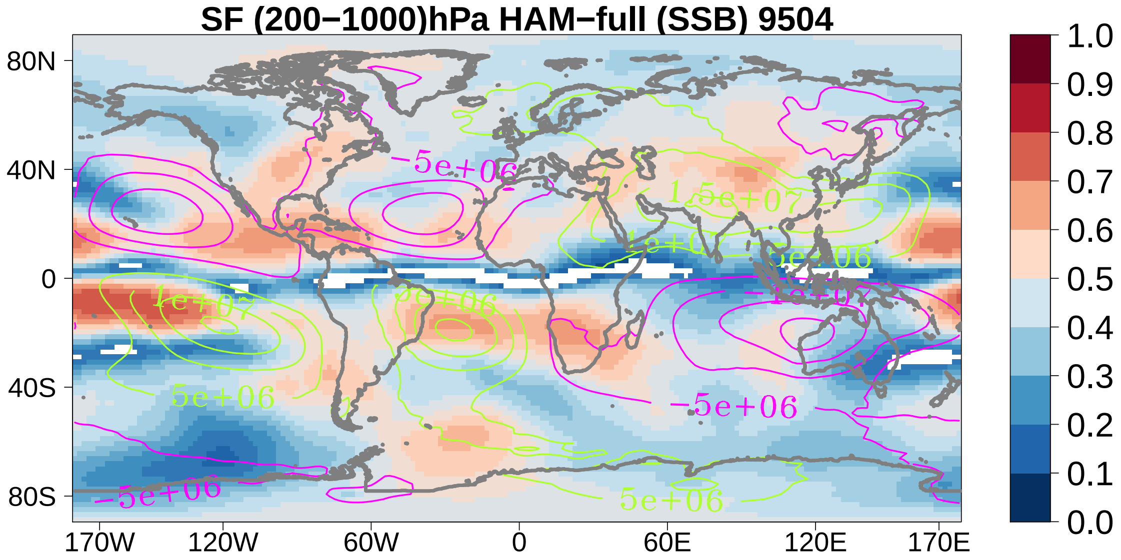

Figure 5.40: It represents the relative change of the pattern of SST induced variability from Figure 5.39 to Figure 5.40. It is for aerosol vs HAM-full ensemble. The contour description is same as in Figure 5.39

Eurasian region clearly indicate the propagation of the PW towards the west-side and the KW to the east-side and their coupling with the high latitudes. The magenta contours represents

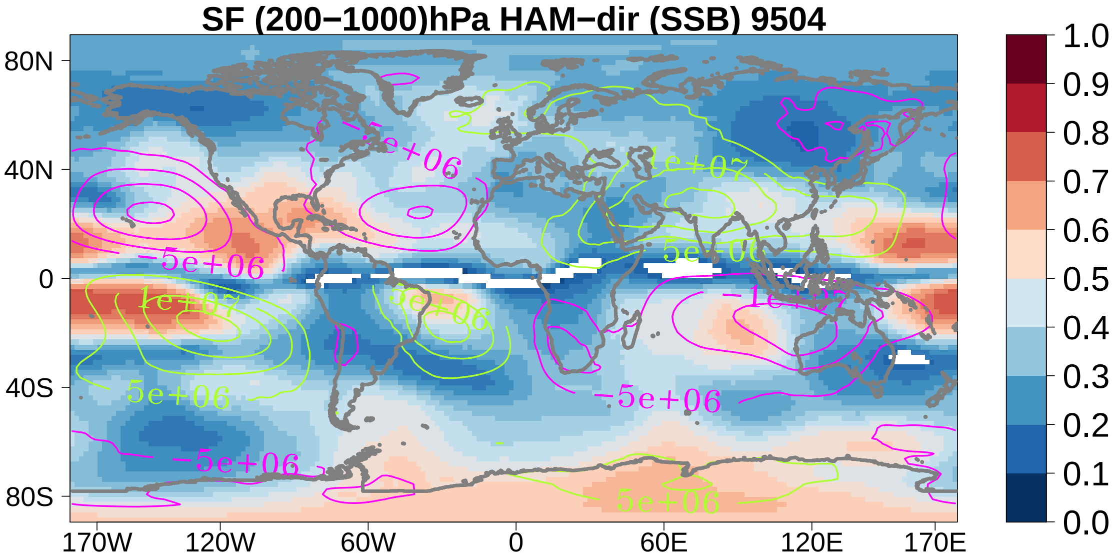

Figure 5.41: It represents the relative change of the pattern of SST induced variability from Figure 5.39 to Figure 5.41. It is for aerosol vs HAM-dir ensemble. The contour description is same as in Figure 5.39

the cyclones activity in the tropics. The SIV in this case is observed between the range of 40 % to 70 % significance. The SST variability is responsible for the heating of the atmosphere.

(2) aerosol vs HAM-full and (3) aerosol vs HAM-dir: These patterns of the SIV is damped down when the SIV for the stream function is analyzed using aerosol vs HAM-model, as shown in Figures 5.40 and 5.41. The SIV in HAM-model cases is estimated within the range of 40 % to 50 %. For the FBM, the divergent flow field or the velocity potential plays an important role for heating the atmosphere and enhancing the convection instead of the rotational flow field.

5.2.3.8 Stream function for slower baroclinic mode due to aerosol induced variability

(1) no-aerosol vs aerosol: For the no-aerosol vs aerosol ensemble, the AIV of the SF is estimated between 30 % to 50 % significance, it is shown in Figure 5.42.

(2) aerosol vs HAM-full and (3) aerosol vs HAM-dir: For the aerosol vs HAM-full case in Figure 5.43, the patterns of heating over tropics and mid-latitude areas are within the range of 40 % to 60 %. The maxima of the heating due to the AIV over the west Africa and Caribbean sea are between 40 % to 50 % significance in case of aerosol vs HAM-dir ensemble, as shown in Figure 5.44. The contours interpretation is same as it has been described in Figure 5.36.

For the slower baroclinic mode, the predicted portion of heating due to AIV is well captured for the aerosol vs HAM-full case as compared to no-aerosol vs aerosol and aerosol vs HAM-dir ensemble.

5.2.3.9 Stream function for slower baroclinic mode due to SST induced variability

(1) no-aerosol vs aerosol: The SIV for the rotational flow of no-aerosol vs aerosol ensemble shows a good SST signal in Figure 5.45. Most of the variability is concentrated over the Pacific ocean and the maxima of this variability are between 50 % to 60 % significance.

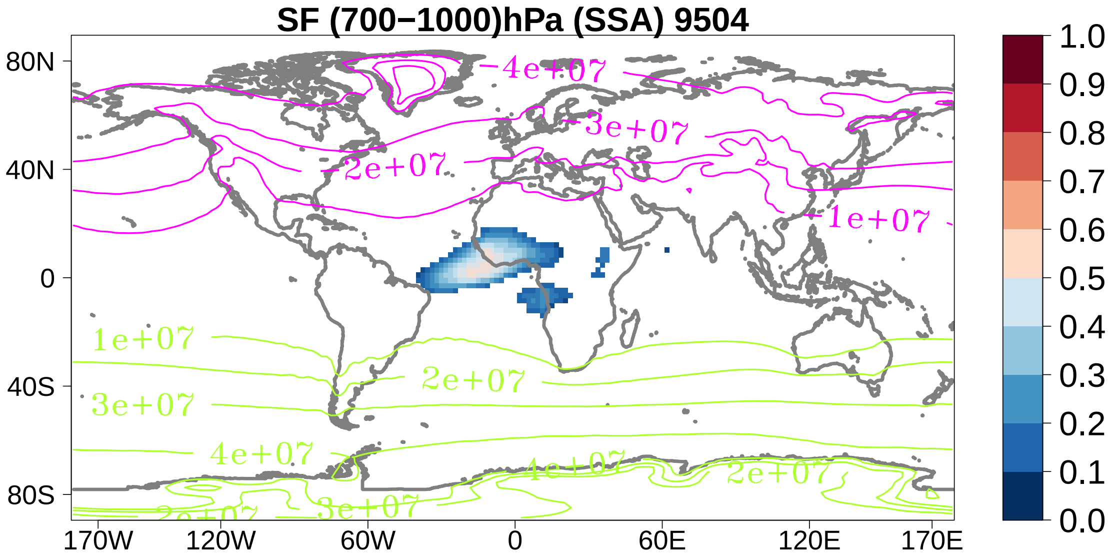

Figure 5.42: Same as in Figure 5.36 but for the stream function (700-1000) hPa of no-aerosol vs aerosol ensemble. The contour description is same as in Figure 5.36.

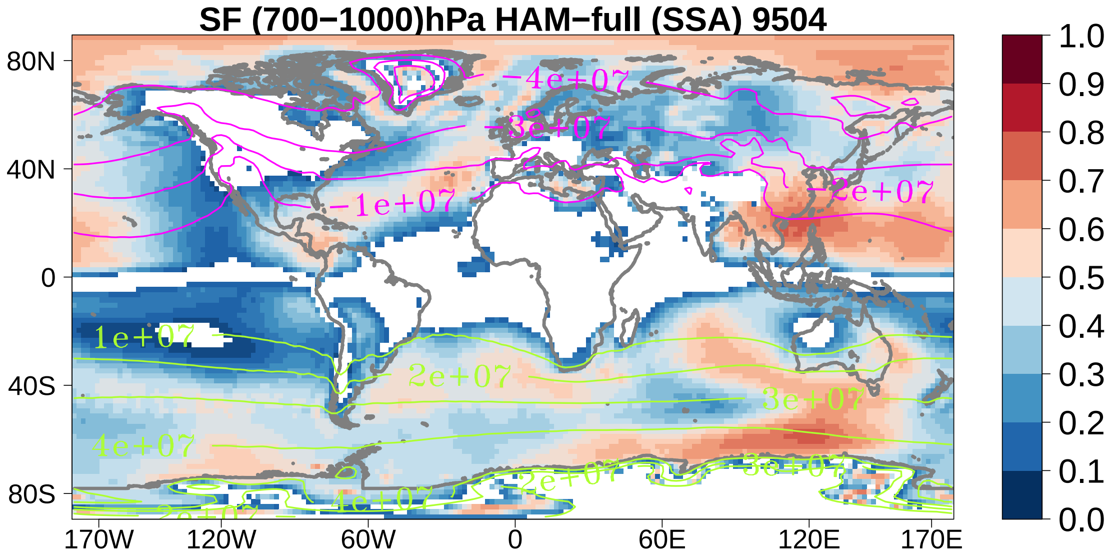

Figure 5.43: It represents the relative change of the pattern of aerosol induced variability from Figure 5.42 to 5.43. It is for aerosol vs HAM-full ensemble. The contour description is same as in Figure 5.42.

(2) aerosol vs HAM-full and (3) aerosol vs HAM-dir: For the HAM-full case, the rotational flow field depicts a weaker shallow response due to the SIV heating. The signal due to this heating is between 30 % to 40 % significant, as shown in Figure 5.46. Spatially the maxima are decreased and SIV heating signal became damped in this case. In Figure 5.47 for the aerosol vs HAM-dir case, the SST signal for the rotational flow field showed some strength compared to aerosol vs HAM-full rotational flow field. The detectable SST projection is mostly over the Pacific and it is within the range of 30 % to 50 % significant.

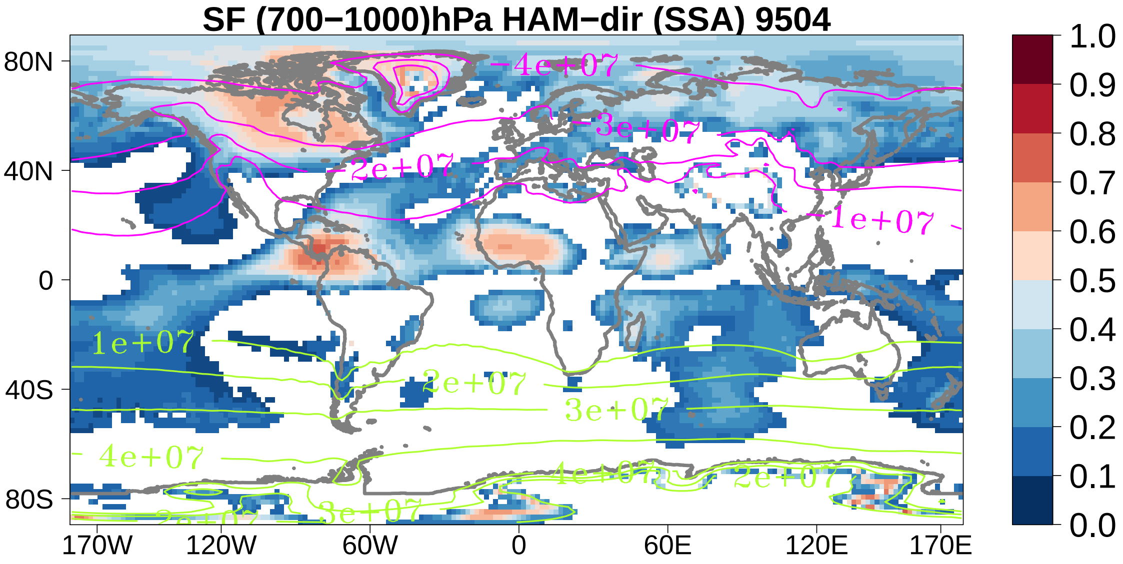

Figure 5.44: It represents the relative change of the pattern of aerosol induced variability from Figure 5.42 to 5.44. It is for aerosol vs HAM-full ensemble. The contour description is same as in Figure 5.42.

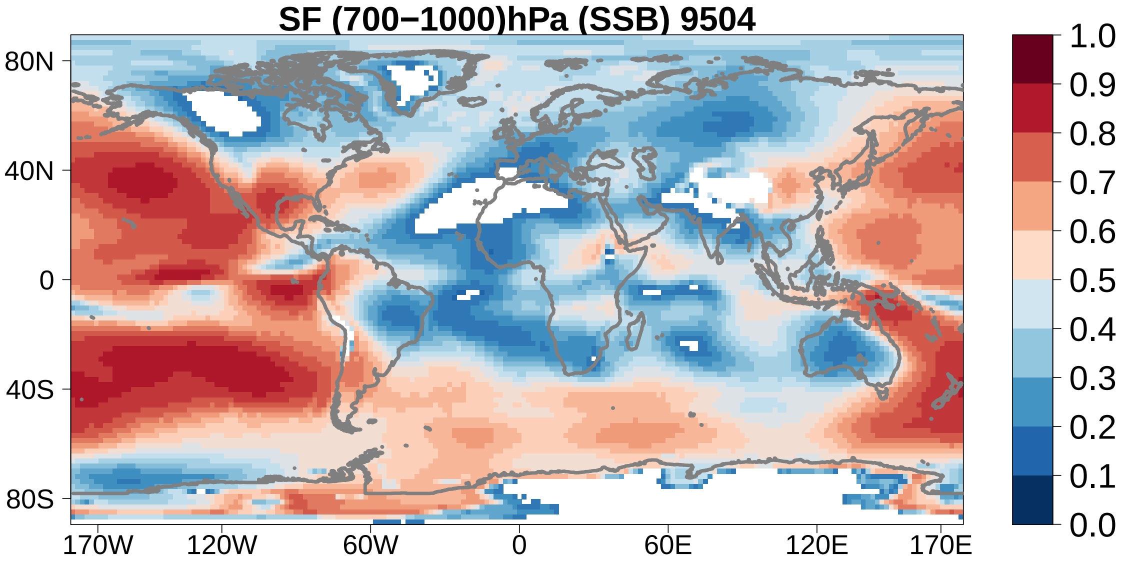

Figure 5.45: Same as in Figure 5.39 but for ECHAM6 ensemble.

For the rotational flow field, the SIV in the FBM played an important role compared to the AIV. The HAM-dir ensemble showed a pronounced signal for the AIV. In the shallow layer, the SIV projected a distinct signal especially over the Pacific in no-aerosol vs aerosol compared to the aerosol vs HAM-model cases. The AIV for aerosol vs HAM-full in SBM accounted a good signal. Overall, the SST contribution for the rotational flow field is greater than the AIV. The results of large scale circulation showed a significant contribution of SIV for the VP compared to the SF, in the FBM and SBM.

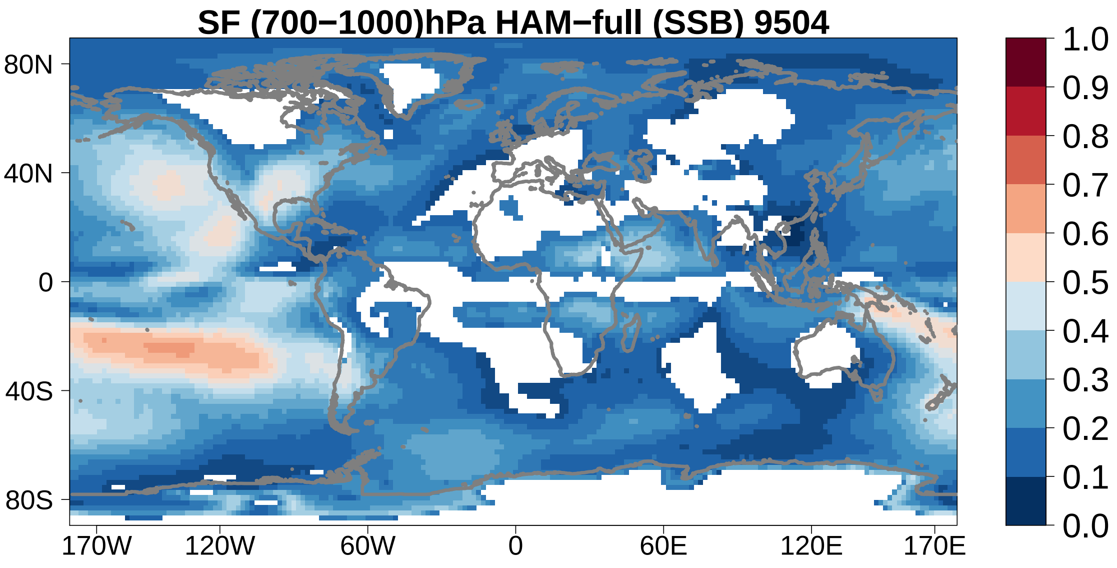

Figure 5.46: Same as in Figure 5.39 but for HAM-full ensemble.

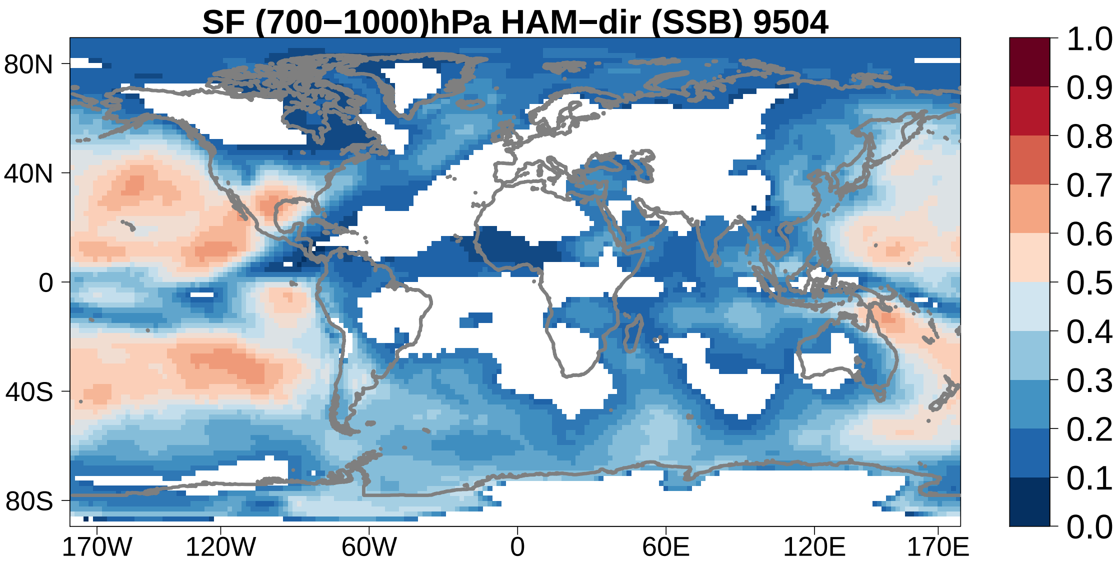

Figure 5.47: Same as in Figure 5.39 but for HAM-dir ensemble.

5.2.3.10 Stream function vertical profile for aerosol, SST and SSI variability

The AIV for the SF of no-aerosol vs aerosol ensemble is shown in Figure 5.48. For this case, the aerosol variability is estimated as zero for the rotational flow field. Upon comparing the divergence flow in Figure 5.35 with vertical profile of rotational flow, it is observed that the AIV for aerosol vs HAM-model ensemble is decreased from 75 % of divergence flow to 25 % of rotational flow in the atmosphere. The SST variability for all model cases play a dominant role in estimating the rotational flow field. The SSI variability did not show any reasonable trend here.

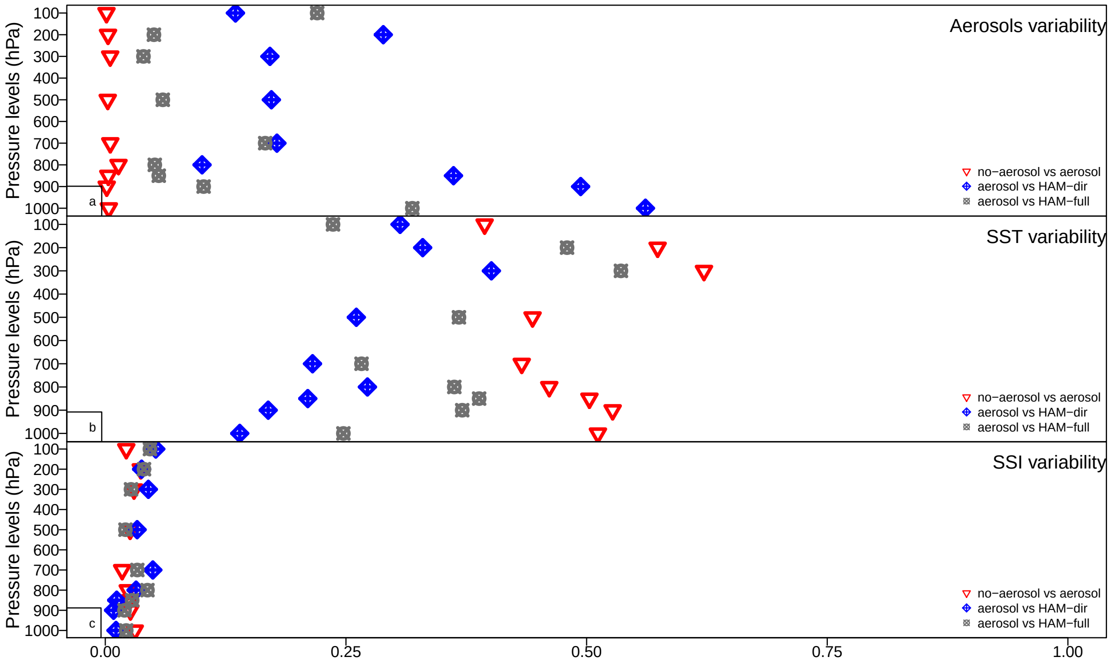

Figure 5.48: Same as in Figure 5.19 but for the stream function. (a) The AIV or SSA is accounted almost nothing for the rotational flow fields for no-aerosol vs aerosol ensemble, between 10 % to 50 % the near surface rotational flow field and between 20 % to 25 % the middle and upper tropospheric rotational flow field for aerosol vs HAM-full ensemble and between 5 % to 30 % the near surface rotational flow field and between 5 % to 25 % the middle and upper tropospheric rotational flow for aerosol vs HAM-dir ensemble (b) The SIV or SSB is also accounted the rotational flow field between 40 % to 60 % for no-aerosol vs aerosol ensemble, between 15 % to 45 % the rotational flow field for aerosol vs HAM-full ensemble and between 25 % to 50 % the rotational flow field for aerosol vs HAM-dir ensemble (c) SSI induced variability (SSI) is not affecting the rotational flow field for all model realizations. The data is analyzed between 1995 to 2004.

6 Physical reasoning of ANOVA

In Chapter 5, the response of the predictable variance of aerosol and SST variability showed the projection mostly over tropics. It is expected that the variability shown in two-way ANOVA can lead to real time climate forecast. For this, a dynamical response of either SSI or SIV should show a good trend. The static effect of AIV is not varying over time therefore it is not possible to show a forecast signal for it. The dynamical response of SIV can possibly interpret into a forecast signal, because it already showed the reasonable projection in previous chapter. The SSI variability is also a dynamical response quantity however there is not such a evidence that the SSI played a good role in two-way ANOVA. It will be interesting to check again the response of this quantity by using regression and correlation coefficients method, described in Chapter 4.

6.0.4 Correlation coefficients of African AOD and global 2m temperature

The time series of African AOD is correlated with the global 2m temperature, it is shown in Figures 6.1, 6.2 and 6.3. These three patterns represent the transient variability of SSI. However, it is accounted as zero for all model variables when analyzed by the two-way ANOVA, this has been discussed earlier in Section 5.2. Three cases of correlation coefficients differ from each other in the description of the different aerosol schemes (i.e. ECHAM6, HAM-full and HAM-dir). It is confirmed now that there exists no correlation between AOD and 2m temperature because no reliable signal is captured for all three cases.

In Figure 6.1, the variation in correlation coefficients between AOD and 2m temperature show the values greater than 0.5. The spread of the patterns is quite ambiguous, because no strong correlation exists over Africa. This is the region where a AOD time series is correlated along the global 2m temperature. The maxima over other regions instead of Africa are due to the random signal of the two quantities. It is more clear in Figures 6.2 and 6.3 that there is not such a good relationship between these two variables. Therefore, no real climate forecast is possible for the SSI case.

6.0.5 Correlation coefficients of central Pacific SST and global 2m temperature

A good connection is established between the central Pacific SST and global 2m temperature, as shown in Figures 6.4, 6.5 and 6.6. Using two-way ANOVA, the SST variability detected the similar patterns for the 2m temperature as it has been shown in Figures 5.10, 5.11 and 5.12. Both the ANOVA and correlation patterns cannot be exactly same because ANOVA is based on two ensemble and it gives the projection of the variability and the correlation coefficients method explains the dynamics behind that variability.

The correlation between the SST and 2m temperature over Pacific and Indian ocean shows some significant projection, as shown in Figure 6.4. Over these region the value of the correlation coefficient is greater than 0.5. A strong correlation occurs over central Pacific where the SST times series is correlated with the 2m temperature. In case of HAM-model, the strength of the correlation signal is weakened compared to ECHAM6 ensemble, it can be seen in Figures

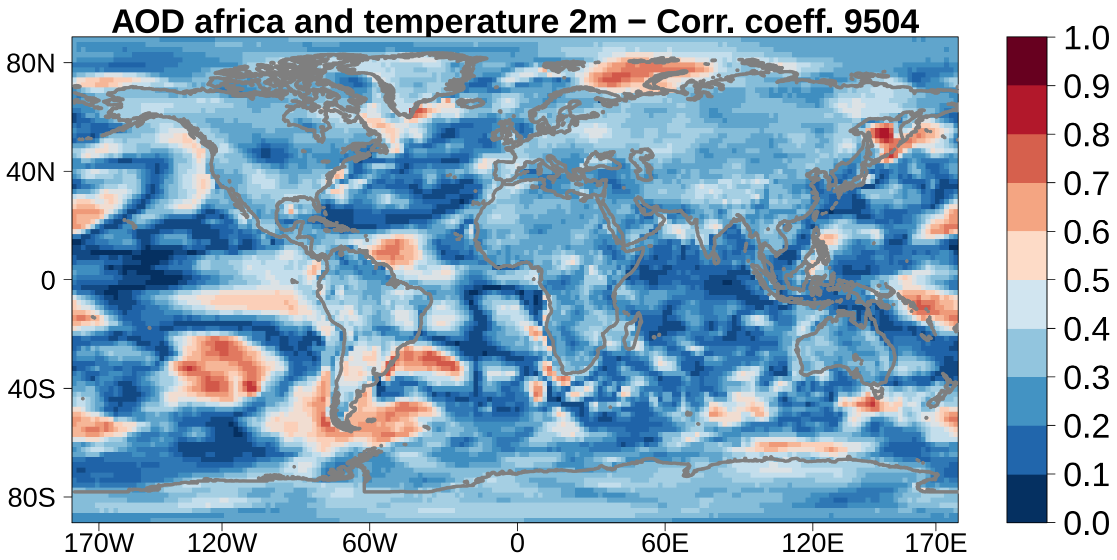

Figure 6.1: A correlation between the time series of AOD over Africa and global 2m temperature of aerosol ensemble is investigated to see either both of these quantities have any connection with each others or not. This plot is made by using four different methods: (1) An area with Kinne AOD over Africa is selected and the residual (Chapter 4: Regression and correlation coefficient) from the regression model are computed for both the AOD Africa and the global 2m temperature. (2) The time series of AOD Africa is computed and the intercept between the time series and global 2m temperature is estimated. (3) The sum of square and sum of errors of AOD Africa and global 2m temperature are computed using the deviance function (i.e. for sum of errors) in R. (4) Finally, the correlation coefficient is obtained by taking the square root of the correlation square. The correlation coefficients are computed for each ensemble separately and at the end these coefficients values are averaged and plotted. It basically represents the SSI variability of two-way ANOVA. The color bar in this plot represents the correlation coefficients values. When the value of correlation coefficients between AOD and 2m temperature is greater than 0.5, this will mean both the data have good correlation with each others. The data is analyzed between 1995 to 2004.

6.5 and 6.6. However, the location of the correlation maxima is still over the Pacific and the Indian ocean.

The 2m temperature is taken as a test case. The projection of SSI and SST variability in two-way ANOVA is physically interpreted by the correlation coefficients method. A real time climatic forecast using current setup is only possible for the Pacific SST variability.

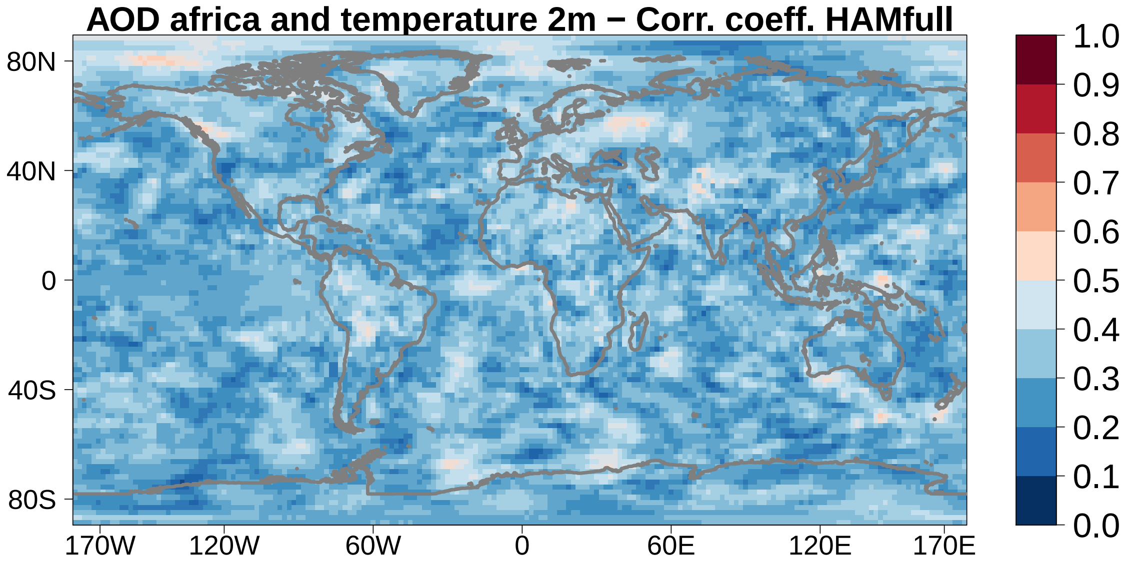

Figure 6.2: Same as in Figure 6.1 but for HAM-full ensemble and HAM-full AOD data is used for this experiment.

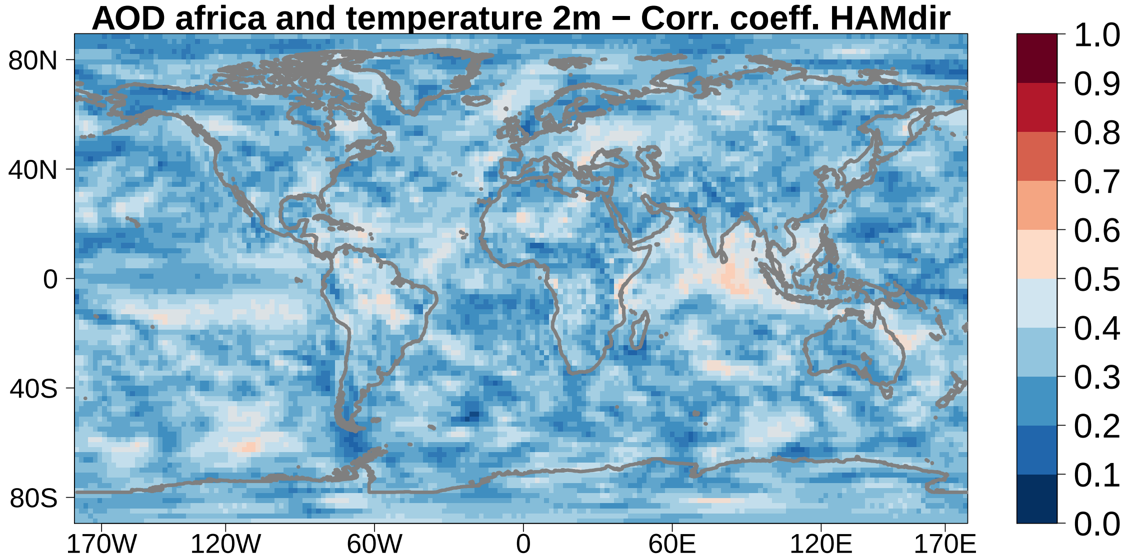

Figure 6.3: Same as Figure 6.1 but for HAM-dir ensemble and HAM-dir AOD data is used for this experiment.

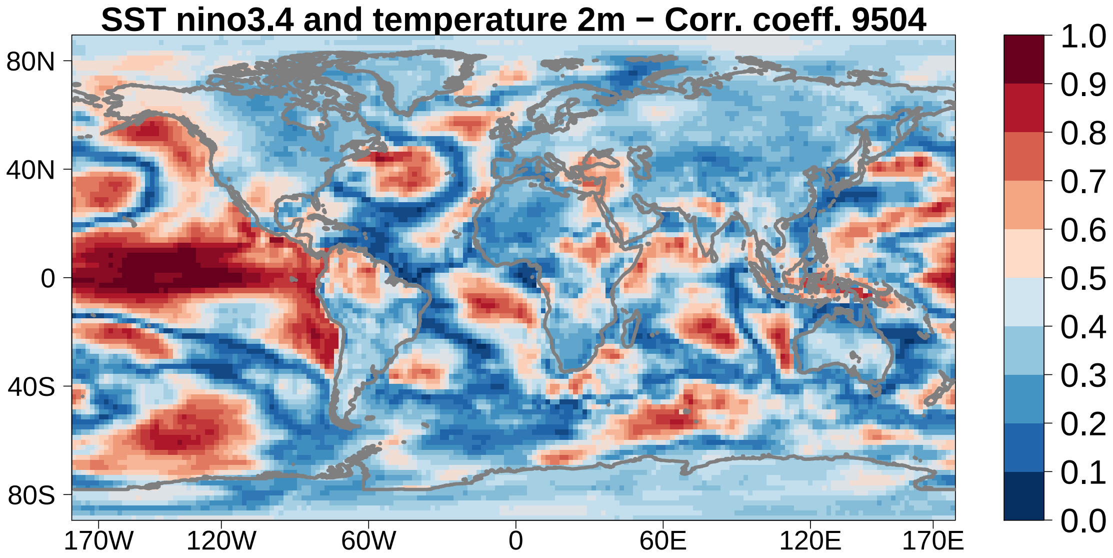

Figure 6.4: Same as in Figure 6.1 but for the central Pacific SST (Hadley center SST data) and 2m temperature of aerosol ensemble.

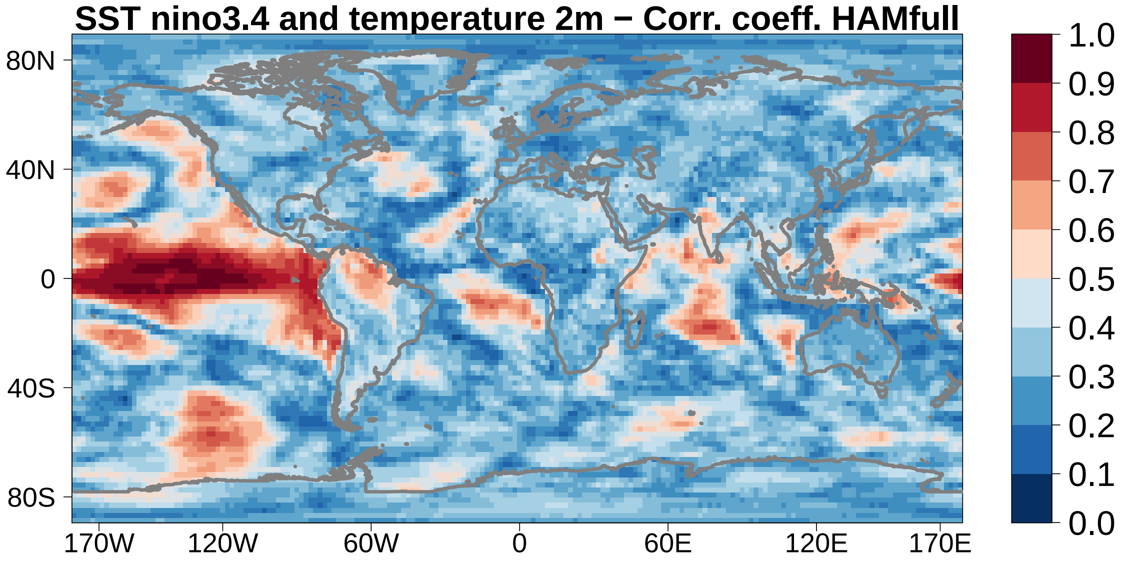

Figure 6.5: Same as in Figure 6.4 but for HAM-full ensemble.

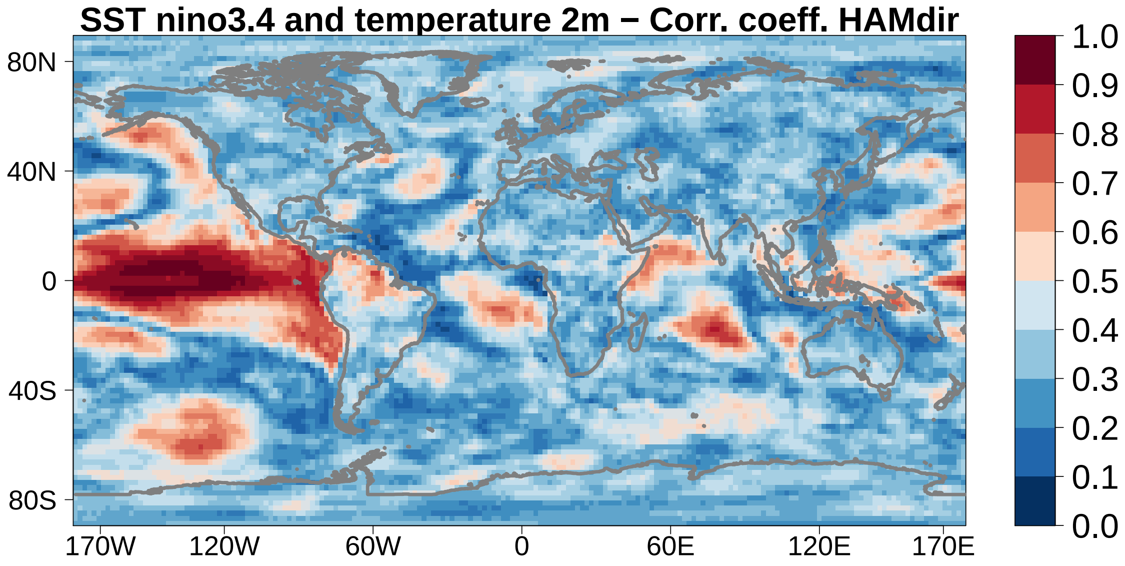

Figure 6.6: Same as in Figure 6.4 but for HAM-dir ensemble.

7 Conclusions

Aerosol and SST climatic effects are satisfactorily understood in this study. The fundamental complexity and global spatio-temporal inhomogeneities in the global aerosol structure makes it difficult to assess the impact of aerosol induced variability (AIV). Traditionally, the microphysical properties like the aerosol composition, mixing state and size distribution have been enormously studied and several different aerosol schemes have been implemented into the GCMs. Only few studies discussed about the statistical significance of global aerosol direct and indirect effect. However, in this study, not only the AIV is statistical quantified and analyzed but also the SST induced variability (SIV). The climate prediction of the greenhouse gases and aerosol in IPCC fifth assessment report is based on 50 to 100 years time scale. This work is a part of MiKlip and therefore the projection of AIV and SIV have been assessed and predicted over a decade.

The global climate model ECHAM6-HAM has been used to estimate such effects of AIV and SIV via four different aerosol treatments and a common SST forcing. With the atmospheric component of ECHAM6-HAM, the prescribed SST data has been used as a supplement to the ocean model. Recent model configuration of ECHAM6-HAM includes sulfate, black carbon, sea salt, particulate organic matters and mineral dust aerosol species. Four ensemble have been created using the different initial conditions derived from the four control runs. These ensemble are based on the different aerosol scheme. The ensemble without any transient additional aerosol concentration is named as the no-aerosol. The time varying aerosol climatological data is used for the aerosol ensemble. For the direct and indirect effect of aerosol, model ECHAM6-HAM is integrated with AEROCOM data and aerosol micro-physics processes are interactively calculated by the HAM model. This case is regarded as the HAM-full ensemble. A similar approach like HAM-full ensemble is used for the assessment of the HAM-dir ensemble but the model simulated only the aerosol direct effect in this case. The model data for ECHAM6 and ECHAM6-HAM captured well the maxima of dust aerosol over west Africa, the anthropogenic aerosol of north India and industrial aerosol plume in the east of China.

Two different satellite products like SRB, GPCP were used for the validation of the model output. Furthermore, model data was compared with the evaporation data of ERA-Interim. The aerosol increased the planetary albedo from 0.29 (no-aerosol) to the 0.3 for the aerosol case. The highest values of PA is observed for the HAM-full ensemble 0.325 and lowest is found for the HAM-dir 0.225. For TOA radiation balance, the HAM-dir case exhibits the global and annual mean imbalance of 21 W·m^{-2}, whereas all other cases (i.e. no-aerosol, aerosol and HAM-full) are closer to the radiative balance when averaged over the ten years 1995-2004. For the further validation, the simulated results are compared to the SRB data and the water balance components precipitation from GPCP and evaporation from the ERA-Interim. The comparison between the radiative energy balance shows that the offset of the planetary radiative balance in HAM-dir case by 21 W·m^{-2} has almost no effect upon the radiative balance of the atmosphere being still at a loss of about 103 W·m^{-2} but it is transferred directly to the surface radiative balance. This imbalance in TOA radiative energy balance also did not show any effect upon the evapotranspiration or latent heat fluxes which are close to 3 (mm/day) in all experiments. In case, when this 21 W·m^{-2} imbalance will be balanced completely by evapotranspiration, it will correspond to 0.7 (mm/day) but the differences among the runs and observations are only between 0.1 to 0.2 (mm/day).

The uncertainties are further investigated in the zonal mean plots. For the TREB, the equator and tropics received more SW energy compared to the mid-latitude and poles. The values of the difference between the model and observations are within the uncertainty range which means the data is statistically significant. A large amount of energy is radiated from equator and tropics in SREB case. The atmospheric aerosol absorbs energy in AREB case.

The basic aim of this work is to advance the understanding about the global tropospheric AIV and SIV using ANOVA technique. The one-way ANOVA has been used to find a connection between the AOD and SIV. Unfortunately, there exists no relationship between the AOD and SIV. All projected SIV is over central Pacific which might indicate to a SST signal. Most of the AIV in AREB cases has been recorded over the tropics and sub-tropics. This AIV belongs to the absorbing aerosol of Brazil, Africa, Arabian peninsula and the north of India. The results show that the direct effect of prescribed and interactive aerosol are clearly detectable (especially for the aerosol vs HAM-dir) even on a regional scale on the decadal time scale when the atmospheric radiative fluxes are analyzed. The energy which has been absorbed by aerosol in AREB case, potentially changed the thermodynamical structure of the atmosphere (i.e. temperature). The projection of AIV for the 2m temperature (temperature-2m) has indicated a heating near surface. This heating is affected by the SIV and to a less extent by the AIV. The ECHAM6-HAM is not coupled to the ocean model and it utilized the prescribed SST data, as stated earlier. This might be the reason that the model simulated such a good SIV signal for temperature-2m. Both the AIV and SIV are damped down for the temperature-850hPa. However, the SIV has still predicted a reasonable maxima when compared to AIV. In the tropics, the change in temperature has modified the divergence flow or velocity potential (VP). In the faster baroclinic mode (FBM), a reasonable aerosol heating signal for the VP has been detected mainly over south America. The heating due to AIV for the large scale circulation did not fit well to the baroclinic model (BM) and it mainly represented the barotropic atmosphere. In contrast to this, the heating signal in the FBM due to the SIV agrees with the BM and is related to the convection in tropics. In the slower baroclinic mode (SBM), the signal of the AIV and SIV for VP is reduced compared to the FBM of AIV and SIV, but heating due SIV has potential to affect the VP. The divergence flow is coupled to the rotational flow field or stream function (SF). The BM has been implemented to the SF. In the FBM, a weak maxima of AIV for the SF is projected over the south America and Africa. The projection of SIV has been observed over the tropics. The heating due to SIV in FBM instigated the Kelvin wave and planetary wave, these waves pointed out the different cyclones and anticyclones activity near tropics. For the SBM, the AIV and SIV did not show a reasonable maxima but again the SIV has shown a reasonable trend than the AIV.

The AIV and SIV in ANOVA are further analyzed for the real time forecast. In the first case, the AIV over Africa has been correlated with the global temperature-2m and no reasonable signal is detected over Africa. This means that no climatic forecast is possible for the AIV. However, the correlation coefficient for the central Pacific SST and temperature-2m predicted a good signal in Pacific which means that SIV has potential to do the real time forecast especially for the Pacific region.

It has been explained in detail that the ECHAM6-HAM is capable to simulate the significant characteristics of the global aerosol. The analysis of variance of radiative fluxes, temperature and dynamical variables on times scales of 10 years show that aerosol effects (direct and indirect) could be important for the longer leads of decadal climate forecasts. In this study, it was found that without an ocean model and using the prescribed SST data, the model has potential to perform a real time climate forecast for the SIV specially over the Pacific.

Acknowledgements

My thanks go first to my supervisors Dr. Andreas Bott and Dr. Andreas Hense for their constant support, for their inspirational way of teaching and for the interesting project they involved me. Their positive spirit in the Miklip project made my aerosols work funfull. Their personalities are source of knowledge for me.

I pay thank to Meteorlogisches Institut Universität Bonn Germany for giving me the oppurtunity and good environment to perform this research. The support of Federal Ministry of Education and Research (BMBF) is greatly acknowledged, as they fully supported the one of the big German decadal climate project MiKlip i.e. BMBF program MiKlip project AODA-peng (funding code: 01LP1157A).

My sincere thanks go to all my colleagues, in particular Benno Thoma, Elke Rustemeier, Lilo Bach, Chris Weijenborg, Sophie Stolzenberger, Dr. Elham Rehmani, Dr. Pablo Saavedra Garfias, Dr. Xinxin Xie, Mohammad Reza, Ehsan Khorsandi, Dr. Sabrina Wahl, Dr. Jan Keller, Alex Kelbach, Dr. Volker Küll, Dr. Michael Weniger, Christoph Beekmans, Werner Schneider, Marcus Übel, Ms. Annemarie Debus, Ms. Ingeborg Rassow, Dr. Rita Glowienka-Hense, Ms. Lucia Hallas, Rüdiger Hewer, Sebastian Knist, Marc Mertes, Ieda Pscheidt, Dr. Vanya Romanova, Nils Weitzel, Dr. Thorsten Simon and David Willms.

Registers and Bibliography

Bibliography

Aaron, D., Battisti, D. S. (2011). Atmospheric and Surface Contributions to Planetary Albedo. *J. Climate* **24**: 4402–4418.

Adam, J. C., Clark, E. A., Lettenmaier, D. P., Wood, E. F. (2006). Correction of global precipitation products for orographic effects. *J. Climate* **19**: 15–38.

Adams, P. J., Seinfeld, J. H. (2002). Predicting global aerosol size distributions in general circulation models. *J. Geophys. Res. Atmos.* **107**: 1–23.

Adler, R. F., Gu, G., Huffman, G. J. (2012). Estimating Climatological Bias Errors for the Global Precipitation Climatology Project (GPCP). *J. Appl. Meteor. Climatol.* **51**: 84–99.

Adler, R. F., Huffman, G. J., Chang, A., Ferraro, R., Xie, P., Janowiak, J., Rudolf, B., Schneider, U., Curtis, S., Bolvin, D., Gruber, A., Susskind, J., Arkin, P., Nelkin, E. (2003). The Version-2 Global Precipitation Climatology Project (GPCP) Monthly Precipitation Analysis (1979-Present). *J. Hydrometeor.* **4**: 1147–1167. ISSN: 1525-755X.

Aoki, K. (2006). Aerosol optical characteristics in Asia from measurements of SKYNET sky radiometers, in IRS 2004: Current Problems in Atmospheric Radiation. *Hampton, VA*, 311–313.

Ardanuy, P. E., Kyle, H. L., Hoyt, D. (1992). Global relationships among the earth's radiation budget, cloudiness, volcanic aerosols and surface temperature. *J. Climate* **5**: 1120–1139.

Ayash, T., Gong, S., Jia, C. Q. (2007). Direct and Indirect Shortwave Radiative Effects of Sea Salt Aerosols. *J. Climate* **21**: 3207–3220.

Babu, S. S., Moorthy, K. K., Manchanda, R. K., Sinha, P. R., Satheesh, S. K., Vajja, D. P., Srinivasan, S., Kumar, V. H. A. (2011). Free tropospheric black carbon aerosol measurements using high altitude balloon: Do BC layers build "their own homes" up in the atmosphere? *Geophys. Res. Lett.* **38**: 1–6.

Baines, P. G., Palmer, T. N. (1990). Rationale for a new physically-based parameterization of subgridscale orographic effects. *Tech. Rep.* **169**: 1–11.

Baumgardner, D., Popovicheva, O., Allan, J., Bernardoni, V., Cao, J., Cavalli, F., Cozic, J., Diapouli, E. (2012). Soot reference materials for instrument calibration and intercomparisons: A workshop summary with recommendations. *Atmos. Meas. Tech.* **5**: 1869–1887.

Bender, F. A.-M., Rodhe, H., Charlson, R. J., Ekman, A. M. L., Loeb, N. (2006). 22 views of the global albedo–Comparison between 20 GCMs and two satellites. *Tellus* **58**:3, 320–330.

Bloom, S., Silva, A. d., Dee, D. (2005). Documentation and validation of the Goddard Earth Observing System (GEOS) Data Assimilation System–Version 4. *Tech. Rep.* **26**: 1–165.

Bond, T., Streets, D. G., Yarber, K. F., Nelson, S. M., Woo, J.-H., Klimont, Z. (2004). A technology-based global inventory of black and organic carbon emissions from combustion. *J. Geophys. Res.* **109**: 1–43.

Bony, S., Colman, R., Kattsov, V. M., Allan, R. P., Bretherton, C. S., Dufresne, J.-L., Hall, A., Hallegatte, S., Holland, M. M., Ingram, W., Randall, D. A., Soden, B. J., Tselioudis, G., Webb, M. J. (2006). How well do we understand climate change feedback processes? *J. Climate* **19**: 3445–3482.

Bony, S., Dufresne, J.-L., Treut, H. L., Morcrette, J.-J., Senior, C. (2004). On dynamic and thermodynamic components of cloud changes. *Clim. Dyn.* **22**: 71–86.

Brasseur, G. P., Prinn, R. G., Pszenny, A. A. (2006). Atmospheric Chemistry in a Changing World. *Springer-Verlag*, 300 pp.

Brinkop, S., Roeckner, E. (1995). Sensitivity of a general circulation model to parameterizations of cloud-turbulence interactions in the atmospheric boundary layer. *Tellus* **47**: 197–220.

Budyko, M. I. (1969). The effect of solar radiation variations on the climate of the Earth. *Tellus* **21**: 611–619.

Buizza, R., Palmer, T. (1995). The singular-vector structure of the atmospheric global circulation. *J. Atmos. Sci.* **52**: 1434–1456.

Chand, D., Wood, R., Anderson, T. L., Satheesh, S. K., Charlson, R. J. (2009). Satellite-derived direct radiative effect of aerosols dependent on cloud cover. *Nat. Geosci.* **2**: 181–184.

Chang, L. S., Park, S. U. (2004). Direct radiative forcing due to anthropogenic aerosols in East Asia during April 2001. *Atmos. Environ.* **38**: 4467–4482.

Chapman, W. L., Welch, W. J., Bowman, K. P., Sacks, J., Walsh, J. E. (1994). Arctic sea ice variability: Model sensitivities and a multidecadal simulation. *J. Geophys.Res. Oceans* **99**: 919–935.

Charlson, R. J., Schwartz, S. E., Hales, J. M., Cess, R. D., Coakley, J. A., Hansen, J. E., Hofmann, D. J. (1992). Climate forcing by anthropogenic aerosols. *Science* **255**: 423–430.

Chuang, C. C., Penner, J. E., Prospero, J. M., Grant, K. E., Rau, G. H., Kawamoto, K. (2002). Cloud susceptibility and the first aerosol indirect forcing: Sensitivity to black carbon and aerosol concentrations. *J. Geophys. Res. Atmos.* **107**: 1–23.

Cionni, I., Eyring, V., Lamarque, J. F., Randel, W. J., Stevenson, D. S., Wu, F., Bodekar, G. E., Shephered, T. G., Shindell, D. T., Waugh, D. W. (2011). Ozone database in support of CMIP5 simulations: results and corresponding radiative forcing. *Atmos. Chem. Phys.* **11**: 11267–11292.

Crawley, M. J. (2013). *The R book*. Vol. Second edition. 1051 pp. Wiley, 449–498.

Del Genio, A. D., Kovari, W. (2002). Climatic properties of tropical precipitating convection under varying environmnetal conditions. *J. Climate* **15**: 2597–2615.

Dentener, F., Kinne, S., Bond, T., Boucher, O., Cofala, J., Generoso, S., Ginoux, P., Gong, S., Hoelzemann, J. J., Ito, A., Marelli, L., Penner, J. E., Putaud, J.-P., Textor, C., Schulz, M., Warf, G. R. v. d., Wilson, J. (2006). Emissions of primary aerosol and precursor gases in the years 2000 and 1750 prescribed data-sets for AeroCom. *Atmos. Chem. Phys.* **6**: 4321–4344.

Eliasen, E., Machenhauer, B., Rasmussen, E. (1970). *On a numerical method for integration of the hydrodynamical equations with a spectral representation of the horizontal fields*. 74 pp. Kobenhavns Universitet, Institut for Teoretisk Meteorologi.

Enderton, D., Marshall, J. (2009). Controls on the total dynamical heat transport of the atmosphere and oceans. *J. Atmos. Sci.* **66**: 1593–1611.

Eyring, V., Cionni, I., Lamarque, J. F., Akiyoshi, H., Bodeker, G. E., Charlton-Perez, A. J., Frith, S. M., Gettelman, A., Kinnison, D. E., Nakamura, T., Oman, L. D., Pawson, S., Yamashita, Y. (2010). Sensitivity of 21st century stratospheric ozone to greenhouse gas scenarios. *Geophys. Res. Lett.* **37**: 1–7.

Fasullo, J. T., Trenberth, K. E. (2008). The annual cycle of the energy budget, part I: Global mean and land–ocean exchanges. *J. Climate* **21**: 2297–2312.

Fasullo, J., Sun, D.-Z. (2001). Radiative sensitivity to water vapor under all-sky conditions. *J. Climate* **14**: 2798–2807.

Feichter, J., Roeckner, E., Lohmann, U., Liepert, E. (2004). Nonlinear aspects of the climate response to greenhouse gas and aerosol forcing. *J. Climate* **17**: 2384–2398.

Feng, J. (2008). A size-resolved model and a four-mode parameterization of dry deposition of atmospheric aerosols. *J. Geophys. Res. Atmos.* **113**: 1–13.

Forster, P., Ramaswamy, V., Artaxo, P., Berntsen, T., Betts, R., Fahey, D., Haywood, J., Lean, J., Lowe, D., Myhre, G., Nganga, J., Prinn, R., Raga, G., Schulz, M., Dorland, R. V. (2007). Changes in Atmospheric Constituents and in Radiative Forcing. In: Climate Change 2007: The Physical Science Basis. Contribution of Working Group I to the Fourth Assessment Report of the Intergovernmental Panel on Climate Change. *Cambridge University Press*, 1–234.

Fröhlich, C., Judith, L. (2004). Solar radiative output and its variability: evidence and mechanisms. *The Astron. Astrophys. Rev.* **12**: 273–320.

Fuchs, N. A. (1959). *Evaporation and droplet growth in gaseous media*. Ed. by R. S. Bradley. 77 pp. Pergamon Press, Oxford, 72.

– (1964). *The mechanics of aerosols*. Vol. 146. 408 pp. American Association for the Advancement of Science.

Fujihara, Y., Yamamoto, Y., Tsujimoto, Y., Sakagami, J.-I. (2014). Discharge simulation in a data-scarce basin using reanalysis and global precipitation data: A case study of the white volta basin. *Journal of Water Resource and Protection* **6**: 1316–1325.

Gill, A. E. (1982). *Atmosphere Ocean dynamics: Chapter Eleven, The Tropics*. 662 pp. Academic press, 429–482.

Giorgetta, M. A., Manzini, E., Roeckner, E., Esch, M., Bengtsson, L. (2006). Climatology and forcing of the quasi-biennial oscillation in the MAECHAM5 model. *J. Climate* **19**: 3882–3901.

Giorgetta, M., Roeckner, E., Mauritsen, T., Stevens, B., Bader, J., Crueger, T., Esch, M., Rast, S., Kornblueh, L., Schmidt, H., Kinne, S., Möbis, B., Krismer, T. (2012). *The atmospheric general circulation model Echam6*. (Model description) 172 pp. Max-Planck Institute for Meteorology Hamburg, Germany.

Gorodetskaya, I. V., Cane, M. A., Tremblay, L.-B., Kaplan, A. (2006). The effects of sea-Ice and land-snow concentrations on planetary albedo from the earth radiation budget experiment. *Atmosphere-Ocean* **44**: 195–205.

Gough, W. A., Welch, W. J. (1994). Parameter space exploration for an ocean general circulation model using isopycnal mixing parameterization. *J. Mar. Res.* **52**: 773–796.

Graham, N. E., Barnett, T. P. (1987). Sea surface temperature, surface wind divergence, and convection over Tropical oceans. *Science* **238**: 657–659.

Granat, L., Rodhe, H., Hallberg, R. O. (1976). The global Sulphur cycle. *Ecol. Bull.* **22**: 89–134.

Granier, C., Artaxo, P., Reeves, C. E. (2004). *Emission Of Atmospheric Trace Compounds, chapter: Sea-salt aerosol source functions and emissions*. Vol. 18. 545 pp. Kluwer Academic Publisher, 333–359.

Gualdi, S., Scoccimarro, E., Navarra, A. (2008). Changes in tropical cyclone activity due to global warming: Results from a high-resolution coupled general circulation model. *J. Climate* **21**: 5204–5228.

Guelle, W., Schulz, M., Balkanski, Y., Dentener, F. (2001). Influence of the source formulation on modeling the atmospheric global distribution of sea salt aerosol. *J. Geophys. Res. Atmos.* **106**: 27, 509–27, 524.

Hagedorn, R., Doblas-Reyes, F. J., Palmer, T. N. (2005). The rationale behind the success of multi-model ensembles in seasonal forecasting-I. Basic concept. *Tellus* **57**: 219–233.

Hagemann, S. (2002). *An improved land surface parameter dataset for global and regional climate models*. 336 21 pp. Max-Planck Institute for Meteorology Hamburg Germany.

He, Q., Li, C., Geng, F., Lei, Y., Li, Y., Tie, X., Yin, Q. (2011). Study on long-term aerosol distribution over the land of East China using MODIS data. *Atmos. Chem. Phys. Discuss.* **11**: 10, 485–10, 523.

Hense, A. (2005). "Observed Global Climate." Ed. by M Hantel. Springer Berlin Heidelberg. Chap. 2 Processing of observational data and its implication for climate analysis, 1–11.

Herman, J. R., Bhartia, P. K., O. Torres, C. H., Seftor, C., Celarier, E. (1997). Global distribution of UV-absorbing aerosols from Nimbus 7/TOMS data. *J. Geophys. Res. Atmos.* **102**: 16, 911–16, 922.

Hollingsworth, A. (1993). Validation and diagnosis of atmospheric models. *Dynam. Atmos. Ocean* **20**: 227–246.

Houghton, J. T., Meira, F., Callander, B., Harris, N., Kattenberg, A. (1996). *Climate Change 1995: The Science of Climate Change*. Tech. rep. 572 pp. Cambridge University Press, 572.

Houtekamer, P., Derome, J. (1995). Methods for ensemble prediction. *Mon. Weather Rev.* **123**: 2181–2196.

Houtekamer, P., Mitchell, H. L. (1998). Data assimilation using an ensemble kalman filter technique. *Mon. Weather Rev.* **126**: 796–811.

Huang, Y., Wu, S., Dubey, M. K., French, N. H. F. (2013). Impact of aging mechanism on model simulated carbonaceous aerosols. *Atmos. Chem. Phys.* **13**: 6329–6343.

Huffman, G. J., Adler, R. F., D. T. Bolvin, G. G. (2009). Improving the Global Precipitation Record: GPCP Version 2.1. *Geophys. Res. Lett.* **36**: 1–5.

Hurrell, J. W., James, J. H., Dennis, S., Julie, M. C., Rosinski, J. (2008). A New Sea Surface Temperature and Sea Ice Boundary Dataset for the Community Atmosphere Model. *J. Climate* **21**: 5145–5153.

Hurtt, G. C., Chini, L. P., Frolking, S., Betts, R. A., Feddema, J., Fischer, G., Fisk, J. P., Hibbard, K., Houghton, R. A., Janetos, A., Jones, C. D., Kindermann, G., Kinoshita, T., Goldewijk, K. K., Riahi, K., Shevliakova, E., Smith, S. (2011). Harmonization of land-use scenarios for the period 1500-2100: 600 years of global gridded annual land-use transitions, wood harvest, and resulting secondary lands. *Clim. Chang.* **109**: 117–161.

IPCC (2001). *The Scientific Basis. Contribution of Working Group I to the Third Assessment Report of the Intergovernmental Panel on Climate Change*. Tech. rep. Cambridge University Press, 881 pp.

– (2013). *Climate Change 2013: The Physical Science Basis. Contribution of Working Group I to the Fifth Assessment Report of the Intergovernmental Panel on Climate Change*. Tech. rep. Cambridge University Press, 27 pp.

Jimenez, J. L., Canagaratna, M. R., Donahue, N. M., Prevot, A. S. H., Zhang, Q., Kroll, J. H., DeCarlo, P. F., Allan, J. D. (2009). Evolution of organic aerosols in the atmosphere. *Science* **326**: 1525–1529.

Jonko, K. A., Hense, A., Feddema, J. J. (2009). Effects of land cover change on the tropical circulation in a GCM. *Clim. Dyn.* **35**: 635–649.

Keenlyside, N., Latif, M., Jungclaus, J., Kornblueh, L., Roeckner, E. (2008). Advancing decadal-scale climate prediction in the North Atlantic sector. *Nature* **453**: 84–88.

Keller, J. D. (2008). "Ensemble initialization using the breeding technique in a new ensemble forecasting system based on the numerical weather prediction model GME." PhD thesis. Meteorological Institut University of Bonn, 1–107.

Kerkweg, A., Buchholz, J., Ganzeveld, L., Pozzer, A., Tost, H., Jöckel, P. (2006). Technical Note: An implementation of the dry removal processes DRY DEPositionand SEDImentation in the Modular Earth Submodel System (MESSy). *Atmos. Chem. Phys.* **6**: 4617–4632.

Kiehl, J., Trenberth, K. E. (1997). Earth's annual global mean energy budget. *Bull. Am. Meteorol. Soc.* **78**: 197–208.

Kim, D., Ramanathan, V. (2008). Solar radiation budget and radiative forcing due to aerosols and clouds. *J. Geophys. Res.* **113**: 1–34.

Kim, K.-M., Lau, W. K.-M., Sud, Y. C., Walker, G. K. (2010). Influence of aerosol-radiative forcings on the diurnal and seasonal cycles of rainfall over West Africa and Eastern Atlantic Ocean using GCM simulations. *Clim. Dyn.* **35**: 115–126.

Kimoto, M., Yasutomi, N., Yokoyama, C., Emori, S. (2005). Projected changes in precipitation characteristics around Japan under the global warming. *SOLA* **1**: 85–88.

Kinne, S. a. S., Textor, C., Guilbert, S., Balkanski, Y., Baur, S. E., Berntsen, T. (2006). An AeroCom initial assessment - Optical properties in aerosol component modules of global models. *Atmos. Chem. Phys.* **6**: 1815–1834.

Klein, S. A., Hartmann, D. L. (1993). The seasonal cycle of low stratiform clouds. *J. Climate* **6**: 1587–1606.

Kloster, S., Feichter, J., Maier-Reimer, E., Six, K. D., Stier, P., Wetzel, P. (2006). DMS cycle in the marine ocean-atmosphere system - a global model study. *Biogeosciences* **3**: 29–51.

Koch, D., Surabi, M., Del-Genio, A., Reto, R. R., Alienov, I., Schmidt, G. A. (2009). Distinguishing aerosol Impacts on climate over the past century. *J. Climate* **22**: 2659–2677.

Koepke, P., Hess, M., Schult, I., Shettle, E. P. (1997). *Global aerosol data set*. Tech. rep. 243. 44 pp. Max-Planck Institute for Meteorology, Hamburg, Germany, 44.

Kulmala, M., Kerminen, V.-M., Anttila, T., Laaksonen, A., O'Dowd, C. D. (2004). Organic aerosol formation via sulphate cluster activation. *J. Geophys. Res. Atmos.* **109**: 1–7.

Lean, J. (2000). Evolution of the sun spectral irradiance since the maunder minimum. *Geophys. Res. Lett.* **27**: 2425–2428.

Leith, C. E. (1974). Theoretical skill of Monte Carlo forecasts. *Mon. Weather Rev.* **102**: 409–418.

Leutbecher, M., Palmer, T. (2008). Ensemble forecasting. *J. Comput. Phys.* **227**: 3515–3539.

Li, Z., Lee, K.-H., Wang, Y., Xin, J., Hao, W.-M. (2010). First observation-based estimates of cloud-free aerosol radiative forcing across China. *J. Geophys. Res. Atmos.* **115**: 1–9.

Li, Z., Moreau, L., Arking, A. (1997). On Solar Energy Disposition: A Perspective from Observation and Modeling. *Bull. Am. Meteorol. Soc.* **78**: 53–70.

Lin, S.-J., Rood, R. B. (1996). Multidimensional flux-form semi-Lagrangian transport schemes. *Mon. Weather Rev.* **124**: 2046–2068.

Loeb, N. G., Su, W. (2010). Direct aerosol radiative forcing uncertainty based on a radiative perturbation analysis. *J. Climate* **23**: 5288–5293.

Lohmann, U., Feichter, J. (2005). Global indirect aerosol effects: a review. *Atmos. Chem. Phys.* **5**: 715–737.

Lohmann, U., Feichter, J., Penner, J. E., Leaitch, W. R. (2000). Indirect effect of sulfate and carbonaceous aerosols: A mechanistic treatment. *J. Geophys. Res. Atmos.* **105**: 12, 193–12, 206.

Lorenz, E. N. (1963). A deterministic nonperiodic flow. *J. Atmos. Sci.* **20**: 130–141.

– (1982). Atmospheric predictability experiments with a large numerical model. *Tellus* **34**: 505–513.

Ma, X., vonSalzen, K., Li, J. (2008). Modelling sea salt aerosol and its direct and indirect effects on climate. *Atmos. Chem. Phys.* **8**: 1311–1327.

Machenhauer, B., Rasmussen, E. (1972). *On the integration of the spectral hydrodynamical equations by a transform method*. Tech. rep. 3. 44 pp. Kobenhavns Universitet, Institut for Teoretisk Meteorologi, Copenhagen,

Manzini, E., Giorgetta, M., Esch, M., Kornblueh, L., Roeckner, E. (2006). The influence of sea surface temperatures on the northern winter stratosphere: Ensemble simulations with the MAECHAM5 model. *J. Climate* **19**: 3863–3881.

Marcella, M. P., Eltahir, E. A. B. (2014). The role of mineral aerosols in shaping the regional climate of west Africa. *J. Geophys. Res. Atmos.* **119**: 5806–5822.

Mauritsen, T., Stevens, B., Roeckner, E., Crueger, T., Esch, M., Giorgetta, M., Haak, H., Jungclaus, J., Klocke, D., Matei, D., Mikolajewicz, U., Notz, D., Pincus, R., Schmidt, H., Tomassini, L. (2012). Tuning the climate of a global model. *J. Adv, Model Earth Sy.* **4**: 1–18.

McComiskey, A., Schwartz, S. E., Schmid, B., Guan, H., Lewis, E., Ricchiazzi, P., Ogren, J. A. (2008). Direct aerosol forcing: Calculation from observables and sensitivities to inputs. *J. Geophys. Res. Atmos.* **113**: 1–16.

McCormick, M. P., Thomason, L. W., Trepte, C. R. (1995). Atmospheric effects of the Mt Pinatubo eruption. *Nature* **373**: 399–404.

McFiggans, G., Artaxo, P., Baltensperger, U., Coe, H., Facchini, M. C., Feingold, G., Fuzzi, S., Gysel, M., Laaksonen, A., Lohmann, U., Mentel, T. F., Murphy, D. M., O'Dowd, C. D., Snider, J. R., Weingartner, E. (2006). The effect of physical and chemical aerosol properties on warm cloud droplet activation. *Atmos. Chem. Phys.* **6**: 2593–2649.

Meehl, G. A., Goddard, L., Murphy, J., Stouffer, R. J., Boer, G., Danabasoglu, G., Dixon, K., Giorgetta, M. A., Greene, A. M., Hawkins, E., Hegerl, G., Karoly, D., Keenlyside, N., Kimoto, M., Kirtman, B., Navarra, A., Pulwarty, R., Smith, D., Stammer, D., Stockdale, T. (2009). Decadal prediction: Can it be skillful? *Bull. Am. Meteorol. Soc.* 1467–1485.

MiKlip (2011). *A research Proposal on Decadal Climate Prediction*. Online report. URL: `http://www.fona-miklip.de/en/index.php`.

Miller, J., Haden, P. (2006). *Statistical Analysis with The General Linear Model*. 259 pp.

Moosmüller, H., Chakrabarty, R. K., Arnott, W. P. (2009). Aerosol light absorption and its measurement: A review. *J. Quant. Spectrosc. Radiat. Transfer.* **110**: 844–878.

Nordeng, T. E. (1994). *Extended versions of the convective parameterization scheme at ECMWF and their impact on the mean and transient activity of the model in the tropics*. 41 pp. ECMWF.

Oldenborgh, G. J.-v., Francisco, J., Reyes, D., Wouters, B., Hazeleger, W. (2012). Decadal prediction skill in a multi-model ensemble. *Clim. Dyn.* **38**: 1263–1280.

Orszag, S. A. (1970). Transform method for calculation of vector-coupled sums: Application to the Spectral Form of the Vorticity Equation. *J. Atmos. Sci.* **27**: 890–895.

Penner, J. E., Andreae, M., Annegarn, H., Barrie, L., Feichter, J., Hegg, D., Jayaraman, A., Leaitch, R., Murphy, D., Nganga, J., Pitari, G. (2001). Aerosols, their direct and Indirect effect, in: Climate Change 2001: The Scientific basis, Contribution of Working Group I to the third assesment report of the Intergovernmental Panel on Climate Change. *Cambridge University Press*, 298–348.

Petroff, A., Zhang, L. (2010). Development and validation of a size-resolved particle dry deposition scheme for application in aerosol transport models. *Geosci. Model Dev.* **3**: 753–769.

Pham, M., M/"uller, J.-F., C, G. P. B., Granier, Megie, G. (1995). A three-dimensional study of the tropospheric sulfur cycle. *J. Geophys. Res. Atmos.* **100**: 26, 061–26, 092.

Phillips, N. A. (1957). A coordinate system having some special advantages for numerical forecasting. *J. Meteor.* **14**: 184–185.

Pierrehumbert, R. T. (1995). Thermostats, radiator fins, and the local runaway greenhouse. *J. Atmos. Sci.* **52**: 1784–1806.

Pohlmann, H., Jungclaus, J. H., Kohl, A., Stammer, D., Marotzke, J. (2009). Initializing decadal climate predictions with the GECCO oceanic synthesis: effects on the north Atlantic. *J. Climate* **22**: 3926–3938.

Pongratz, J., Reick, C., Raddatz, T., Claussen, M. (2008). A reconstruction of global agricultural areas and land cover for the last millennium. *Global Biogeochem. Cycles* **22**: 1–16.

Qu, X., Hall, A. (2005). Surface contribution to planetary albedo variability in the cryosphere regions. *J. Climate* **18**: 5239–5252.

Raes, F., Dingenen, R. V., Vignati, E., Wilson, J., Putaud, J.-P., Seinfeld, J. H., Adams, P. (2000). Formation and cycling of aerosols in the global troposphere. *Atmos. Environ.* **34**: 4215–4240.

Ramanathan, V., Collins, W. (1991). Thermodynamic regulation of ocean warming by cirrus clouds deduced from observations of the 1987 El Niño. *Nature* **351**: 27–32.

Ramankutty, N., Foley, J. A. (1999). Estimating historical changes in global land cover: Croplands from 1700 to 1992. *Global Biogeochem. Cycles* **13**: 997–1027.

Reddy, M. S., Boucher, O., Balkanski, Y., Schulz, M. (2005). Aerosol optical depths and direct radiative perturbations by species and source type. *Geophys. Res. Lett.* **32**: 1–4.

Richardson, L. F. (1922). *Weather Prediction by Numerical Process*. 262 pp. Cambridge University Press.

Roeckner, E., Arpe, L., Bengtsson, M., Christoph, M., Claussen, L., D/"umenil, M., Esch, M., Giorgetta, U., Schlese, U. (1996). *The atmospheric general circulation model ECHAM-4: Model description and simulation of present-day climate.* Tech. rep. 218. 90 pp. Max-Planck Institute for Meteorology Hamburg Germany.

Rossow, W. B., Zhang, Y. (1995). Calculation of Surface and top of Atmosphere radiative fluxes from physical quantities based on ISCCP data sets 2. Validation and first Results. *J. Geophys. Res.* **100**: 1167–1197.

Sabin, T., Babu, C. A., Joseph, P. V. (2013). SST–convection relation over tropical oceans. *Int. J. Climatol.* **33**: 1424–1435.

Sarkar, S., Chokngamwong, R., Cervone, G., Singh, R., Kafatos, M. (2005). Variability of aerosol optical depth and aerosol forcing over India. *Adv. Space Res.* **37**: 2153–2159.

Schmidt, H., Rast, S., Bunzel, F., Esch, M., Giorgetta, M., Kinne, S., Krismer, T., Stenchikov, G., Timmreck, C., Tomassini, L., Walz, M. (2012). The response of the middle atmosphere to anthropogenic and natural forcing in the CMIP5 simulations with MPI-ESM. *J. Adv, Model Earth Sy.* **5**: 98–116.

Schulz, M., Textor, C., Kinne, S., Balkanski, Y., Bauer, S., Berntsen, T., Berglen, T., Boucher, O. (2006). Radiative forcing by aerosols as derived from the AeroCom present-day and pre-industrial simulations. *Atmos. Chem. Phys. Discuss.* **6**: 5095–5136.

Schwartz, S. E. (1996). The whitehouse effect - Shortwave radiative forcing of climate by anthropogenic aerosols: An overview. *J. Aerosol Sci.* **27**: 359–383.

Seager, R., Ting, M., Held, I., Kushnir, Y., Lu, J. (2007). Model projections of an imminent transition to a more arid climate in south-western North America. *Science* **316**: 1181–1184.

Sena, T. E., Artaxo, P., Correia, A. L. (2013). Spatial variability of the direct radiative forcing of biomass burning aerosols and the effects of land use change in Amazonia. *Atmos. Chem. Phys.* **13**: 1261–1275.

Shiklomanov, I. A. (1993). World fresh water resources. *Oxford University Press*, 13–24.

Simmons, A. J., Burridge, D. M. (1981). An energy and angular-momentum conserving vertical finite difference scheme and hybrid vertical coordinates. *Mon. Weather Rev.* **109**: 758–766.

Smith, D., Cusack, S., Colman, A., Folland, C., Harris, G., Murphy, J. (2007). Improved surface temperature prediction for the coming decade from a global circulation model. *Science* **317**: 796–799.

Solomon, S., Qin, D., Manning, M., Chen, Z., Marquis, M., Averyt, K., Tignor, M., Miller, H. (2007). *Contribution of Working Group I to the Fourth Assessment Report of the Intergovernmental Panel on Climate Change, 2007*. Tech. rep. 996 pp. Cambridge University Press.

Stenchikov, G. L., Kirchner, I., Robock, A., Graf, H.-F., Antuna, J. C., Grainger, R. G., Lambert, A., Thomason, L. (1998). Radiative forcing from the 1991 Mount Pinatubo volcanic eruption. *J. Geophys. Res.* **103**: 13, 837–13, 858.

Stephens, G. L., Li, J., Wild, M., Andrews, T. (2012). An update on Earth's energy balance in light of the latest global observations. *Nature Geosci.* **5**: 691–696.

Stevens, B., Giorgetta, M., Esch, M., Mauritsen, T., Crueger, T., Rast, S., Salzmann, M., Schmidt, H., Bader, J., Block, K., Brokopf, R., Fast, I., Kinne, S., Kornblueh, L., Lohmann, U., Pincus, R., Reichler, T., Roeckner, E. (2013). Atmospheric component of the MPI-M Earth System Model: ECHAM6. *J. Adv. Model Earth Sy.* **5**: 1–27.

Stier, P. (2004). "Towards the assesment of the aerosol radiative effects, a global modelling approach." 111 pp. PhD thesis. Max-Planck Institute for Meteorology Hamburg Germany, 1–111.

Stone, R. S., Anderson, G. P., Shettle, E., Roman I., M. O. (2008). Radiative impact of boreal smoke in the Arctic: Observed and modeled. *J. Geophys. Res. Atmos.* **113**: 1–7.

Sugimoto, N., Matsui, I., Shimizu, A., Nishizawa, T. (2008). Lidar network for monitoring Asian dust and air pollution aerosols. *IEEE Geosci. Remote Sens. Symp.* 573–576.

Sundqvist, H., Berge, E., Kristjansson, J. E. (1989). Condensation and cloud parameterization studies with a mesoscale numerical weather prediction model. *Mon. Weather Rev.* **117**: 1641–1657.

Takemura, T., Nozawa, T., Emori, S., Nakajima, T. Y., Nakajima, T. (2005). Simulation of climate response to aerosol direct and indirect effects with aerosol transport-radiation model. *J. Geophys. Res. Atmos.* **110**: 1–16.

Tang, I. N., Tridico, A. C., Fung, K. H. (1997). Thermodynamic and optical properties of salt aerosols. *J. Geophys. Res.* **102**: 23, 269–23, 275.

Tanre, D., Geleyn, J. F., Slingo, J. (1984). First results of the introduction of an advanced aerosol-radiation interaction in the ECMWF low resolution global model. *A. Deepak*, 133–177.

Tegen, I., Harrison, S. P., Kohfeld, K., Prentice, I. C., Coe, M., Heimann, M. (2002). Impact of vegetation and preferential source areas on global dust aerosol: Results from a model study. *J. Geophys. Res. Atmos.* **107**: 4576–4597.

Textor, C., Schulz, M., Guibert, S., Kinne, S., Balkanski, Y., Bauer, S., Berntsen, T., Berglen, T., Boucher, O., Chin, M., Dentener, F., Diehl, T., Easter, R., Feichter, H., Fillmore, D., Ghan, S., Ginoux, P., Gong, S., Grini, A., Hendricks, J., Horowitz, L., Huang, P., Isaksen, I., Iversen, I., Kloster, S., Koch, D., Kirkevåg, A., Kristjansson, J. E., Krol, M., Lauer, A., Lamarque, J. F., Liu, X., Montanaro, V., Myhre, G., Penner, J., Pitari, G., Reddy, S., Seland, Stier, P., Takemura, T., Tie, X. (2006). Analysis and quantification of the diversities of aerosol life cycles within AeroCom. *Atmos. Chem. Phys.* **6**: 1777–1813.

Tiedtke, M. (1989). A comprehensive mass flux scheme for cumulus parameterization in large-scale models. *Mon. Weather Rev.* **117**: 1779–1800.

Trenberth, K. E., Smith, L., Qian, T., Dai, A., Fassulo, J. (2007a). Estimates of the Global Water Budget and Its Annual Cycle Using Observational and Model Data. *J. Hydrometeorol.* **8**: 758–769.

Trenberth, K. E., Fasullo, J. T., Kiehl, J. (2009). Eearths Global Energy Budget. *American Meteorological Society*, 311–324.

Twomey, S. (1977). The influence of pollution on the shortwave albedo of clouds. *J. Atmos. Sci.* **34**: 1149–1152.

Vehkamäki, H., Kulmala, M., Napari, I., Lehtinen, K. E. J., Timmreck, C., Noppel, M., Laaksonen, A. (2002). An improved parameterization for sulfuric acid water nucleation rates for tropospheric and stratospheric conditions. *J. Geophys. Res. Atmos.* **107**: 4622–4632.

Vignati, E., Wilson, J., Stier, P. (2004). M7: An efficient size-resolved aerosol microphysics module for large-scale aerosol transport models. *J. Geophys. Res.* **109**: 1–17.

Webster, P. J., Chou, L. C. (1980). Seasonal structure of simple monsoon system. *J. Atmos. Sci.* **37**: 354–367.

Welton, E. J., Campbell, J. R., Spinhirne, J. D., ScottIII, V. S. (2001). Global monitoring of clouds and aerosols using a network of micro pulse lidar systems. *Proc. SPIE* **4153**: 151–158.

Wendisch, M., Hellmuth, O., Ansmann, A., Heintzenberg, J., Engelmann, R., Althausen, D., Eichler, H., Mueller, D., Hu, M., Zhang, Y., Mao, J. (2008). Radiative and dynamic effects of absorbing aerosol particles over the Pearl River Delta, China. *Atmos. Environ.* **42**: 6405–6416.

Whitby, K. T. (1978). The physical characteristics of sulfur aerosols. *Atmos. Environ.* **12**: 135–159.

Wilber, A. C., Kratz, D. P., Gupta, S. K. (1999). Surface emissivity maps for use in satellite retrievals of Longwave Radiation. *Nasa Technical paper* **209362**: 1–35.

Wild, M., Doris, F., Christoph, S., Norman, L., D, E. G., Gert, K. L. (2013). The global energy balance from a surface perspective. *Clim. Dyn.* **40**: 3107–3134.

Wild, M., Roeckner, E. (2006). Radiative fluxes in the ECHAM5 General Circulation Model. *J. Climate* **19**: 3792–3809.

Williams, J. E., Scheele, M. P., Velthoven, P. F. J. v., Thouret, V., Saunois, M., Reeves, C. E., Cammas, J.-P. (2010). The influence of biomass burning and transport on tropospheric composition over the tropical Atlantic Ocean and Equatorial Africa during the West African monsoon in 2006. *Atmos. Chem. Phys.* **10**: 9797–9817.

WMO (1986). *Atmospheric Ozone 1985 Assessment of our Understanding of the Processes Controlling its Present Distribution and Change*. Tech. rep. 16. World Meteorological Organization, 821–893.

Yu, R., Zhang, M., Cess, R. D. (1999). Analysis of the atmospheric energy budet: A consistency study of available data sets. *J. Geophys. Res. Atmos.* **104**: 9655–9661.

Zarzycki, C. M., Bond, T. C. (2010). How much can the vertical distribution of black carbon affect its global direct radiative forcing. *Geophys. Res. Lett.* **37**: 1–6.

Zender, C., Miller, R. L., Tegen, I. (2004). Quantifying mineral dust mass budgets: terminology, constraints, and current estimates. *EOS* **85**: 509–512.

Zhang, K., O'Donnell, D., Kazil, J., Stier, P., Kinne, S., Lohmann, U., Ferrachat, S., Croft, B., Quaas, J., Wan, H., Rast, S., Feichter, J. (2012). The global aerosol-climate model ECHAM-HAM, version 2: Sensitivity to improvements in process representations. *Atmos. Chem. Phys.* **12**: 8911–8949.

Zhang, T., Stackhouse, P. W., Gupta, S. K., Cox, S. J., Colleen, M. J., Hinkelman, L. M. (2013). The validation of the GEWEX SRB surface shortwave flux data products using BSRN measurements: A systematic quality control, production and application approach. *J. Quant. Spectrosc. Radiat. Transfer.* **122**: 127–140.

Zhang, X. Y., Wang, Y. Q., Niu, T., Zhang, X. C., Gong, S. L., Zhang, Y. M., Sun, Y. J. (2012). Atmospheric aerosol compositions in China: Spatial/temporal variability, chemical signature, regional haze distribution and comparisons with global aerosols. *Atmos. Chem. Phys.* **12**: 779–799.

Zhang, Y., Rossow, W. B., Lacis, A. A., Oinas, V., Mishchenko, M. I. (2004). Calculation of radiative fluxes from the surface to top of atmosphere based on ISCCP and other global data sets: Refinements of the radiative transfer model and the input data. *J. Geophys. Res. Atmos.* **109**: 1–27.

Zhao, C., Liu, X., Leung, L. R., Hagos, S. (2011). Radiative impact of mineral dust on monsoon precipitation variability over West Africa. *Atmos. Chem. Phys.* **11**: 1879–1893.

BONNER METEOROLOGISCHE ABHANDLUNGEN

Herausgegeben vom Meteorologischen Institut der Universität Bonn durch Prof. Dr. H. FLOHN (Hefte 1-25), Prof. Dr. M. HANTEL (Hefte 26-35), Prof. Dr. H.-D. SCHILLING (Hefte 36-39), Prof. Dr. H. KRAUS (Hefte 40-49), ab Heft 50 durch Prof. Dr. A. HENSE.

Heft 1-49:	siehe `http://www.meteo.uni-bonn.de/bibliothek/bma`	
Heft 50:	***Petra Friederichs***: Interannuelle und dekadische Variabilität der atmosphärischen Zirkulation in gekoppelten und SST-getriebenen GCM-Experimenten. 2000, 133 S. + VIII.	€ 25
Heft 51:	***Heiko Paeth***: Anthropogene Klimaänderungen auf der Nordhemisphäre und die Rolle der Nordatlantik-Oszillation. 2000, 168 S.+ XVIII.	€ 28
Heft 52:	***Hildegard Steinhorst***: Statistisch-dynamische Verbundsanalyse von zeitlich und räumlich hoch aufgelösten Niederschlagsmustern: eine Untersuchung am Beispiel der Gebiete von Köln und Bonn. 2000, 146 S. + XIV.	€ 25
Heft 53:	***Thomas Klein***: Katabatic winds over Greenland and Antartica and their interaction with mesoscale and synoptic-scale weather systems: three-dimensional numerical models. 2000, 146 S. + XIV.	€ 25
Heft 54:	***Clemens Drüe***: Experimentelle Untersuchung arktischer Grenzschichtfronten an der Meereisgrenze in der Davis-Straße. 2001, 165 S. + VIII.	€ 28
Heft 55:	***Gisela Seuffert***: Two approaches to improve the simulation of near surface processes in numerical weather prediction models. 2001, 128 S. + VI.	€ 25
Heft 56:	***Jochen Stuck***: Die simulierte axiale atmosphärische Drehimpulsbilanz des ECHAM3-T21 GCM. 2002, 202 S. + VII.	€ 30
Heft 57:	***Günther Haase***: A physical initialization algorithm for non-hydrostatic weather prediction models using radar derived rain rates. 2002, 106S. + IV.	€ 25
Heft 58:	***Judith Berner***: Detection and Stochastic Modeling of Nonlinear Signatures in the Geopotential Height Field of an Atmospheric General Circulation Model. 2003, 157 S. + VIII.	€ 28
Heft 59:	***Bernd Maurer***: Messungen in der atmosphärischen Grenzschicht und Validation eines mesoskaligen Atmosphärenmodells über heterogenen Landoberflächen. 2003, 182 S. + IX.	€ 30
Heft 60:	***Christoph Gebhardt***: Variational reconstruction of Quaternary temperature fields using mixture models as botanical – climatological transfer functions. 2003, 204 S. + VIII.	€ 30
Heft 61:	***Heiko Paeth***: The climate of tropical and northern Africa – A statistical-dynamical analysis of the key factors in climate variability and the role of human activity in future climate change. 2005, 316 S. + XVI.	€ 15
Heft 62:	***Christian Schölzel***: Palaeoenvironmental transfer functions in a Bayesian framework with application to Holocene climate variability in the Near East. 2006, 104 S. + VI.	€ 15
Heft 63:	***Susanne Bachner***: Daily precipitation characteristics simulated by a regional climate model, including their sensitivity to model physics, 2008, 161 S.	€ 15

Heft 64: ***Michael Weniger***: Stochastic parameterization: a rigorous approach to stochastic three-dimensional primitive equations, 2014, 148 S. + XV. open access[1]

Heft 65: ***Andreas Röpnack***: Bayesian model verification: predictability of convective conditions based on EPS forecasts and observations, 2014, 152 S. + VI. open access[1]

Heft 66: ***Thorsten Simon***: Statistical and Dynamical Downscaling of Numerical Climate Simulations: Enhancement and Evaluation for East Asia, 2014, 48 S. + VII. + Anhänge open access[1]

Heft 67: ***Elham Rahmani***: The Effect of Climate Change on Wheat in Iran, 2014, [erschienen] 2015, 96 S. + XIII. open access[1]

Heft 68: ***Pablo A. Saavedra Garfias***: Retrieval of Cloud and Rainwater from Ground-Based Passive Microwave Observations with the Multi-frequency Dual-polarized Radiometer ADMIRARI, 2014, [erschienen] 2015, 168 S. + XIII. open access[1]

Heft 69: ***Christoph Bollmeyer***: A high-resolution regional reanalysis for Europe and Germany - Creation and Verification with a special focus on the moisture budget, 2015, 103 S. + IX. open access[1]

Heft 70: ***A S M Mostaquimur Rahman***: Influence of subsurface hydrodynamics on the lower atmosphere at the catchment scale, 2015, 98 S. + XVI. open access[1]

Heft 71: ***Sabrina Wahl***: Uncertainty in mesoscale numerical weather prediction: probabilistic forecasting of precipitation, 2015, 108 S. open access[1]

Heft 72: ***Markus Übel***: Simulation of mesoscale patterns and diurnal variations of atmospheric CO_2 mixing ratios with the model system TerrSysMP-CO_2, 2015, [erschienen] 2016, II, 158 S. open access[1]

Heft 73: ***Christian Bernardus Maria Weijenborg***: Characteristics of Potential Vorticity anomalies associated with mesoscale extremes in the extratropical troposphere, 2015, [erschienen] 2016, XI, 151 S. open access[1]

Heft 74: ***Kaleem Muhammad***: A sensitivity study of decadal climate prediction to aerosol variability using ECHAM6-HAM (GCM), 2016, [erschienen] 2016, XIII, 98 S. open access[1]

---

[1] Available at `http://hss.ulb.uni-bonn.de/fakultaet/math-nat/`

METEOROLOGISCHES INSTITUT
MATHEMATISCH NATURWISSENSCHAFTLICHE FAKULTÄT
UNIVERSITÄT BONN